

**Acoustic Emission Analysis of the Effect of a 2D
Wedge Shaped Blade on the Compact
Bone Cutting Process**

A thesis submitted for the degree of
Master of Engineering

By

Ashkan Safari

B.Sc.

Department of Mechanical and Electronic Engineering
School of Engineering
Institute of Technology Sligo

September 2006

Supervisors

Mr. Ger Reilly

Dr. Brendan McCormack

This thesis is dedicated to my family, Mohammad, Monir, Fara and Elham.

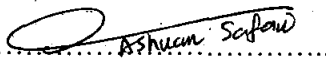
A special mention to Mehdi (R.I.P).

You have not been forgotten.

Declaration

This thesis describes original work which has not been submitted for a degree at any other university or college.

The investigations were carried out in the Department of Mechanical and Electrical Engineering, Institute of Technology Sligo, under the supervision of Mr. Ger Reilly.



Ashkan Safari

Ashkan Safari

September 2006

Acknowledgments

This research would not have been completed without the guidance of my supervisors, Mr. Ger Reilly and Dr. Brendan McCormack.

I would also like to acknowledge the support of the technical team, Mr. Gordan Muir and Mr. Ray Tobin. Special thanks to Mr. Timothy Bradshaw (Physical Acoustic) for his technical assistance with acoustic emission testing.

To all my colleagues in the office Anthony, Chan, Cormack, Eamonn, John and Shane, thank you for your help. Particular thanks to Bahman, Hamid, Joanna and Mehdi for your support.

Recent Publications

1. Indentation fracture of bovine cortical bone: acoustic emission technique, Safari. A., Reilly, G.A., McCormack, B.A.O., the 12th Annual Conference of the Section of Bioengineering of the Royal Academy of Medicine in Ireland, Galway, Ireland, January 2006.
2. Analysis of indentation loading of cortical bone using acoustic emission technique, Safari. A., Reilly, G.A., McCormack, B.A.O., the 1st International Conference on Mechanics of Biomaterials & Tissues, Hawai'i, USA, December 2005.
3. Detection of microcracks during bone cutting using acoustic emission technique, Safari. A., Reilly, G.A., McCormack, B.A.O., Proceeding of the 19th Conference of European Society for Biomaterials combined with European Society of Biomechanics, page 214, Sorrento, Naples, Italy, September 2005.
4. Sequential labelling and AE analysis of damage in cortical bone during indentation cutting, Reilly, G.A., Safari. A., Taylor. D, McCormack, B.A.O. Proceeding of the 29th ASB Annual Meeting, page 565, Cleveland, Ohio, USA, August 2005.
5. Acoustic Emission during indentation loading of bone. Safari. A., Reilly, G.A., McCormack, B.A.O., Proceeding of the 11th Annual Conference of the Section of Bioengineering of the Royal Academy of Medicine in Ireland, page 58, Dublin, Ireland, January 2005.
6. An investigation of acoustic emission technique for cortical bone cracking. Safari. A., Reilly, G.A., McCormack, B.A.O., Macey, A, Proceeding of the 5th Annual Multidisciplinary Research Conference at Sligo General Hospital, Page 17, Sligo, Ireland, November 2004.

Contents

Declaration	I
Acknowledgments	II
Recent Publications	III
Contents	IV
Table of Figures	VII
List of Tables	X
Abstract	XI
List of Abbreviations and Glossary	XII
Chapter 1: Introduction	1
1.1 Background of the research	1
1.2 Bone surgery	1
1.3 Surgical cutting instruments	2
1.3.1 Power cutting tools	2
1.3.2 Manual cutting tools	2
1.4 Indentation fracture in cortical bone	4
1.5 Acoustic emission monitoring of bone damage	5
1.6 Objective of the research	6
Chapter 2: Literature Review	7
2.1 Overview.....	7
2.2 The cutting process in materials.....	7
2.2.1 Models of fracture during the cutting process.....	8
2.3 Structure of bone	9
2.3.1 Macroscopic structure of bone	10
2.3.2 Cortical and cancellous bone	11
2.3.3 Woven and lamellar bone	12
2.3.4 Primary and secondary bone	13
2.3.5 Molecular level of bone	14
2.3.6 Bone cells.....	15
2.4 Mechanical properties of bone.....	16
2.4.1 Stress and strain.....	16
2.4.2 Stiffness and strength.....	17
2.4.3 Fracture toughness.....	19

2.5	Damage in cortical bone	22
2.5.1	Nature of microdamage	23
2.5.2	Effect of microcracking on mechanical properties.....	24
2.5.3	Development of microcracks	25
2.5.4	Effect of cortical bone structure on microcrack development	26
2.5.5	Toughening mechanisms in cortical bone.....	27
2.5.6	Damage process in cortical bone during the cutting process.....	28
2.6	Bone damage observation techniques	29
2.7	Acoustic emission technique.....	32
2.8	Acoustic emission studies on cortical bone	34
2.8.1	AE during fracture processes in cortical bone	35
2.8.2	Parameters that affect AE response in bone.....	36
2.9	Acoustic emission studies on other materials	37
2.9.1	AE studies on titanium alloy and steel materials	37
2.9.2	AE studies on bone cements	38
2.9.3	AE and failure mode detection in composite materials	39
2.9.4	AE activity in materials during the indentation loading	39
2.9.5	AE activity and fracture energy.....	40
2.10	Summary.....	40
Chapter 3: Materials and Methods		41
3.1	Scope of the experimental work.....	41
3.2	Overview of the experimental set up.....	41
3.3	Specimen preparation.....	42
3.4	Materials used in this work.....	44
3.4.1	Wedge type blade	44
3.4.2	Mechanical testing machine.....	45
3.4.3	Bone specimen holding fixture	47
3.4.4	Acoustic emission measurement instruments	47
3.4.4.1	AE sensor	48
3.4.4.2	Preamplifier.....	49
3.4.4.3	AE data acquisition card	50
3.4.5	AEwin analysis software.....	52
3.4.6	Dynamometer.....	53
3.5	Experiment model	54

3.5.1	Experiment 1 set up	55
3.5.2	Experiment 2 set up	58
3.5.3	AE acquisition set up	59
3.6	SEM imaging	60
Chapter 4: Results		62
4.1	Threshold set up for AE testing	62
4.2	Results of experiment 1	62
4.2.1	Indentation fracture load	63
4.2.2	AE hit accumulation during the fracture process	64
4.2.3	Analysis of AE hit amplitudes	68
4.2.4	Analysis of AE hit durations	70
4.2.5	Abs-energy as measure of fracture characterisation	73
4.2.6	Abs-energy from low and high amplitude hits	75
4.2.7	Analysis of abs-energy during the fracture process	76
4.3	Results of experiment 2	79
4.3.1	Indentation fracture load	80
4.3.2	Number of AE hits at 50/90/100% of fracture load	80
4.3.3	Quality of AE hits at 50/90/100% of fracture load	81
4.3.4	SEM images analysis	83
Chapter 5: Discussion		87
5.1	Overview	87
5.2	Discussion of results in experiment 1	88
5.2.1	Fracture process monitoring based on AE hit accumulation	88
5.2.2	Failure modes detection based on amplitude and duration	90
5.2.3	Fracture process monitoring based on abs-energy	92
5.2.4	Crack initiation and propagation during indentation process	96
5.3	Discussion of results in experiment 2	97
Chapter 6: Conclusions and Future Work		99
6.1	Conclusions	99
6.2	Recommendations for future work	100
References		102
Appendix A - Results of experiment 1		
Appendix B - Results of experiment 2		
Appendix C - Technical sheet		

Table of Figures

Figure 1.1: An amputation saw which is used to cut a long bone	2
Figure 1.2: Tip details of osteotome, scalpel and gouge	3
Figure 1.3: Tip geometry of wedge angle type blade	3
Figure 1.4: Osteotome in use, impact with a mallet	4
Figure 1.5: Indentation fracture processes in materials	4
Figure 1.6: Labelled crack process during the cutting of cortical bone.....	5
Figure 1.7: Acoustic emission generation process	5
Figure 2.1: Orthogonal cutting process	7
Figure 2.2: Indentation cutting process	8
Figure 2.3: Lawn model of crack formation under indentation process in a brittle material	9
Figure 2.4: Hierarchical structure of bone.....	9
Figure 2.5: Schematic diagram of a long bone.....	10
Figure 2.6: Diagram of a portion of a long bone shaft showing details of cortical and cancellous bones.....	11
Figure 2.7: Fibre arrangements in lamellar bone.....	12
Figure 2.8: Diagram of fibrolamellar bone formation process	13
Figure 2.9: Diagram of osteonal bone formation as a result of remodelling process.....	14
Figure 2.10: Schematic diagram of collagen molecules-mineral crystals interactions	15
Figure 2.11: Compressive (a), tensile (b), and shear (c) stresses applied to an object	16
Figure 2.12: A typical stress-strain curve in a tensile test.....	18
Figure 2.13: Modes of fracture in materials: (I) opening, (II) sliding & (III) tearing	20
Figure 2.14: Segregation of stress-strain curve into elastic, damaging and fracture regions for cortical bone loaded in tensile mode	22
Figure 2.15: Sites of microcrack formation in osteonal bone.....	23
Figure 2.16: Model of crack growth processes in cortical bone.....	25
Figure 2.17: Macrocrack growth subjected to various modes of load.....	26
Figure 2.18: Crack deflection at the secondary osteon boundary in cortical bone.....	27
Figure 2.19: Microcracking toughening mechanisms during crack growth in cortical bone	27
Figure 2.20: Bridging effect as a toughening mechanism in cortical bone: (a) crack bridging and (b) uncracked ligament bridging.....	28
Figure 2.21: Indentation crack growth processes in bovine cortical bone: (a) transverse crack growth and (b) longitudinal crack growth.....	29
Figure 2.22: Fuchsin-stained microcrack	30
Figure 2.23: Stained developing microcrack using fluorescent sequential labelling method	31

Figure 2.24: Process of generation of acoustic emission signal, detected by a typical AE system setup	32
Figure 2.25: AE hit feature extraction diagram	33
Figure 3.1: Schematic of the experimental arrangement	42
Figure 3.2: Longitudinal sectioning of bone pieces into 8mm cubic specimens using low-speed saw	43
Figure 3.3: Preparation procedure for 8mm cubic specimens	44
Figure 3.4: A typical wedge type blade	45
Figure 3.5: Application of indentation cutting load using MTS machine	46
Figure 3.6: Bone specimen holding fixture	47
Figure 3.7: A typical AE sensor	48
Figure 3.8: AE sensor placed on the bone specimen	48
Figure 3.9: The 2/4/6.type amplifier	49
Figure 3.10: PCI-2 system connection block diagram	50
Figure 3.11: PCI-2 board layout showing key AE channels and parametric connectors	51
Figure 3.12: 2D line (a) and point (b) plots in AEwin	52
Figure 3.13: A Kistler dynamometer (Type 9257BA)	53
Figure 3.14: Dynamometer cutting force measuring system	53
Figure 3.15: Experiment progression for experiments 1 & 2	54
Figure 3.16: Experimental setup for monotonic indentation cutting load	55
Figure 3.17: Bone holding fixture mounted on Kistler dynamometer	56
Figure 3.18: Close-up of the sensor attachment to the bone specimen	56
Figure 3.19: Alignment of the blade to bone specimen	57
Figure 3.20: Kistler dynamometer connection to PCI-2 card	57
Figure 3.21: Gold coated bone specimen placed in the fixture for SEM imaging	61
Figure 4.1: A typical graph of load versus time during longitudinal indentation cutting process	63
Figure 4.2: Typical plots of load & cumulative number of AE hits versus time for specimens taken from different sources	66
Figure 4.3: Plot of cumulative number of AE hits versus load intervals based on maximum fracture load	66
Figure 4.4: Stages of change in AE hit accumulation during the indentation cutting load	67
Figure 4.5: Amplitude distribution graph of AE hits recorded in all experiments	68
Figure 4.6: Plot of AE hit frequencies as a function of amplitude range in all experiments	70
Figure 4.7: Correlation plot of amplitude versus duration for a typical test	71
Figure 4.8: Correlation plot of amplitude versus duration for all tests	71
Figure 4.9: A typical graph of load & duration versus time	72

Figure 4.10: Correlation plot of abs-energy versus amplitude for AE hits in all experiments	74
Figure 4.11: Correlation plot of abs-energy versus duration for AE hits in all experiments	74
Figure 4.12: Plot of mean values of abs-energy as a function of load intervals based on maximum fracture load	76
Figure 4.13: A typical graph of load & abs-energy versus time	77
Figure 4.14: Abs-energy produced by AE hits prior to and at final maximum load	77
Figure 4.15: Typical graphs of abs-energy versus load intervals showing the first high amplitude AE hit	78
Figure 4.16: Exponential increase in the number of AE hits at chosen load intervals prior to and at final maximum load	80
Figure 4.17: Abs-energy produced at 3 chosen load intervals prior to and at final maximum load	82
Figure 4.18: SEM image of bone specimen cut up to 50% of maximum load	84
Figure 4.19: Cumulative number of AE hits of bone specimen cut up to 50% of maximum load	84
Figure 4.20: SEM image of bone specimen cut up to 90% of maximum load	85
Figure 4.21: Cumulative number of AE hits for bone specimen cut up to 90% of maximum load	85
Figure 4.22: SEM image of bone specimen cut up to maximum fracture load	86
Figure 4.23: Cumulative number of AE hits for bone specimen cut up to maximum fracture load	86
Figure 5.1: Stages of crack growth up to final fracture during fatigue tensile loading of titanium alloy	89
Figure 5.2: Stages of crack growth up to final fracture based on change in AE hit accumulation during indentation loading	89
Figure 5.3: Observation of the signal with the highest duration value at final failure for bone cement specimen under fatigue loading	92
Figure 5.4: Crack growth process based on change in AE hit abs-energy during indentation cutting	94
Figure 5.5: Fatigue crack growth processes	94
Figure 5.6: Stop/start crack growth process occurring in some specimens	95
Figure 5.7: Crack initiation and propagation phases during indentation cutting based on the change in AE hit accumulation and abs-energy content	96

List of Tables

Table 2.1: Elastic Moduli of cortical bone	18
Table 2.2: Strength properties of cortical bone	19
Table 2.3: Fracture toughness properties of cortical bone.....	21
Table 3.1: Frequency bandwidth for gains supplied in 2/4/6 amplifier.....	49
Table 3.2: Specimen groups in experiment 1	58
Table 3.3: Specimen groups in experiment 2	59
Table 3.4: The range of AE signal voltage amplitudes for a 40dB gain	60
Table 4.1: Load levels at onset of AE activity & significant change in AE hit rate during indentation cutting loading	68
Table 4.2: AE hits clustered into two groups based on amplitude values using K-mean clustering method	69
Table 4.3: Durations of high amplitude AE hits prior to and at maximum fracture load.....	73
Table 4.4: High amplitude AE hits classified into two groups based on duration values	73
Table 4.5: Abs-energy produced by low and high amplitude AE hits	75
Table 4.6: Load levels associated with the first high energy signal	79
Table 4.7: Number of AE hits at 3 load intervals of 50%, 90% & 100% of maximum load ...	81
Table 4.8: Mean values of AE hit features at 3 load intervals of 50%, 90% & 100% of maximum load.....	82
Table 4.9: AE hit features at maximum fracture load	83

Abstract

Surgeons may use a number of cutting instruments such as osteotomes and chisels to cut bone during an operative procedure. The initial loading of cortical bone during the cutting process results in the formation of microcracks in the vicinity of the cutting zone with main crack propagation to failure occurring with continued loading. When a material cracks, energy is emitted in the form of Acoustic Emission (AE) signals that spread in all directions, therefore, AE transducers can be used to monitor the occurrence and development of microcracking and crack propagation in cortical bone. In this research, number of AE signals (hits) and related parameters including amplitude, duration and absolute energy (abs-energy) were recorded during the indentation cutting process by a wedge blade on cortical bone specimens. The cutting force was also measured to correlate between load-displacement curves and the output from the AE sensor.

The results from experiments show AE signals increase substantially during the loading just prior to fracture between 90% and 100% of maximum fracture load. Furthermore, an amplitude threshold value of 64dB (with approximate abs-energy of 1500aJ) was established to separate AE signals associated with microcracking (41-64dB) from fracture related signals (65-98dB). The results also demonstrated that the complete fracture event which had the highest duration value can be distinguished from other growing macrocracks which did not lead to catastrophic fracture. It was observed that the main crack initiation may be detected by capturing a high amplitude signal at a mean load value of 87% of maximum load and unsteady crack propagation may occur just prior to final fracture event at a mean load value of 96% of maximum load. The author concludes that the AE method is useful in understanding the crack initiation and fracture during the indentation cutting process.

List of Abbreviations and Glossary

Abbreviations

AE	Acoustic Emission
LSCM	Laser Scanning Confocal Microscopy
MARSE	Measured Area under the Rectified Signal Envelope
NDT	Non Destructive Testing
PCI	Peripheral Component Interconnect
SEM	Scanning Electron Microscopy

Glossary

Absolute energy	A true energy measure of the AE hit
Acoustic emission	Elastic waves generated by the rapid release of energy from sources within a material
Amplitude	The largest Voltage peak in the AE signal waveform
Counts	The AE signal excursions over the AE threshold
dBae	A unit of measurement of AE signal amplitude
Event	A local material change giving rise to acoustic emission
Frequency	For an oscillating signal or process, the number of cycles occurring in unit time.
Hit (AE)	The process of detecting and measuring an AE signal on a channel.
Lamellae	Fine sheets made up of planar arrangement of collagen fibres which are held near one another
MARSE energy	A gain dependant energy measure of the AE hit

Osteon	The tightly packed concentric rings of bone tissue with a blood vessel running through the central canal
Osteotome	Surgical cutting instrument used for the cutting of bone
Risetime	The time from an AE signal's first threshold crossing count to its peak
Slip planes	Closely spaced surfaces along which differential movement takes place in a material.

Chapter 1: Introduction

1.1 Background of the research

Surgical procedures involving cutting of bone are complex processes. A number of cutting instruments such as osteotomes may be used by surgeons to complete the operative procedure. Application of a surgical cutting tool to cut bone may result in microstructural damage such as microcracking and cracking. It has been observed by other researchers that microcracking processes occur as part of a larger crack creation process (Vashishth et al., 1997).

Little literature exists regarding development of microcracks and crack growth during the cutting process. During the indentation loading of a bone specimen using a wedge blade, it was difficult to distinguish clearly between stages of crack growth by use of histological techniques (Reilly and Taylor, 2005a). Therefore, it is worth developing a non-destructive method such as acoustic emission technique for real-time monitoring of crack growth during the cutting process.

1.2 Bone surgery

Osteotomy is a surgical procedure which involves the process of bone cutting and can be classified into three types corresponding to specific tasks (Giraud et al., 1991):

- Excision osteotomy: To remove a pathological portion of bone;
- Reparative osteotomy: To change the size or alignment of a part of the bone;
- Osteotomy for purpose of approach: To cut the bone to access the operation site and returning the bone to original position.

Amputation is another type of bone surgery which involves the removal of an affected limb to control pain or a disease process.

1.3 Surgical cutting instruments

During bone surgery, a number of surgical cutting tools may be used depending on the shape of the cut. These cutting tools are classified corresponding to the driving force into two groups of power and manual cutting instruments.

1.3.1 Power cutting tools

In surgical power cutting, drills and various types of saws such as oscillating, reciprocating and circular saws are driven by a motor to cut the bone in different shapes. The main advantage of the power cutting process is minimising the cutting time. A number of key issues are concerned with the power cutting process including initial deformation of bone, bone plasticity, chip formation, heat generation and cutting force measurement (Giraud et al., 1991). This study is not concerned with these aspects of power cutting.

1.3.2 Manual cutting tools

Surgical manual cutting involves the use of surgical handsaws, chisels, osteotomes, gouges, and etc. Different types of handsaws with specific blades may be used for bone cutting during amputation surgery such as Satterlee saws (Figure 1.1).

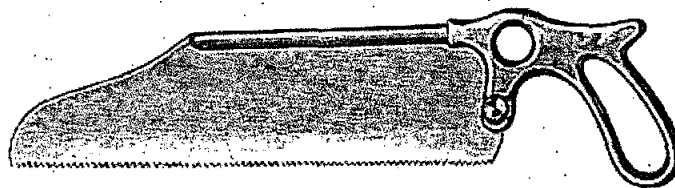


Figure 1.1: An amputation saw which is used to cut a long bone
(www.icrc.org/emergency-items/Volume2)

Chisels are cutting instruments which are used to cut, scrape and sculpt bone. The sculpting chisels are called osteotomes. The osteotomes may be used during a surgical

procedure such as removal of bony protrusions, bunions and shaping of the bone such as occurs in maxillofacial surgery. Figure 1.2 shows the varied tip geometries of osteotome, chisel and gouge.

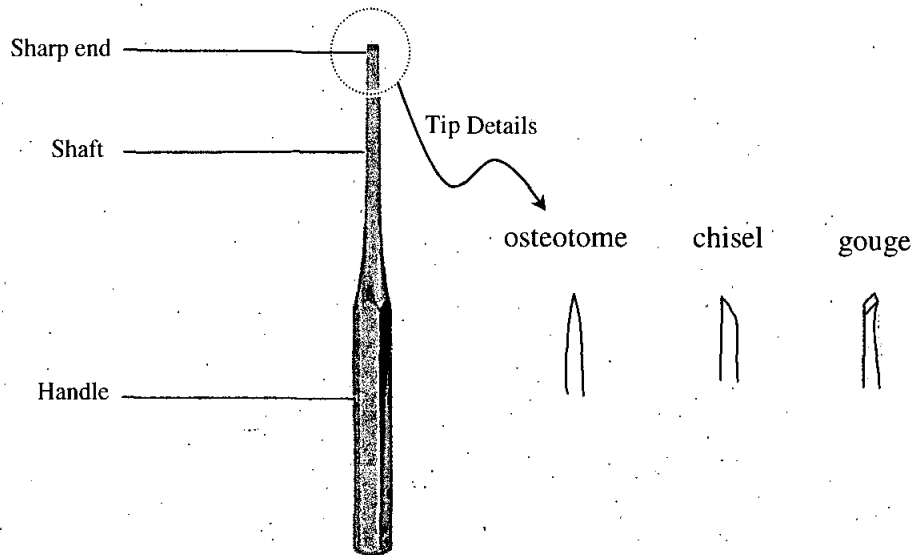


Figure 1.2: Tip details of osteotome, scalpel and gouge (www.kmedicoem.com/pdf/surgical.pdf)

The cutting edge of an osteotome is a 2D wedge. The included angle of this wedge may vary from manufacturer but it is normally in the range of 20° to 50° as shown in Figure 1.3. The tip of the cutting edge may also have a cutting edge radius, especially if the blade becomes blunted.

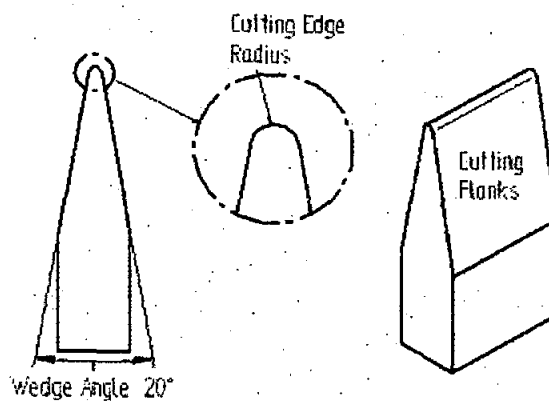


Figure 1.3: Tip geometry of wedge angle type blade (Reilly et al., 2004)

As shown in Figure 1.4, a surgical mallet is used to force the osteotome into the bone. Damage processes during bone removal is the main issue with manual cutting which is the focus of this research.



Figure 1.4: Osteotome in use, impact with a mallet

1.4 Indentation fracture in cortical bone

As shown in Figure 1.5, when a cutting tool is applied to a material, a compacted zone initially forms around the indenter tip that will create a main crack. Further loading results in the advance of the main crack to the complete fracture (Lawn, 1975). Within the compacted zone, the material is likely to be damaged in the form of microcracks and fractures on slip planes as will be discussed in the following chapter.

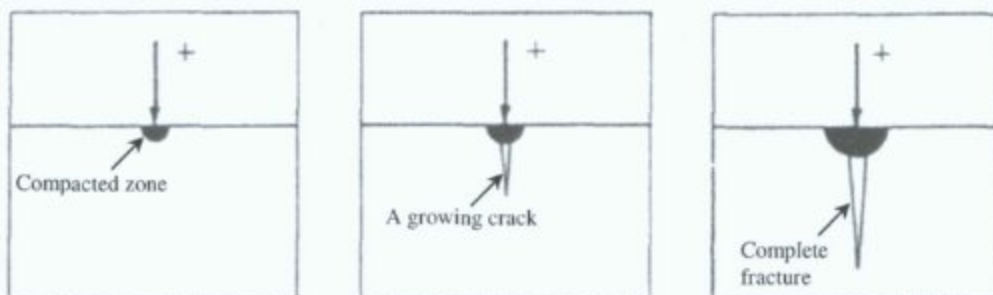


Figure 1.5: Indentation fracture processes in materials (Lawn, 1975)

During the indentation cutting process on cortical bone specimens, a damage zone with microcrack was observed around the main crack tip using a sequential

fluorescent labelling technique (Figure 1.6) however it was not possible to clearly monitor the stages in the main crack growth (Reilly and Taylor, 2005a).

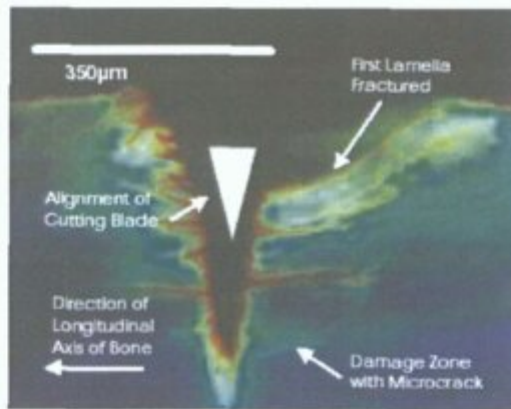


Figure 1.6: Labelled crack process during the cutting of cortical bone (Reilly and Taylor, 2005a)

1.5 Acoustic emission monitoring of bone damage

The Acoustic Emission (AE) technique is a dynamic test method providing a response to ongoing change in a material during application of an external load. As shown in Figure 1.7, the damage-related AE signals (hits) can be detected by AE sensors and processed in a main AE instrument to extract AE features such as amplitude, duration and energy of the AE signals.

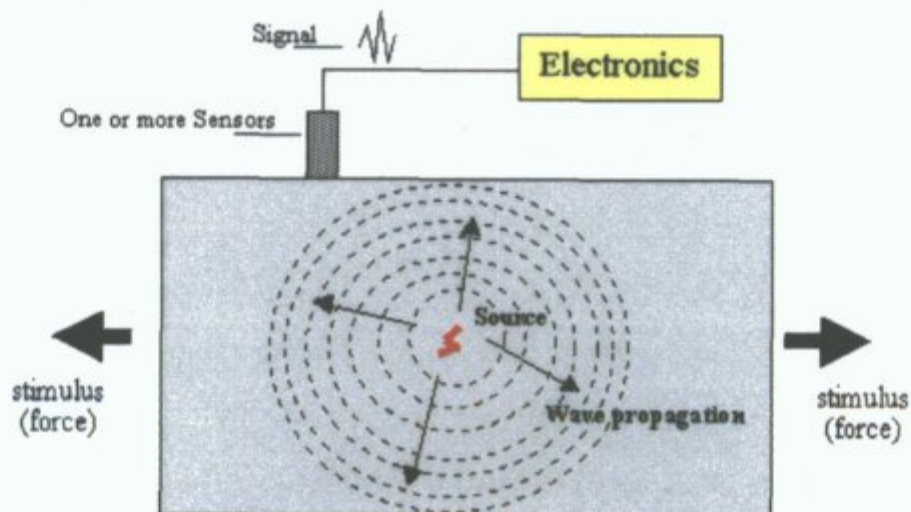


Figure 1.7: Acoustic emission generation process (www.ndt.net/article/az/ae_idx.htm)

The AE technique was successfully used to detect damage-related AE signals at early stage of fracture process in bone specimens subjected to a mechanical load (Hanagud et al., 1973). These early AE signals during yield phase were found to be associated with initial microcracking (Zioupos et al., 1994). It was reported by researchers that during fracture processes, microcracking produces lower energy AE hits, whereas crack growth events generate higher energy signals (Akkus et al., 2000).

1.6 Objective of the research

In this study, AE signals were recorded during the indentation fracture processes in bovine cortical bone specimens and cutting forces were also measured simultaneously using a dynamometer. The main aims of this research were to detect crack initiation and propagation phases based on AE signals parameters such as amplitude, duration and absolute energy as well as associating the different stages of crack growth to load-deformation curves.

Chapter 2: Literature Review

2.1 Overview

This literature review focuses on key elements of research relevant to the main objectives of this research work. In this regard, the review focuses on:

1. The cutting process
2. The structure of bone
3. Fracture and damage in bone
4. Damage detection techniques in bone
5. Acoustic emission damage monitoring technique.

2.2 The cutting process in materials

The cutting process is classified into two models of orthogonal and indentation cutting. These two types of cutting process may be applied to the bone during surgical procedures using osteotomes. As shown in Figure 2.1, in the orthogonal cutting model, the cutting edge of the blade is aligned at a right angle to the line of cutting action (Merchant, 1944).

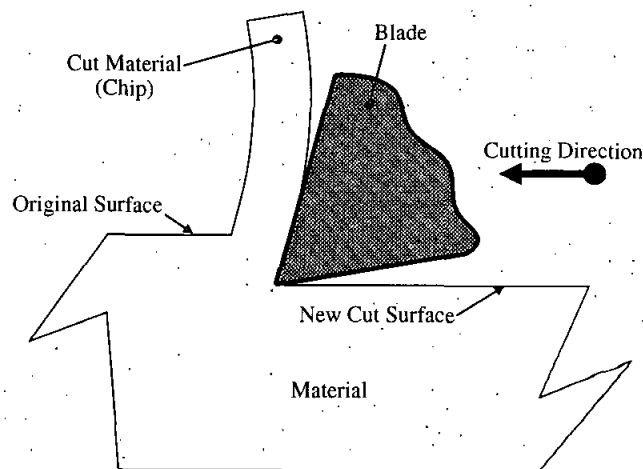


Figure 2.1: Orthogonal cutting process (Merchant, 1944)

During the indentation cutting process, the tip of the blade is perpendicularly penetrated into the material and orientation of the wedge is symmetrical to the line of cutting action (Figure 2.2).

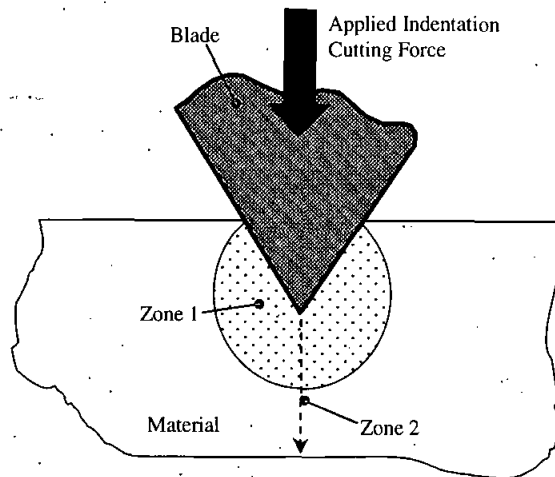


Figure 2.2: Indentation cutting process (Hill, 1953)

2.2.1 Models of fracture during the cutting process

It has been described that during the indentation cutting process in a ductile material as shown in Figure 2.2, a small plastic area forms at the sides of the tip of the blade (zone 1). Further loading of the material results in a gradual spread of damage into the rigid area that leads to the separation of the material underneath the indenter tip (zone 2) (Hill, 1953).

Similarly, a fracture model was proposed by Lawn (1975) for a brittle material subjected to the indentation loading by a sharp indenter (Figure 2.3). In that model, it was shown that the compacted area at the contact zone between indenter and material (zone 1) was expanded to create a median vent crack underneath the indenter tip. As a result of the further increase in the load, the crack propagated up to the final catastrophic fracture event.

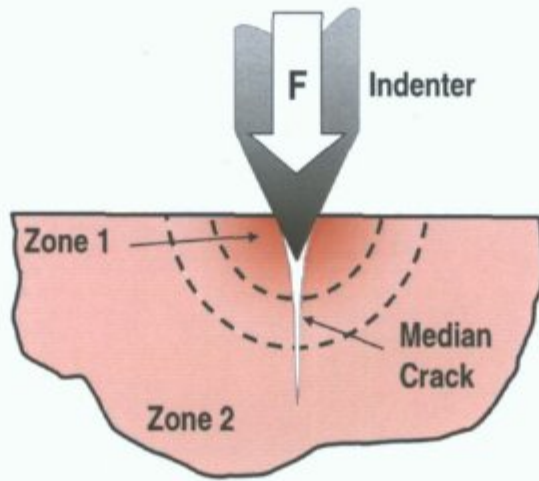


Figure 2.3: Lawn model of crack formation under indentation process in a brittle material (Lawn et al., 1975)

2.3 Structure of bone

The hierarchical structure of cortical bone has an effect on the fracture events and process occurring during loading of bone. Figure 2.4 shows the hierarchical structure of bone proposed by Rho et al. (1998).

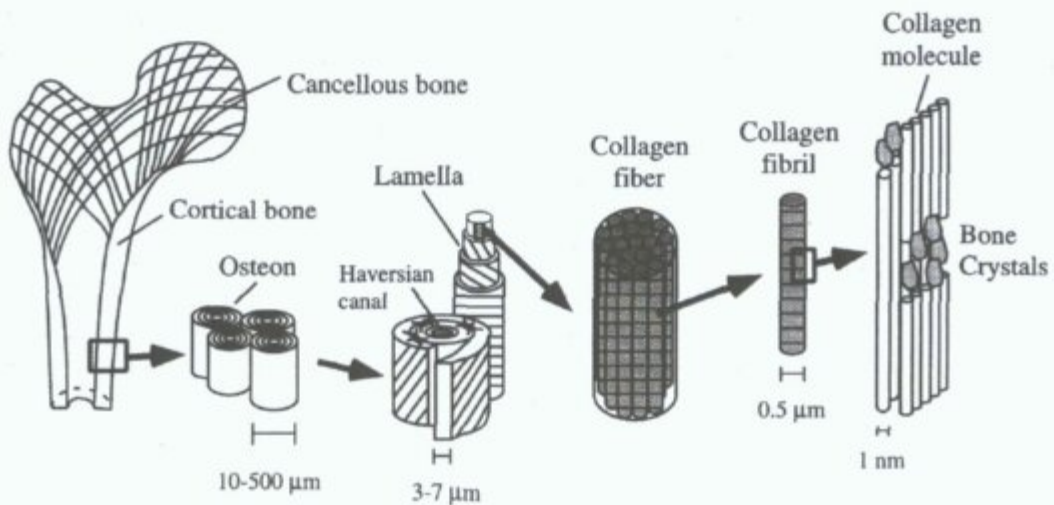


Figure 2.4: Hierarchical structure of bone (Rho et al., 1998)

2.3.1 Macroscopic structure of bone

At macroscopic level, the structure of bone is classified by shape into long, flat, short and irregular bones. Humerus, femur and tibia are examples of long bones in the human body. As shown in Figure 2.5, a long bone has a shaft which is called the diaphysis with two rounded ends known as the epiphysis. The diaphysis is made up of cortical bone surrounding the medullary cavity filled with bone marrow and the epiphysis has cancellous bone which contains red bone marrow. The inner surface of bone at the medullary canal is called the endosteum and the outer surface of the bone is known as the periosteum. The periosteum contains surface bone cells including osteoblasts, osteoclasts and lining cells. In short bones (wrist and ankle), the bone in the centre is wrapped by a hard shell of cortical bone and in flat bone (scapula), cancellous bone is sandwiched between two layers of cortical bone.

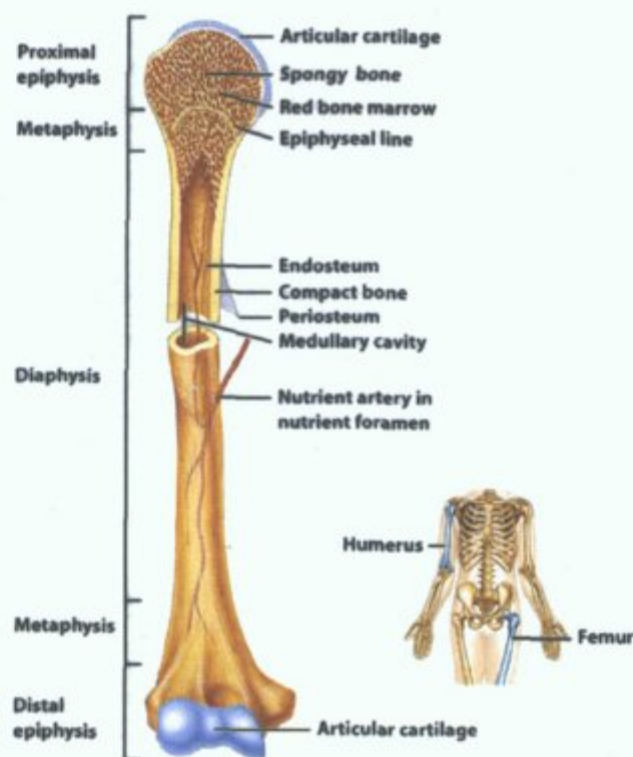


Figure 2.5: Schematic diagram of a long bone (Tortora and Derrickson, 2005)

2.3.2 Cortical and cancellous bone

Bone can be either compact (cortical) or cancellous (spongy or trabecular). Figure 2.6 shows a portion of long bone containing cortical and cancellous bone. Cancellous bone has a porous architectural structure (75%-95% porosity) and consists of may be oriented struts (trabeculae) which are approximately 200 μ m thick (Martin et al., 1999). This type of bone may be found in flat bones and the epiphyses of long bones. Cortical bone is very dense (5%-10% porosity) and can be found in diaphyses of long bones or around the periphery of cancellous bone. As shown in Figure 2.6, different bone structures may be found in an adult human cortical bone including secondary osteons, layers of primary circumferential lamellae, and interstitial bone (fragments of old existing osteons). In cortical bone, there are two main nutrient and blood supply canals including longitudinal Haversian canals (or central canal) and transversal Volkmann's canals (or perforating canals). Volkmann's canals connect Haversian canals to each other and to the bone surface. In addition to these canals, there are also canaliculi networks which connect osteocytes (bone cells) to each other.

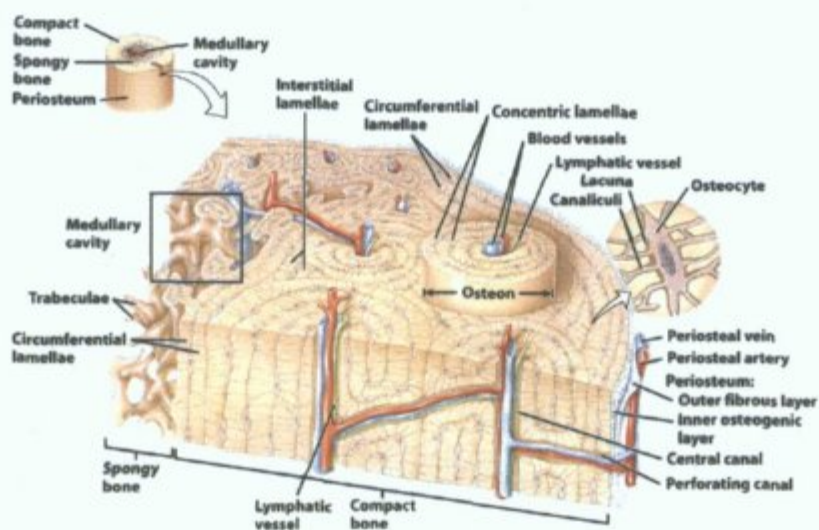


Figure 2.6: Diagram of a portion of a long bone shaft showing details of cortical and cancellous bones (Tortora and Derrickson, 2005)

2.3.3 Woven and lamellar bone

At the lower level, cortical bone can exist either as woven or lamellar bone. Woven bone is formed very quickly (more than $4\mu\text{m}$ a day) during initial ossification when new bone needs to be introduced (in embryo or fracture healing). This type of bone is made of randomly organised collagen fibres and it is more highly mineralised bone. Lamellar bone is a well-arranged bone that is laid down slowly (less than $1\mu\text{m}$ a day). Lamellar bone is formed by the planar arrangement of collagen fibres, which are called lamellae and it is less mineralised than woven bone.

Lamellar bone may be found in two forms; plywood and helicoidal structure (Martin et al., 1999). In the plywood structure, in each lamellae sheet, collagen fibres are parallel and oriented approximately in the same direction, while the fibre orientation in each lamellae changes to the next lamellae sheet as shown in Figure 2.7. In the helicoidal structure, there is a small and constant change in angle between lamellae sheets that makes it difficult to distinguish between individual lamellae. At this level there is another type of bone between woven and lamellar bone with collagen fibres arranged in a well-organised manner called parallel-fibred bone.

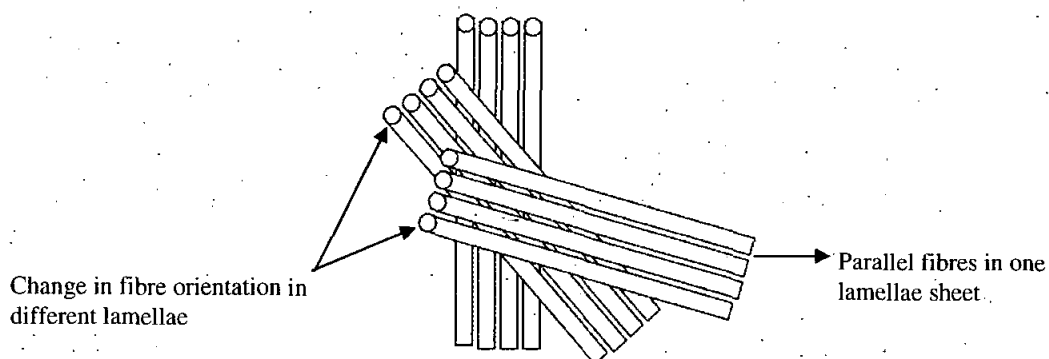


Figure 2.7: Fibre arrangements in lamellar bone

2.3.4 Primary and secondary bone

Both woven and lamellar bones were found in human and animal cortical bone in two forms of primary and secondary bone. There are two primary bones including circumferential lamellar in immature human bone and fibrolamellar (plexiform) in bovine bone. The secondary bone which is found in mature human bone is called Haversian bone.

In circumferential lamellar bone, beneath the surface of the bone (periosteum) concentric lamellae wrap the blood vessels to form the primary osteons. Fibrolamellar bone is a mixture of lamellar and woven bone. As shown in Figure 2.8, during the formation of fibrolamellar bone, the network of blood vessels at the surface are surrounded by quickly formed woven bone. This woven bone then will be replaced by concentric lamellae to form the primary osteons (Currey, 2002).

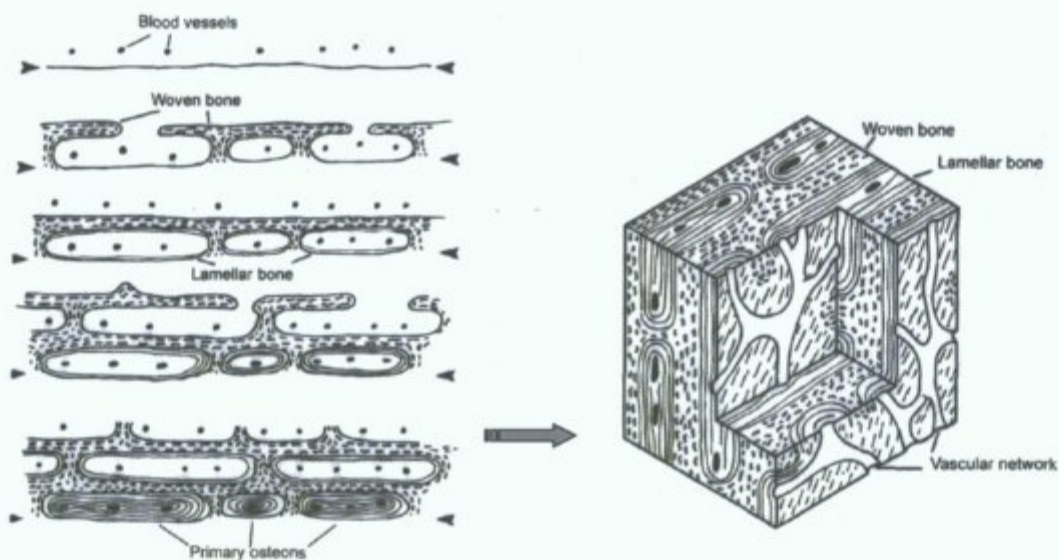


Figure 2.8: Diagram of fibrolamellar bone formation process (Currey, 2002)

The secondary Haversian bone is formed as a result of remodelling process (Figure 2.9). During the resorption phase of remodeling process, a tunnel like cavity is eroded by osteoclasts which is called “cutting cone” and it is approximately 200 μ m in

diameter and 300 μm in length (Martin et al., 1999). When the cutting cone is formed, osteoblasts begin to refill the internal surfaces by forming concentric lamellae during a refilling phase. A cement sheath (cement line) around the osteon is formed during a transition phase (reversal) between resorption and refilling processes. The Haversian canal is not completely filled and there is a 40-50 μm diameter tunnel cavity in the middle which acts as a vascular passage (Martin et al., 1999).

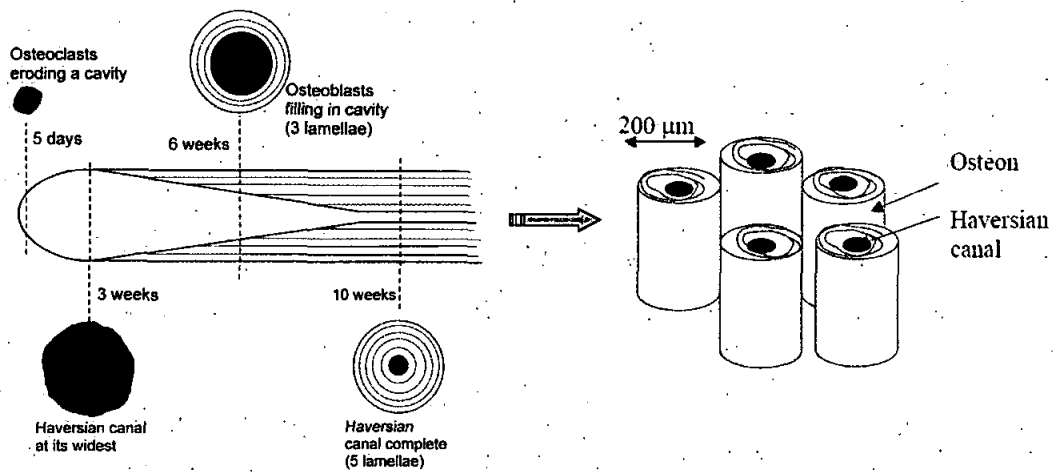


Figure 2.9: Diagram of osteonal bone formation as a result of remodelling process (Currey, 2002)

2.3.5 Molecular level of bone

At the molecular level, bone is composed of type 1 collagen, non-collagen proteins, calcium phosphate mineral (hydroxyl-apatite) and water. As seen in Figure 2.10, mineral crystals are deposited in the gap (approximate size of 67nm) between collagen molecules to form the collagen fibrils (Currey, 2002). These fibrils aggregate to form the collagen fibres which are known as the basic unit in woven and lamellar bone.

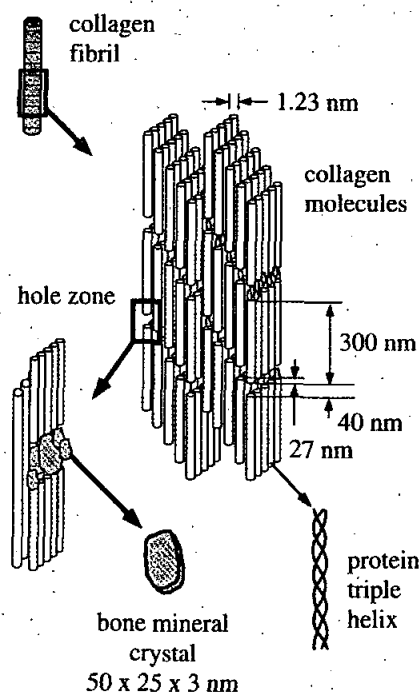


Figure 2.10: Schematic diagram of collagen molecules-mineral crystals interactions (Rho et al., 1998)

2.3.6 Bone cells

During bone formation process, osteoblasts, osteoclasts, and osteocytes are the main cell features. Osteoclasts are large cells which are originated from cells in the blood to destroy organic and mineral components (old existing bone) from the bone surface. Osteoblasts are derived from lining cells and are responsible for laying down the osteoid which is calcified during mineralisation process to form the new bone. These cells are not buried in newly formed bone and cover all bone surfaces in the collagenous sheet (periosteum). Osteocytes are osteoblasts trapped in the newly formed bone. As shown in Figure 2.6, they are located in the lacunae cavities and communicate with osteoblasts through the canaliculi channels.

2.4 Mechanical properties of bone

In the study of deformation and fracture in bone, the strength and stiffness are of fundamental importance. Force may be applied to the bone sample in various modes of tension, compression, bending and torsion. This brief review of mechanical properties of bone will focus on two basic modes including tension and compression.

2.4.1 Stress and strain

The effect of applied force to a solid object is referred to as a Stress (σ) and the resulting deformation as a Strain. Figure 2.1 shows the nature of compressive (a) and tensile (b) forces applied to a sample of material that decrease and increase the original length of the material respectively. In these cases, stress is defined as in Equation 2.1, where F is the applied force in Newtons (N) and A is the Cross-Sectional Area in m^2

$$\sigma = \frac{F}{A} \quad (\text{Eq. 2.1})$$

The resulting Strain (ϵ) is defined as in Equation 2.2, where L is the original length of the material and ΔL is the extension which is the change in original length in meters.

$$\epsilon = \frac{\Delta L}{L} \quad (\text{Eq. 2.2})$$

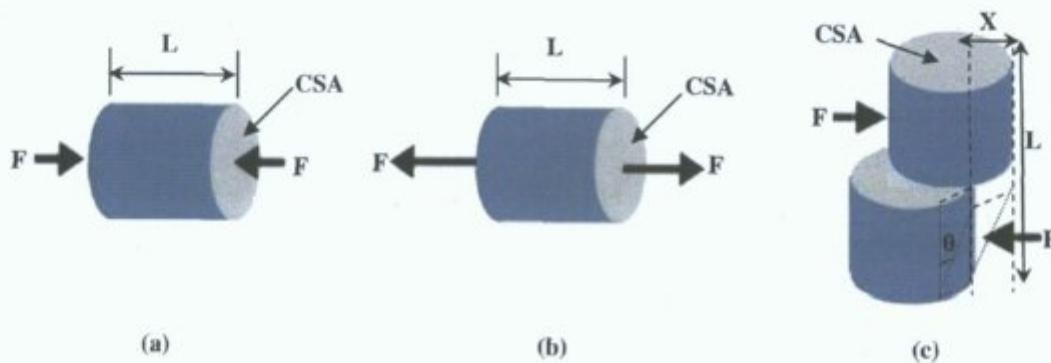


Figure 2.11: Compressive (a), tensile (b), and shear (c) stresses applied to an object

Where an object is subjected to shear force, the change in the shape of the material is measured by the change in the angle between the initially perpendicular sides of a differential element (Figure 2.11c). The shear strain (γ) is defined by Equation 2.3.

$$\gamma = \frac{X}{L} = \tan \theta \quad (\text{Eq. 2.3})$$

The rate of change of strain as a function of stress is called modulus of elasticity or Young's modulus (E) in a specimen subjected to compressive or tensile loading and is defined by Equation 2.4 within the linear portion of a stress-strain diagram (Figure 2.12).

$$E = \frac{\sigma}{\epsilon} \quad (\text{Eq. 2.4})$$

The ratio of lateral strain (ϵ_y) to axial strain (ϵ_x) in an axially loaded specimen is defined as Poisson's ratio (ν) and is defined by Equation 2.5.

$$\nu = -\frac{\epsilon_y}{\epsilon_x} \quad (\text{Eq. 2.5})$$

2.4.2 Stiffness and strength

As shown in Figure 2.12, a typical stress-strain curve may be split into three major regions up to the fracture point: 1) elastic region, 2) yield region and 3) plastic region (post-yield). In the initial elastic region, the relationship between force (or stress) and deformation (or strain) may be linear. The modulus of elasticity or Young's modulus (E) is defined as the slope of stress/strain curve in the elastic region. In this region, if the load is removed, the test specimen returns to its original size, which is called elasticity. When the curve bends over at the yield point, the material behaves plastically and strain is irrecoverable. If a material breaks without showing post-yield deformation, it is said to be a brittle material, conversely, a material with extended post-yield deformation is known as a tough material.

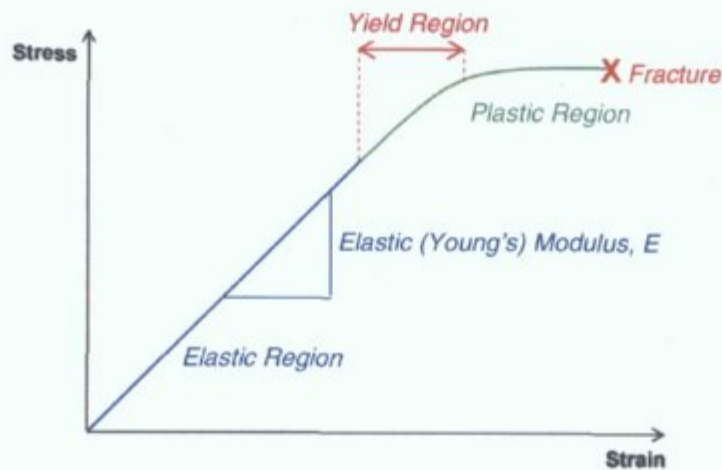


Figure 2.12: A typical stress-strain curve in a tensile test

As previously discussed in Section 2.3, bone has a hierarchical structure, so mechanical properties can be studied at different levels, however, in this review; the focus was on mechanical properties of cortical bone as a whole bone. Table 2.1 shows the mechanically determined elastic moduli values for human and bovine cortical bone femur from experiments produced by Reilly et al. (1974) and Reilly and Burstein (1975). As can be seen in the table, different Young's moduli values were found in different directions to the long axis of the bone (bone anisotropy). For example, human and bovine bones are less stiff in transverse directions than in longitudinal direction in tension and compression. The values in this table also show that bovine is stiffer than human bone in the longitudinal direction.

Elastic Modulus, GPa	Tension		Compression	
	Longitudinal	Transversal	Longitudinal	Transversal
Human Bones				
Haversian	17.7 ± 3.6	12.8 ± 3.0	18.2 ± 0.85	11.7 ± 1.01
Bovine Bones				
Haversian	23.1 ± 3.2	10.4 ± 1.6	22.3 ± 4.6	10.1 ± 1.8

Table 2.1: Elastic Moduli of cortical bone (Reilly et al., 1974; Reilly and Burstein, 1975)

Strength is the easiest way to study fracture in bone and can be directly measured by breaking a specimen under a monotonic load. Data in Table 2.2 is also taken from the classical literatures by Reilly et al. (1974) and Reilly and Burstein (1975). It was found that the strength of human and bovine cortical bone varied depending on the type of load applied. For example, bone is stronger in compression than tension regardless of loading direction and it is weaker when shear loads are applied in comparison to tensile loads. As seen in the table below, bone is generally stronger in the longitudinal than transverse direction.

Strength, MPa	Tension		Compression		Shear
	Longitudinal	Transversal	Longitudinal	Transversal	
Human Bones					
Haversian	133 ± 15.6	53 ± 10.7	205 ± 17.3	131 ± 20.7	67 ± 3.5
Bovine Bones					
Haversian	150 ± 11	54 ± 5.8	272 ± 3.3	171 ± 25	70 ± 9

Table 2.2: Strength properties of cortical bone (Reilly et al., 1974; Reilly and Burstein, 1975)

2.4.3 Fracture toughness

Fracture occurs when a crack is created and propagated to cause failure. According to Griffith theory, a crack can propagate when it meets two main criteria. Firstly, the tip of the crack which is highly stressed must maintain adequate stress up to the final fracture point (stress criterion), and secondly energy released by increase in crack length must be greater than the required energy for surface energy of new crack faces (thermodynamic criterion) (Pook, 2000). Surface energy is potential energy required to bond the atoms at the surface of the materials to other atoms and strain energy is a

potential energy that is released in a material during deformation as a result of crack propagation.

Most studies on bone fracture are concerned with linear-elastic fracture mechanics. In this approach, the inelastic behaviour is limited to regions near the crack tip while stress and displacement near the pre-existing crack are described by the stress intensity factor, K . The stress intensity factor can be defined for different modes of crack propagation in a pre-cracked material as illustrated in Figures 2.13 including Mode I, opening mode where opposing crack surfaces move apart from each other and crack propagation direction is perpendicular to tensile load direction; Mode II, sliding mode where crack surfaces move over each other and crack propagation direction is parallel to shearing forces, and Mode III, tearing mode where crack surfaces move over each other and crack propagation direction is perpendicular to the shearing forces.

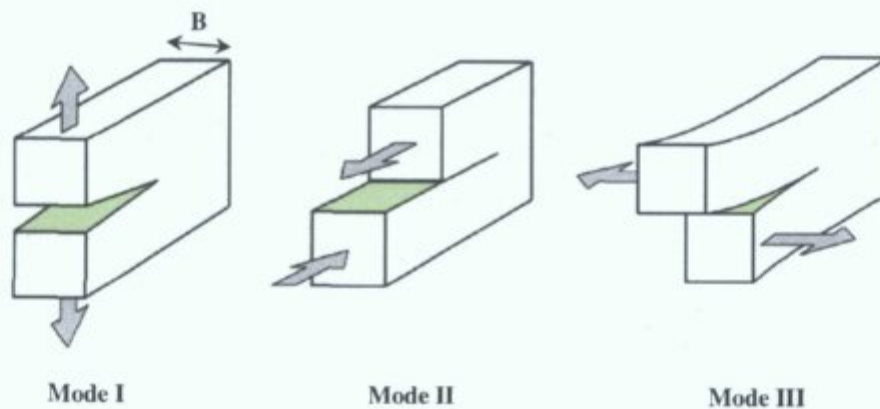


Figure 2.13: Modes of fracture in materials: (I) opening, (II) sliding & (III) tearing

Stress intensity factor (K) may be determined by the geometry of the crack, applied load, σ , and crack size, a , as follows (Pook, 2000):

$$K = Q\sigma\sqrt{\pi a} \quad (\text{Eq. 2.6})$$

Q is a dimensionless constant which depends on the geometry of the sample and mode of loading (Modes I, II and III in Figure 2.13). The resistance to fracture (fracture

toughness) can be measured when the stress intensity reaches the critical value, K_{IC} , at the onset of unstable crack propagation at the peak stress. Alternatively, the critical value of strain energy release rate, G_c , may be utilised as a measure of fracture toughness. The critical strain energy release rate is defined as the change in strain energy per unit increase in crack and it may be measured as (Pook, 2000):

$$G_c = P^2 / 2B(dC/da) \quad (\text{Eq. 2.7})$$

Where P is applied load, B the specimen thickness and dC/da is the specimen compliance with crack extension (the compliance is the slope of displacement-load curve).

Table 2.3 shows the typical mode I fracture toughness values obtained for bovine and human bone (Martin et al., 1999). As can be seen in the table below, fracture toughness properties of a bone specimen are determined by osteonal direction. It should be noted that crack propagation in the transverse direction to the long axis of the bone also turns to longitudinal direction immediately.

Bone type	K_{IC} MPa-m ^{1/2}	G_c Jm ⁻²	Source
Mode I transverse fracture*			
Bovine femur	5.49	3100-5500	Melvin and Evans 1973
Bovine tibia	2.2-4.6	780-1120	Bonfield and Datta 1976
Human tibia	2.2-5.4	350-900	Norman et al 1992
Mode I longitudinal fracture **			
Bovine femur	3.21	1388-2557	Melvin and Evans 1973
Bovine tibia	2.8-6.3	630-2238	Behiri and Bonfield 1984
Human femur	2.2-5.7	350-900	Norman et al 1992

* Crack propagates in the transverse direction to the long axis of the bone.

** Crack propagates in the parallel direction to the long axis of the bone.

Table 2.3: Fracture toughness properties of cortical bone (Martin et al., 1999)

2.5 Damage in cortical bone

Historically, cortical bone was assumed to fracture in linear elastic manner like brittle materials. However, this perception has changed recently since studies showed extensive post-yield damage under load due to microcracking (Currey and Brear, 1992; Zioupos et al., 1994).

Typically, fracture processes in bone can be separated into 3 distinct regions in a typical stress-strain curve as illustrated in Figure 2.14 (Currey and Brear, 1992). As can be seen in Figure 2.14, microcracking was rarely observed within the elastic phase (I) and the onset of microcracking was found to be associated with the yield phase. These microcracks accumulated in number during the plastic phase (II) and converted to a main crack which was propagated up to the final failure (III).

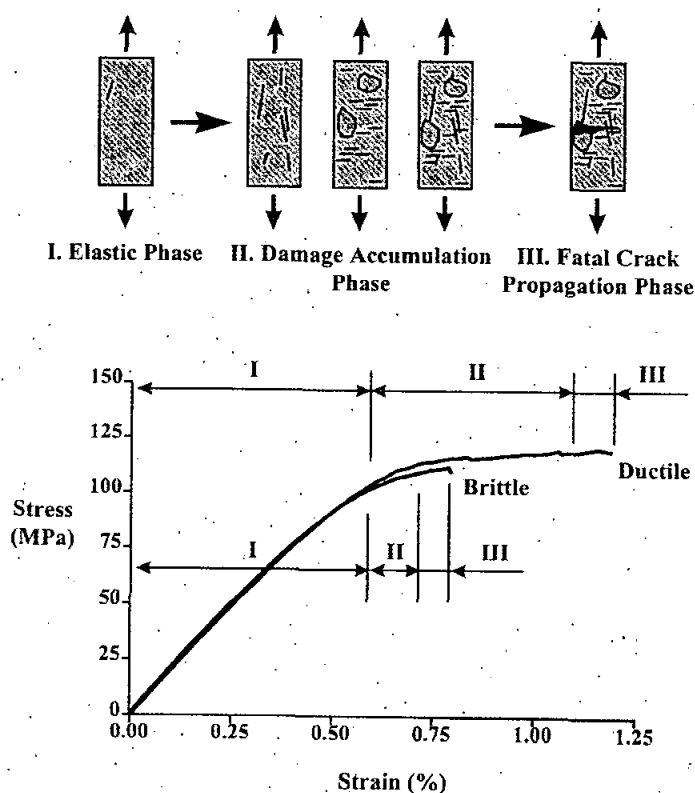


Figure 2.14: Segregation of stress-strain curve into elastic, damaging and fracture regions for cortical bone loaded in tensile mode (Currey and Brear, 1992)

2.5.1 Nature of microdamage

In vivo microdamage in cortical bone was found in the form of dispersed linear microcracks using standard bulk-staining method in the transverse sections of human ribs in old bones (Frost, 1960; Burr and Stafford, 1990). In 1960, Frost first reported the existence of linear microcracks in cortical bone with lengths of 100-200 μm . Years later, in a similar study; Burr et al. (1990) showed that these microcracks were found to be larger than canaliculi but smaller than vascular channels with a well stained sharp edge. Recently, O'Brien et al., (2000) demonstrated that microcracks were found to be longer in the longitudinal than transverse direction. They observed that microcracks in the longitudinal and transverse directions had approximate lengths of 400 μm and 100 μm , respectively.

Histological studies on old human osteonal bone showed that the majority of microcracks formed in interstitial bone (fragments of old existing osteons) and cement lines (marked in 1, 2, 3 in Figure 2.15), and rarely invaded into the osteons (Frost, 1960; Schaffler et al., 1995; Norman and Wang, 1997). Schaffler et al. (1995) reported that these microcracks increased with age in an exponential fashion.

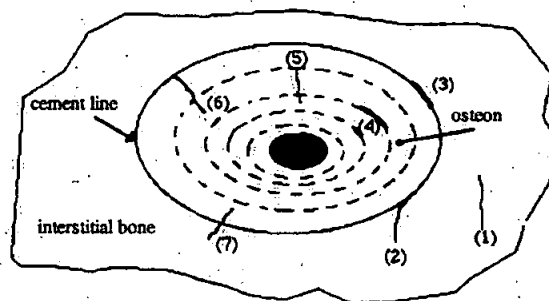


Figure 2.15: Sites of microcrack formation in osteonal bone (Norman and Wang, 1997)

The types of *in vitro* microcracks were found to be similar to *in vivo* microcracks (Schaffler et al., 1989; 1990). During *in vitro* fatigue loading of bone specimens from

bovine and human bone, distinctive types of damage were found depending on the modes of loading. The type of damage was found in the form of oblique cracks in the bone specimens subjected to compressive loading (Carter and Hayes, 1977; Reilly and Currey, 1999; Burr et al., 1998). It was observed that compressive microcracks were initially formed at vascular canals and interstitial bone, and then followed weak lamellae interfaces and cement lines (Carter and Hayes, 1977; O'Brien et al., 2003). The tensile microdamage was of two types; linear microcracks and diffuse damage. The linear microcracks with lengths longer than $100\mu\text{m}$ were found at the weak interfaces of cement lines and interlamellar bands (Carter and Hayes, 1977; Vashishth et al., 2000; Akkus et al., 2000). The diffuse damage was found in the form of arrays of fine microcracks (Zioupos et al., 1994; Burr et al., 1998; Reilly and Currey, 2000). These fine microcracks were approximately $2\text{-}5\mu\text{m}$ thick and $10\text{-}50\mu\text{m}$ long (Zioupos et al., 1994) and formed in the well-mineralised woven part of the bone (Zioupos et al., 1994) and/or around the osteocyte lacunae cavities (Reilly, 2000).

2.5.2 Effect of microcracking on mechanical properties

In several preliminary studies, microcracking was suggested to be associated with degradation of mechanical properties (Carter and Hayes, 1977; Schaffler et al., 1989; 1990). However, they were not able to correlate quantitatively between amount of microcracks and stiffness loss. Schaffler et al. (1990) reported that the loss of stiffness was associated with increase in microcracks densities in cyclically loaded bone specimens in tension. Later, Burr et al. (1998) carried out 4-point cyclic bending experiments on canine femurs and determined a nonlinear correlation between microcrack accumulation and stiffness loss. Consequently, the number of microcracks increased significantly at modulus reduction of greater than 15% (40% of specimens with stiffness loss of 15-25% and 60% with stiffness loss of greater than 26%).

2.5.3 Development of microcracks

Vashishth et al. (1997; 2000) showed 3 stage microcrack formation during crack propagation using a combination of fracture mechanics-based crack growth resistance tests and scanning electron microscopy on human and bovine cortical bone specimens (Figure 2.16). This crack propagation model showed that microcracks initially increased in number within a frontal process zone at a high stress concentration area (a notch) to create a main or macrocrack. This main crack subsequently propagated as a result of microcrack development into the wake zone and ahead of the crack tip.

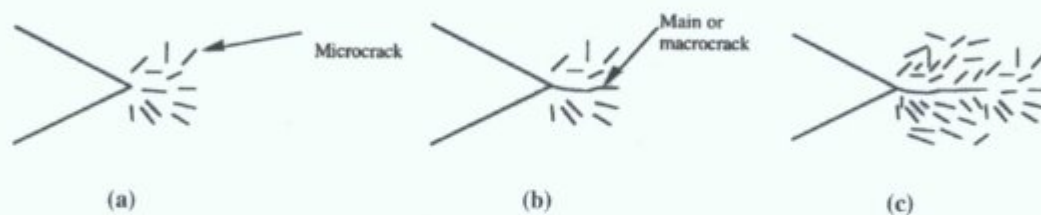


Figure 2.16: Model of crack growth processes in cortical bone (Vashishth et al., 2000)

Microcracking process was found to vary in bone specimens subject to the mode of load which was applied such as tension, compression and torsion. Burr et al. (1998) performed 4-point bending tests on whole canine femurs and found that the tensile loading mode produced more microcracks than compressive loading. Reilly et al. (1999) showed that tensile microcracks occurred at lower strains, grow in density and do not become a macrocrack (longer than $100\mu\text{m}$) when a higher strain is reached, while compressive microcracks formed at higher strains when initiated and become macrocracks quickly. A main or macrocrack may grow to final failure in different ways subjected to different mechanical components of loading as shown in Figure 2.17 for longitudinally oriented specimens of bovine bone (George and Vashishth, 2005). As can be seen in Figure 2.17, the tensile loaded specimens showed mode I cracking and 3 stages of low threshold crack initiation, steady crack propagation and final failure. Conversely, compression showed mode II cracking and two stages of

high threshold crack initiation and a sudden final fracture. Torsion showed mode II and III microcracking and time-dependant damage.

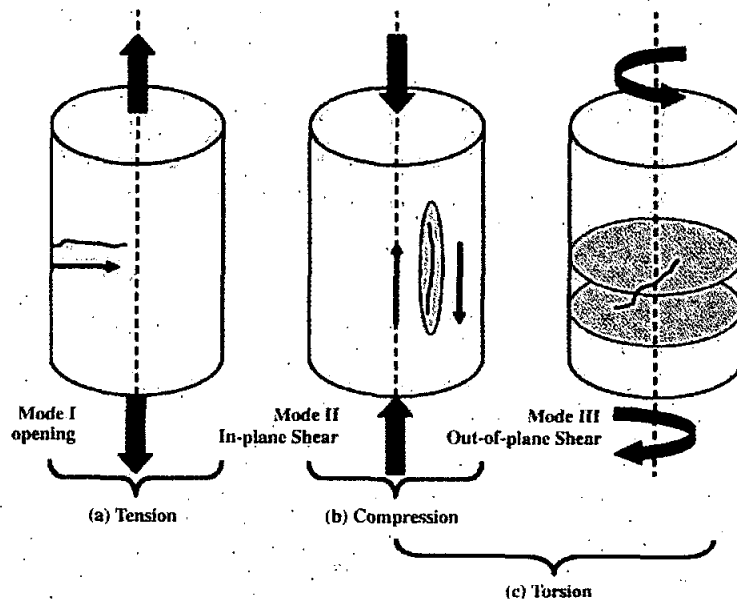


Figure 2.17: Macrocrack growth subjected to various modes of load (George and Vashishth, 2005)

2.5.4 Effect of cortical bone structure on microcrack development

The cement line, lamellar and osteonal structure of the bone are microstructural elements that are thought to play an important role in both micro and macrocrack formation and growth. In 1994, Zioupos and Currey observed that microcracks did not grow in a straight-line due to the barrier effect of the strong lamellar structure around the blood vessels during fatigue testing of bovine bone specimens. Later, Jepsen et al. (1999) reported that new microcracks formed in isolation from each other between the weak interfaces of lamellae in human bone specimens subjected to fatigue torsion loading. A greater number of microcracks were found in bovine compared to human bone specimens during fatigue loading (Vashishth et al., 2000). In that study, it was highlighted that the majority of microcracks in human bone were preferentially oriented in the longitudinal direction which were associated with weak interfaces of lamellae, while in bovine bone lamellae boundaries were stronger and the dominant

damage type was oblique oriented osteon failure. A number of studies on bovine cortical bone specimens subjected to fatigue loading (Akkus and Rimnac, 2001; O'Brien et al., 2003; 2005) and monotonic loading (Hazenberg et al., 2006) showed that propagating macrocracks were arrested or deflected at the cement line where they encountered the secondary osteons (Figure 2.18). Thus, it was concluded that the barrier effect of osteons results in slower crack growth. O'Brien et al. (2003) reported that only 8% of initially formed microcracks at interstitial bone were capable of propagation due to the crack-arresting barriers in osteonal bone. These researchers also showed that microcracks longer than 100 μm could propagate to become longer (300 μm) to invade into the osteons and cause the final failure (O'Brien and Taylor, 2005).

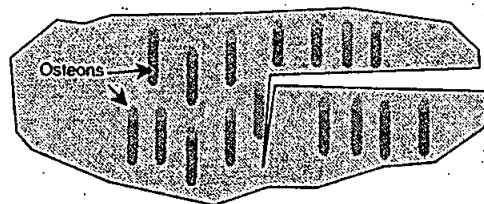


Figure 2.18: Crack deflection at the secondary osteon boundary in cortical bone (Ritchie et al., 2005)

2.5.5 Toughening mechanisms in cortical bone

As discussed previously in Section 2.5.3, microcracking has been suggested as a major toughening mechanism in human and bovine cortical bones by Vashishth et al. (1997; 2000; 2003) (Figure 2.19).

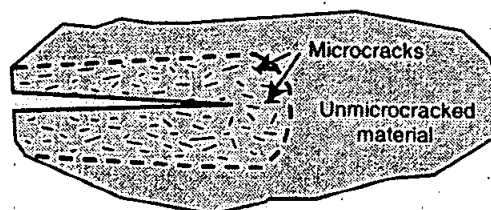


Figure 2.19: Microcracking toughening mechanisms during crack growth in cortical bone (Ritchie et al., 2005)

These researchers described the fracture toughness based on a resistance-curve (R-curve), where toughness was assessed with increase in crack length. A linear increase in fracture toughness and cumulative number of microcracks were found with the increase in the length of the main crack in human and bovine cortical bone (Vashisht et al., 1997).

Recently, Nalla et al. (2004; 2005) suggested that crack bridging is the primary mechanism in human cortical bone to resist crack opening. As shown in Figure 2.20, crack bridging is the formation of unbroken regions resulting from unbroken collagen fibres and/or uncracked ligaments due to non-uniform crack advance or where a propagating crack tends to link-up with microcracks ahead of the crack tip. Similarly, the uncracked ligament bridging was observed in bovine bone specimens subjected to monotonic tensile loading and called terracing effect (Hazenberg et al., 2006).

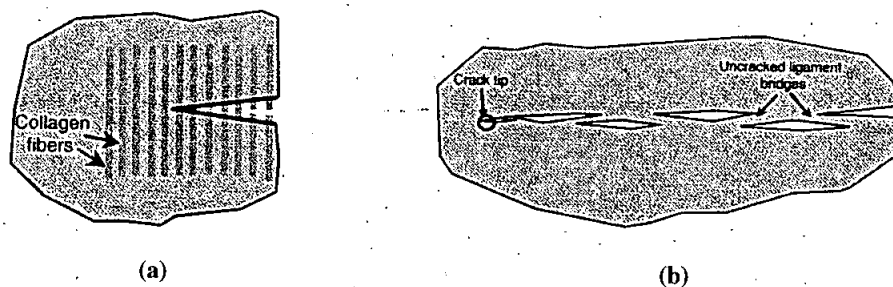


Figure 2.20: Bridging effect as a toughening mechanism in cortical bone: (a) crack bridging and (b) uncracked ligament bridging (Ritchie et al., 2005)

2.5.6 Damage process in cortical bone during the cutting process

During high speed orthogonal machining of bovine bone, Jacobs et al. (1974) showed that there is a preferred direction for crack growth in the longitudinal direction parallel to Haversian canals due to the weak interfaces between osteons. This observation was confirmed by Wiggins et al. (1978) and a higher cutting force was found during the cutting processes in the transverse than longitudinal direction.

The models of crack growth subjected to indentation cutting have been previously discussed in Section 2.2 for brittle and ductile materials. In attempts to apply these models to bone, a recent experiment has been carried out by Reilly and Taylor (2005a; 2005b) to monitor crack growth processes using sequential fluorescent labelling and UV light microscopy in both longitudinal and transverse directions in bone specimens subjected to low speed indentation cutting process (Figure 2.21). This research highlighted that damage occurred with different stages of the loading process and cracks had a tendency to propagate in the longitudinal plane of the bone between the weak interfaces of lamellae in both longitudinal and transverse directions. However, it was found to be difficult to clearly monitor stages of crack growth as the main crack propagates quickly during the final fracture phase. They also found that the damage zone associated with micro and macrocracks between lamellae was more extensive in the transverse than longitudinal direction.

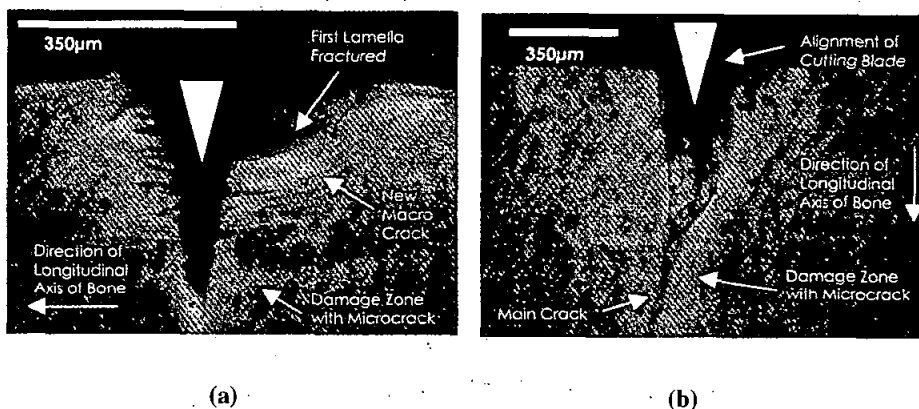


Figure 2.21: Indentation crack growth processes in bovine cortical bone: (a) longitudinal crack growth and (b) transverse crack growth (Reilly et al., 2005a)

2.6 Bone damage observation techniques

Bulk staining of the bone specimens in basic fuchsin has been the most popular method for microcrack detection under conventional microscopy in *in vivo* studies (Frost, 1960; Burr et al., 1985; Burr and Stafford, 1990; Schaffler et al., 1995;

Norman and Wang, 1997; Lee et al., 2000; O'Brien et al., 2000; Akkus et al., 2000; Zioupos et al., 2001). Figure 2.22 shows a detected microcrack using standard basic fuchsin method.

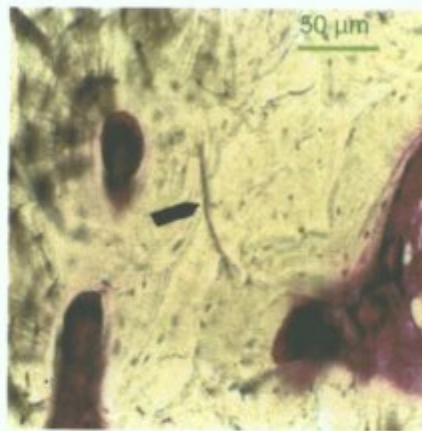


Figure 2.22: Fuchsin-stained microcrack (Burr and Stafford, 1990)

In 1960, the standard en-bloc staining method was introduced by Frost. In this method, bone specimens were bulk-stained in basic fuchsin agents for several weeks which allowed the staining agents to diffuse into the microcracks. After cutting and grinding of rehydrated bone into the thin sections (30-50 μ m thick), microcracks were viewed under light microscope. Burr et al. (1990) confirmed the success of the basic fuchsin staining method and demonstrated that dehydration of bone in alcohol during the staining process did not cause artefactual microcracks. Successful observations of basic fuchsin stained microcracks under microscopy was evaluated by SEM imaging of gold-coated (Burr et al., 1985) and lead-uranyl labelled thin sections of human ribs (Schaffler et al., 1994).

Recently, sequential labelling using a series of fluorescent chelating agents was utilised to monitor the stages of microcrack development and crack growth processes in bovine bone specimens under *in vitro* cyclic loading (Lee et al., 2000; O'Brien et al., 2000; 2002; 2003; 2005). In this technique, prior to testing, specimens were stained with alizarin to detect pre-existing microcracks and then other agents in the

order of xylenol orange, calcein and calcein blue were applied to specimens at loading steps prior to final failure and the labelled damage was viewed under UVepifluorescence microscopy. Figure 2.23 shows stages of a microcrack growth which is initially labelled with Xylenol orange and subsequently with Calcein at later fatigue loading levels.

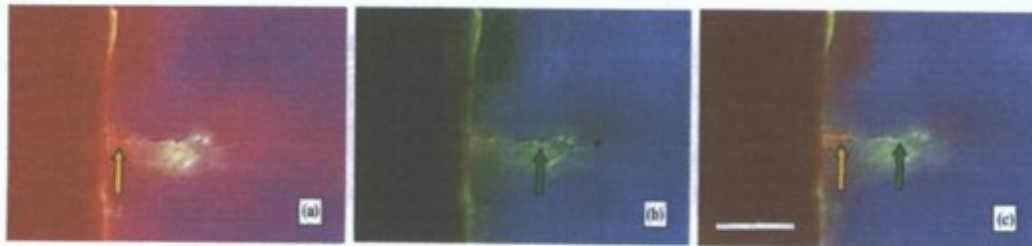


Figure 2.23: Stained developing microcrack using fluorescent sequential labelling method (O' Brien et al., 2002)

Scanning Electron Microscopy (SEM) was used to examine fracture surfaces of fractured specimens as well as monitoring the stages of surface crack growth in the specimens subjected to a standard fracture toughness test (Carter and Hayes, 1977; Xiaodu Wang, 1996; Vashishth et al., 1997; 2000; Nalla et al., 2004; 2005).

Laser Scanning Confocal Microscopy (LSCM) is a non-destructive technique which has been used to visualise microcrack development phases during *in vitro* cyclic loading of bone specimens whilst being immersed in a fluorescent agent (Zioupos et al., 1994; Reilly and Currey, 1999; Reilly, 2000; O'Brien et al., 2000). The advantage of this method is obtaining serial slices of optical images at chosen depths inside the labelled specimens without damaging the specimens. The limitation with LSCM technique is that the depth through which crack could be imaged may be limited to 0.3 mm due to the laser beam attenuation in bone structure (Zioupos et al, 1994).

2.7 Acoustic emission technique

Acoustic emission testing is a non-destructive technique (NDT) with capabilities for real-time monitoring of growing cracks in materials subjected to external load. Acoustic emission signals (AE hits) are defined as transient elastic waves in the range of ultrasound between 20kHz and 1200kHz. Frequency is measured in Hertz (Hz), where 1Hz = 1 cycle per second. As shown in Figure 2.24, AE signals propagate from the source in all directions and are detected on the surface of a test-piece by use of a piezoelectric sensor which converts them to electrical signals. After sensing, AE signals are amplified and sent to main AE processor for event detection and signal conditioning.

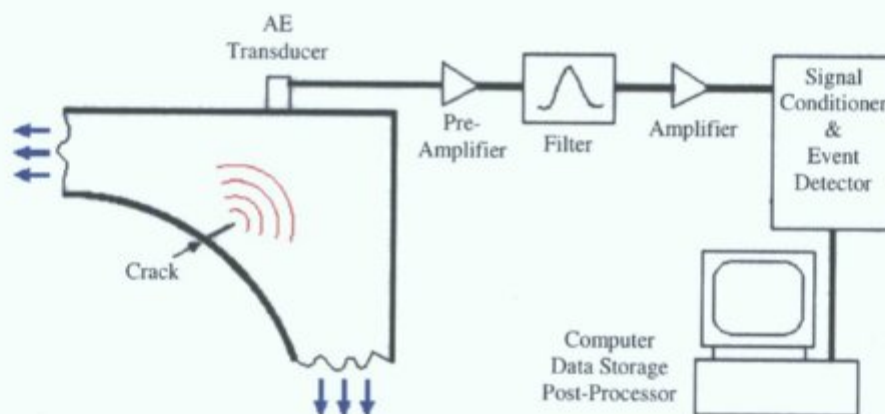


Figure 2.24: Process of generation of acoustic emission signal, detected by a typical AE system setup (<http://www.tms.org/.../Huang-9811.html>)

An AE event can be detected when the AE transducer senses a signal over the threshold value. A typical AE signal from a single crack is a burst type signal as shown in Figure 2.25 based on the time domain. Various AE signals features may be extracted in the AE processor during an AE test such as amplitude, duration, rise time and energy.

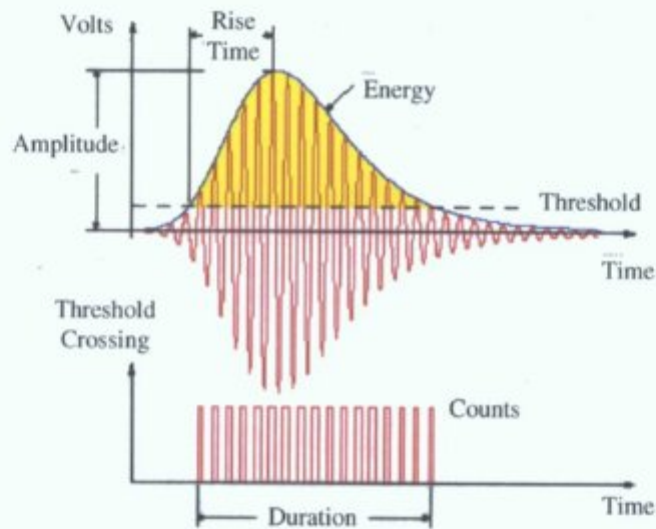


Figure 2.25: AE hit feature extraction diagram (<http://www.tms.org/.../Huang-9811.html>)

The following are the typical AE parameters to characterise an AE event:

- Amplitude:** This is the most important feature of an AE signal, which is defined as the highest (maximum) peak voltage on the voltage-time waveform. Amplitude is related to the strength of the AE event and expressed in Decibel (dB), one tenth of a Bell. Decibel is not a fixed measurement unit but rather expresses a logarithmic ratio between two conditions of the same dimension (i.e. voltage). For an AE signal, amplitude is calculated by the relationship shown in Equation 1, where V_p is peak signal voltage input in mV and G_p is the preamplifier gain and 0dB_{AE} is referenced to $1\mu\text{V}$ at the sensor before any amplification (Moore et al., 2005):

$$A (\text{dB}_{\text{AE}}) = 20 \log (V_{\text{max}} / 1 \mu\text{V}) - G_p \quad (\text{Eq. 2.8})$$

- Threshold Crossing Counts:** The voltages above the threshold line are related to the actual event and called threshold crossing counts (or ring down counts). This feature depends on the magnitude of the AE events. The values below the threshold are the unwanted signals which are removed either during test or post-test.

- **Duration:** The time of occurrence of an AE event in microseconds from first to the last count. It depends on the magnitude of the AE event source similar to threshold crossing counts.
- **Rise Time:** The time between the first count to the signal peak amplitude (reported in microsecond).
- **MARSE (measured area under the rectified signal envelope):** It is derived from the rectified voltage signal over the duration of the AE hit (waveform) with voltage-time units and it is strongly sensitive to amplitude and duration. MARSE is dependant on gain, and so the resolution may be different depending on the chosen gain.
- **Absolute Energy:** It is similar to the MARSE, while it is not dependant on gain and is a true energy value for an AE hit. This feature is driven from the integral of the rectified squared voltage signal divided by the reference resistance (10k-ohm) over the duration of the AE waveform.

2.8 Acoustic emission studies on cortical bone

The AE technique has been usually applied to the whole or machined bone specimens in monotonic loading subjected to various modes including bending (Hanagud et al., 1973; Hanagud and Clinton, 1977; Thomas, 1977; Yoon et al., 1980), torsion (Netz et al., 1980), compression (Hasegawa et al., 1993), tension (Hanagud and Clinton, 1975; Knet-s et al., 1975; Wright et al., 1981; Fischer et al., 1986; Zioupos et al., 1994) and shear (Nicholls and Berg, 1981). A number of AE studies were also conducted in fatigue (cyclic) loading conditions such as torsion (Jonsson and Eriksson, 1984) and tensile fracture toughness tests (Rajachar et al., 1999; Akkus et al., 2000).

2.8.1 AE during fracture processes in cortical bone

In 1973, Hanagud et al. successfully captured early AE activity prior to final fracture in machined bovine femora specimens subject to bending loading. The onset of AE activity was found to vary in AE studies on bone. In the studies carried out by Nicholls and Berg (1981) on rabbit tibia specimens in shear loading, the first AE signal was recorded at 50% of the failure load, while in other research, bone specimens subjected to tensile loading did not show AE activity until 88% of the failure load (Fischer et al., 1986).

For the first time in 1975, during tensile loading of human femur specimens, Knet-s et al. (1975) found that the number of AE signals increased gradually as a result of microcrack accumulation at initial stages of the loading. They reported that during final stages of the fracture process, a significant increase in the number of AE signals was related to the increase in the number of microcracks as well as creation of macrocracks. AE studies on bone typically showed that microcracking during the yield and plasticity phases initially produce AE signals which subsequently led to a significant AE activity at final fracture phase (Netz et al., 1980; Wright et al., 1981; Nicholls and Berg, 1981; Jonsson and Eriksson, 1984; Zioupos et al., 1994). During fatigue loading of dog bone, it was shown that AE signals were mostly produced by newly formed microcracks and/or existing crack growth during unloading phase (Jonsson and Eriksson, 1984). Zioupos et al. (1994) applied AE to bone specimens subjected to monotonic tensile loading and showed a burst of AE signals at yield phase as a result of initial microcracking, followed by a quiet phase during plasticity leading to a significant amount of AE activity during final fracture phase. Fracture toughness tests on human cortical bone specimens demonstrated that increase in total

number of AE hits was directly associated with the main crack growth processes via post-test histological observations (Akkus et al., 2000).

Wright et al. (1981) demonstrated that microcracking during the yield phase produces low amplitude AE signals; whereas fracture-related events generate high amplitude burst type signals during uniaxial loading of bovine bone specimens. Yoon et al. (1980) reported that these fracture-related events had high amplitude values in the range of 65-100dB in bovine femora samples loaded in bending. In a recent study by Akkus et al., (2000), it was found that a lesser amount of higher energy AE hits in the range of 70-90 dB was emanated from main crack growth itself, while linear microcracks and diffuse damage produced a large number of lower energy AE hits in the range of 40-70dB.

2.8.2. Parameters that affect AE response in bone

It has been demonstrated that AE response in bone under load varied with bone density (Hanagud and Clinton, 1975), composition (Wright et al., 1981), strain rate of loading (Fischer et al., 1986), type of bone (Zioupos et al., 1994) and direction of the load applied to the long axis of the bone (Akkus et al., 2000). The results of a study comparing AE response from lower density and normal bone specimens subjected to tensile loading (Hanagud et al., 1973) showed that a greater number of AE signals at smaller load levels were registered in bone specimens with lower density. In comparison of AE activity from defect-introduced and perfect bovine femora loaded in bending, it was observed that in bone samples with defects most of signals were low amplitude (less than 60dB) compared to normal bone which showed fracture-related AE signals over 80dB. Wright et al. (1981) applied AE testing to normal, decalcified and deproteinised bones subjected to tensile loading. In decalcified bone, low amplitude signals were registered during the nonlinear region prior to final

fracture point, however, brittle deproteinised specimens showed AE activity just at final fracture phase. Thus, these researchers suggested that during bone fracture processes, within the post yield region, damage of collagen fibers produced lower amplitude AE signals, followed by mineral crystals breakage at final fracture producing higher amplitude AE signals. Fischer et al. (1986) investigated the effect of strain rate on AE activity on bovine bone specimens subjected to tensile loading at two different strain rates (0.01 s^{-1} and 0.0001 s^{-1}). They found that loading at higher strain rate produced lower amplitude signals. During tensile loading of specimens from human and antler bone, a greater number of higher amplitude signals were registered in tougher bone (Zioupos et al., 1994). It was highlighted that the final failure event showed higher amplitude signal in human than antler bone. Fracture toughness tests conducted on human cortical bone specimens in the transverse and longitudinal directions to the osteonal arrangement showed that a higher number of AE signals were generated during crack growth processes in the transverse direction which was two times tougher than longitudinal direction (Akkus et al., 2000).

2.9 Acoustic emission studies on other materials

Acoustic emission activity from crack growth is of the greatest interest for practical NDT application of the AE phenomena and typically conducted on notched specimens in fatigue loading as discussed in the following sections.

2.9.1 AE studies on titanium alloy and steel materials

A model of fatigue crack growth has been proposed by Kohn et al. (1992a; 1992b) based on change in AE hit rate coinciding with extension of the crack length during fatigue tension loading of Ti-6Al-4V:

- 1) Crack initiation indicated by early AE;

- 2) Stable crack growth coincided with gradual increase in AE rate;
- 3) Unstable fast crack growth leading to final fracture indicated by sudden increase in amount and rate of AE.

In that research, crack initiation was identified when a high peak AE hit of 70dB was detected. Lower amplitude signals in the range of 55-65dB were observed during initial plastic deformation before crack propagation, followed by higher amplitude signals at the average of 72dB just prior to and at maximum load during final failure (100dB signal at fracture point). It was reported that during the damage process, high amplitude burst type signals were related to cleavage fracture events in 7075-T6 aluminium (Bianchetti et al., 1976). Later, fracture toughness testing of titanium alloy showed that low amplitude AE hits during crack growth were related to microcrack formation ahead of the crack tip (Mashino et al., 1996).

Fatigue tensile testing of Nickel-based Incoloy 901 specimens showed that the significant increase in the number of AE signals just prior to maximum load at failure was directly related to main crack growth (Berkovits and Fang, 1995). They found a nonlinear relationship between AE counts and crack growth rate. In other research, during tensile loading of steel material specimens, a poor correlation was found between AE hit accumulation and steady crack propagation rate due to the existence of other AE sources, not just advance of the main crack itself during fracture processes (Roberts and Talebzadeh, 2003).

2.9.2 AE studies on bone cements

In recent AE studies on bone cement subjected to fatigue loading, AE hits with higher durations and energies were observed during final failure phases (Roques et al., 2004; Jeffers et al., 2005). Jeffers et al. (2005) reported that the last AE hit at maximum load had the highest duration of approximately 4000 μ s. Roques et al. (2004) showed

that loading at higher stress rate generated a lower number of AE hits with smaller rise time and duration values.

2.9.3 AE and failure mode detection in composite materials

Various modes of failure mechanisms during fracture processes have been identified based on amplitude of the AE signals. A higher amplitude range of 70-100dB was found to be caused by fracture-related AE events; in contrast, lower range amplitude of 40-70dB coincided with matrix microcracking and possible friction (Bakuckas and Awerbuch, 1987). AE technique was applied to titanium matrix composites subjected to tensile loading and it was showed that high amplitude signals of 90dB were caused by fibre fracture, but lower amplitude signals smaller than 70dB were found to be caused by fibre/matrix debonding and fibre sliding (Fang et al., 2000).

2.9.4 AE activity in materials during the indentation loading

Surprisingly, a limited number of investigations on the indentation cracking process in materials have been found in literature. Indentation loading of platelet ceramic composite showed that the number of AE hits and related energy increased significantly during crack growth process to overcome the crack stoppage mechanisms (platelet resistance) (From et al., 1995). During indentation of aluminium foams using a cylindrical punch, it was found that initial deformation (densification) generated continuous low amplitude signals in the elastic region, while main crack growth produced detectable burst type signals with higher amplitude (Kadar et al., 2004). Cyclic indentation testing on ceramic materials demonstrated that during the unloading phase, when densification was relieved, a greater number of AE signals were recorded as a result of a faster crack growth (Ray et al., 1996).

2.9.5 AE activity and fracture energy

In attempts to correlate between amount of fracture energy and AE activity parameters, Fitz-Randolph et al. (1972) could not find a good relationship between these measures in composite materials under load, however, fracture tests on concrete materials showed that the sudden rise in AE energy just before maximum fracture load was directly correlated with maximum fracture energy as a result of an unsteady crack growth process (Landis and Ballion, 2002).

2.10 Summary

The following key issues were found in this literature review and are relevant to this research work:

- During the indentation cutting process of both brittle and ductile materials, there is a plastic deformation around the tip of the blade prior to crack formation.
- During damage processes in cortical bone, microcracks accumulate in number to create a main or macrocrack.
- Acoustic emission (AE) technique is a useful method to monitor the stages of damage accumulation and crack growth processes in real-time in various materials under mechanical load.
- In cortical bone, microcracking can be detected using the AE technique at early stages of fracture processes.
- The number of damage-related signals increases significantly just prior to final fracture as a result of a main crack propagation in cortical bone.
- During fracture process in cortical bone, microcracking produces lower energy signals, whereas macro crack growth events generate higher energy signals.

Chapter 3: Materials and Methods

3.1 Scope of the experimental work

This work has investigated the capabilities of Acoustic Emission (AE) techniques to detect crack initiation and propagation phases during indentation fracture processes in small cubic cortical bone specimens under monotonic indentation cutting load. To accomplish this, both AE signal features and load-displacement data were recorded simultaneously during the tests. The general AE analysis approach used in this work was based on hit-based features such as amplitude, duration and abs-energy. Attempts were made to capture the first high amplitude AE signal to detect crack initiation as an early indication of the main crack growth processes.

3.2 Overview of the experimental set up

Figure 3.1 shows a schematic arrangement used in this experimental work. A wedge type blade was used to apply a cutting force to the bone specimens using a mechanical testing machine (Hounsfield) under displacement-controlled conditions. Bone specimens were fixed into a specially designed fixture which was mounted on a Kistler dynamometer to record cutting forces.

During the test, crack-related AE signals in the bone specimens were detected by a miniature AE sensor (PICO type, manufactured by Physical Acoustic Limited (PAC)), amplified by amplifier (2/4/6 type, manufactured by PAC) and processed in AE DAQ card (PCI-2 type, manufactured by PAC). The indentation cutting force was measured simultaneously by the Kistler dynamometer and fed into the parametric channel on the AE DAQ card in conjunction with AEWIn software developed by PAC.

- | | |
|---------------------------|-----------------------------|
| 1) Wedge angle type blade | 5) Preamplifier |
| 2) Cubic bone specimen | 6) Kistler dynamometer |
| 3) Bone-holding fixture | 7) Dynamometer control unit |
| 4) AE miniature sensor | 8) Computer system |

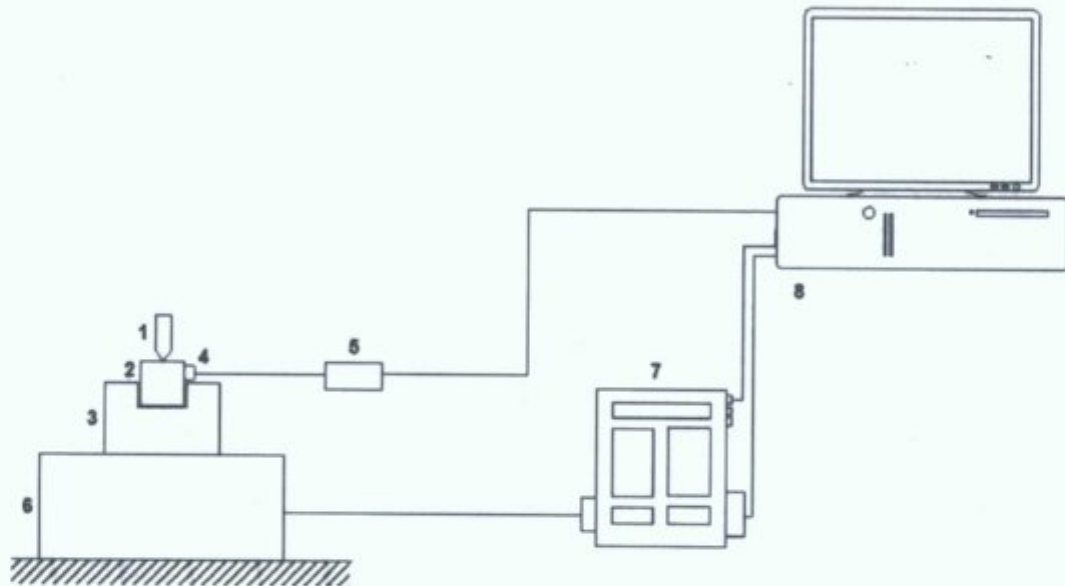


Figure 3.1: Schematic of the experimental arrangement

3.3 Specimen preparation

Whole bones from fresh bovine femora were obtained from an animal slaughterhouse and soft tissues were removed from the bone surface with caution to avoid damaging the surface. In this experimental research, small cubic specimens were prepared as it is the easiest specimen shape to machine.

After removing the ends (epiphyses part) from the whole bone using an electric circular bone saw, the mid-diaphyses part was machined into longitudinally oriented beams (8mm x 8mm x 110mm) using a milling machine (Semco) and the longitudinal axis was marked. A low-speed diamond wafering saw (Buehler Isomet, Buehler) was utilised to cut the bone pieces into the cubic specimens for the experiments.

As illustrated in Figure 3.2, the beam of bone was placed into the sample-holding fixture and cut into equal 8mm sections along the marked longitudinal direction. During the preparation process of the cubic bone specimens, it was required to irrigate the bone to prevent dehydration as this may affect mechanical properties of bone.

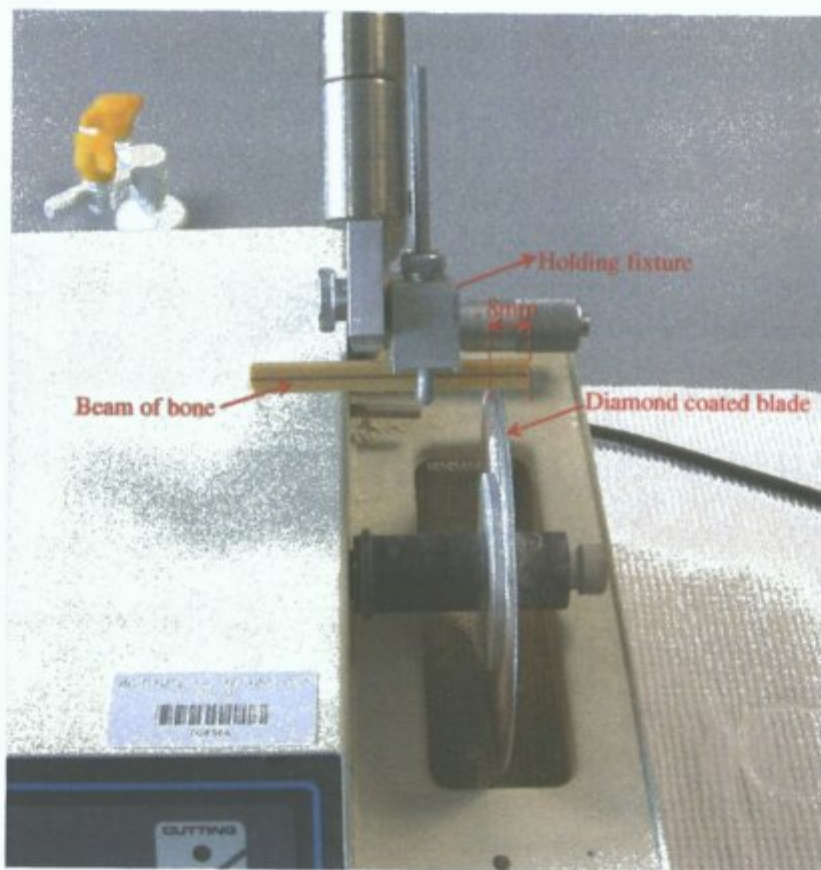


Figure 3.2: Longitudinal sectioning of bone pieces into 8mm cubic specimens using low-speed saw

Specimens were placed in plastic bags and stored frozen at -20°C until the time of testing, the date of storage and details of bone specimens were clearly labelled on the plastic bags to eradicate error during testing. Prior to testing, specimens were thawed in moist gauze and held under a damp cloth to prevent dehydration. The summary of the process of specimen preparation is illustrated in Figure 3.3. The blue line on the specimen shows alignment of the longitudinal direction.

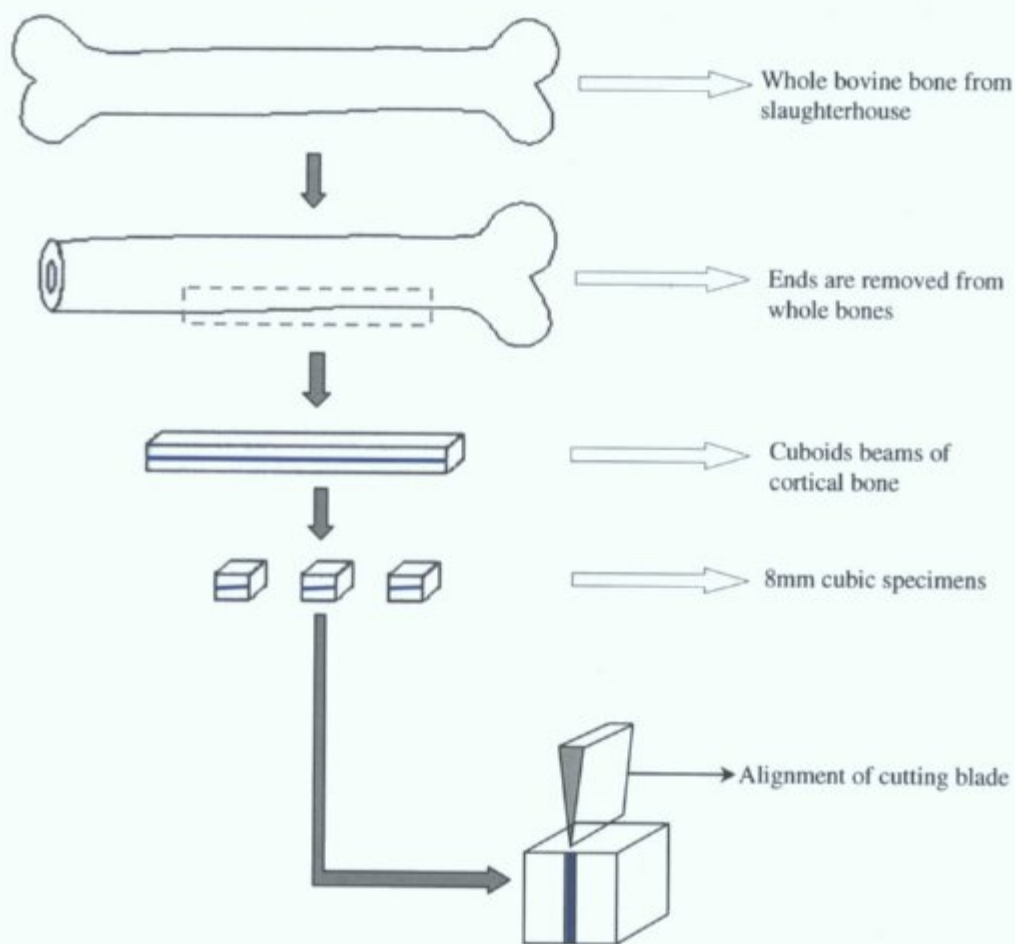


Figure 3.3: Preparation procedure for 8mm cubic specimens

3.4 Materials used in this work

3.4.1 Wedge type blade

A typical blade has two cutting surfaces forming an included wedge. Blades vary in size, shape and geometry. The tip geometry is defined by cutting edge parameters such as wedge angle and cutting edge radius as shown in Figure 3.4 (Reilly et al., 2004). The wedge blade used in this work was a large 2D blade with 60° wedge angle.

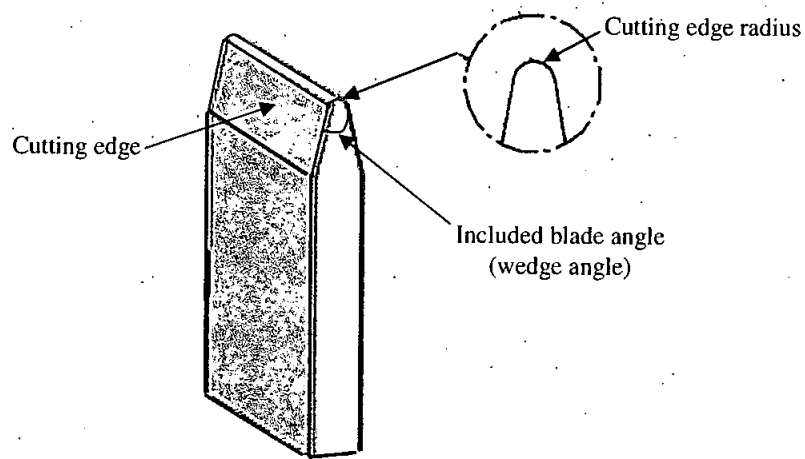


Figure 3.4: A typical wedge type blade

3.4.2 Mechanical testing machine

A material testing machine can perform different types of mechanical testing and measures related load/displacement data. An electromechanical testing machine (Hounsfield 100 HK S-series) was utilised to perform indentation cutting load. Load applied to specimen was measured with a strain-gage load cell (50kN-S-Beam) which was mounted on the underside of the moving crosshead and displacement was also measured using the crosshead travel during testing. In the strain-gage load cell, when load is applied, the strain changes the electrical resistance of the gauges in proportion to the load, and so force can be converted into a measurable electrical output. The load-displacement data was transferred from the controller component of material testing machine to a computer and displayed in conjunction with a software package (Qmat) which has 3 main parts: 1) Test generator, 2) Test zone, and 3) File examination. Test generator module allows the operator to create custom test routines for a specific experiment. In the test zone part, crosshead speed, preload, maximum applied load and displacement ranges are entered by the user for the test and then

conducted. Post-testing, the file examination module in Qmat displays the load/displacement graphs and raw data is exported to Excel.

To perform indentation loading, a test routine was set for a compression loading test. Prior to testing, parameters such as maximum load, cross-head speed rate and preload were entered as user input options by the operator. Preload is a term that is defined as pre-determined load level to ensure the indentation loading was applied by the complete contact of the blade. As shown in Figure 3.5, the wedge type blade was fixed into a designed grip mounted beneath the load cell and moved down to the cutting position with the downward progress of the crosshead.

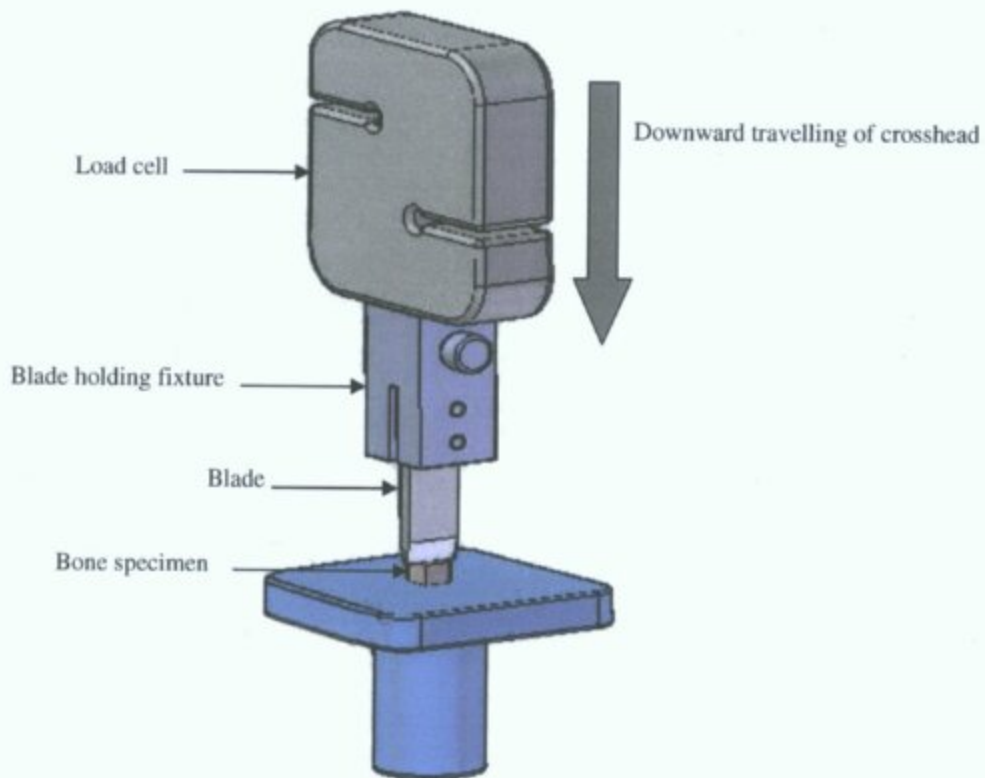


Figure 3.5: Application of indentation cutting load using MTS machine

3.4.3 Bone specimen holding fixture

In any mechanical testing procedure, it is important to hold the specimen firmly without slippage. Figure 3.6 shows the fixture used, which consists of 2 adjustment clamps to retain the bone specimen in both X and Y axis during indentation cutting. This fixture was designed by the other researchers within this group.

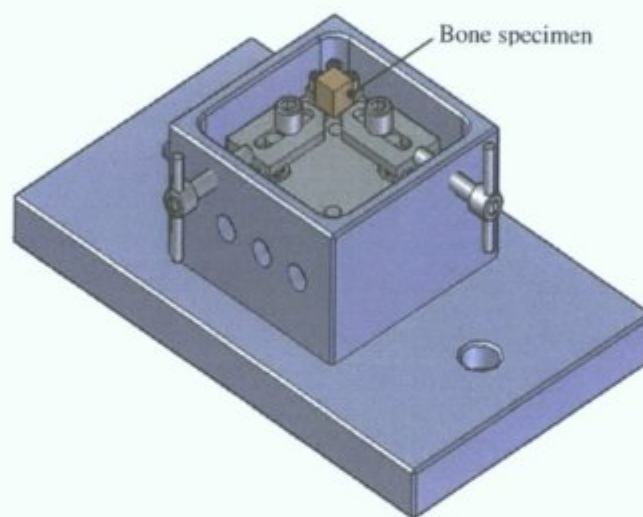


Figure 3.6: Bone specimen holding fixture

3.4.4 Acoustic emission measurement instruments

Acoustic emission system may be a single or multi-channel system. A standard AE system consists of sensor, preamplifier and AE DAQ card (or a bench multi channel system). A two channels AE system was utilised to record AE signals during indentation cutting process. This system includes:

- Miniature sensor (PICO)
- Pre-amplifier (2/4/6)
- AE DAQ card (PCI-2)
- Signal cables between preamplifier and PC
- Standard PC.

3.4.4.1 AE sensor

The AE signals are detected by an AE sensor in contact with the material under test. In an AE sensor a thin disk of piezoelectric crystal generates a voltage in response to change in material subject to mechanical stress. Figure 3.7 shows the make-up of a typical AE sensor along with its piezoelectric crystal element.

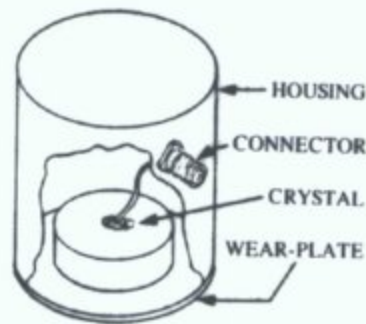


Figure 3.7: A typical AE sensor (PCI-2 based AE system user's manual, 2003)

At the time of the test, a Pico sensor (manufactured by Physical Acoustic Corporation) was the only commercially available miniature sensor (4x5mm) that was suitable for small 8mm cubic specimens in this experiment (Figure 3.8). This sensor has a single-end design to employ a single piezoelectric crystal and covers the broad frequency response of 200-750kHz which was the expected frequency range for crack-related AE signals in bone.



Figure 3.8: AE sensor placed on the bone specimen

In a typical AE test in laboratory conditions, in order to attach the sensor to the surface of the specimen during test, a number of methods may be used such as using

epoxy resin, super glue, surgical tapes or rubber bands. In this experiment, all methods were evaluated considering test conditions such as moist surface of bone and limitation in sensor attachment site and it was found that using Super Glue (cyanoacrylate adhesive) was the optimum approach. Prior to attachment of the sensor to the specimen, it is essential to fill the gap between the face of the sensor and the object surface by using an acoustic couplant such as oil, water or glycerine to achieve a high sensitivity.

3.4.4.2 Preamplifier

The AE signals detected by the sensor need to be amplified for processing procedures. The purpose of the gain is to prevent contamination of the signal by electromagnetic interference (EMI). The 2/4/6 pre-amplifier used in this work was connected to the miniature single ended sensor (Pico) preamplifier via BNC connector A (Figure 3.9). The amplifier provides the required gain and frequency filtering for the test. Three selectable gains setting of 20/40/60dB are supplied within 2/4/6 pre-amplifier (B, Figure 3.9). As seen in Table 3.1, by selecting the greater gain, a narrower frequency range can be obtained.

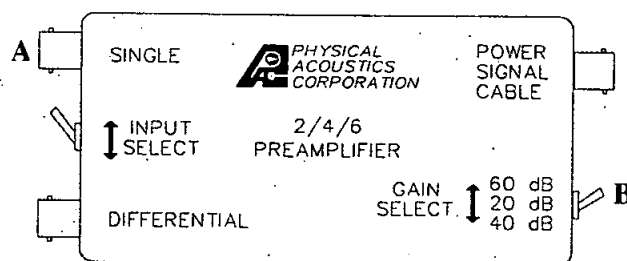


Figure 3.9: The 2/4/6 type amplifier (PCI-2 based AE system user's manual)

Gain selection (dB)	20	40	60
Bandwidth	10kHz-2.5mHz	10kHz-2mHz	10kHz-900kHz

Table 3.1: Frequency bandwidth for gains supplied in 2/4/6 amplifier

3.4.4.3 AE data acquisition card

Figure 3.10 shows a block diagram of the PCI-2 based system used in this experimental work. PCI-2 is a 2-channel data acquisition and digital signal processing card with frequency response of 3kHz-3MHz which is responded to -3dB of the input signal when a calibration signal is used. The PCI-2 DAQ card has two AE real time channels. This card is suitable for applications where low noise and low threshold is a requirement. The AE signals from the amplifier are routed to PCI-2 channel input via a standard BNC connector. After the filtering processes, this signal is passed into the FPGA DSP part of the card that converts the detected AE signals burst into AE hits and extracts different AE features such as amplitude, rise time, duration and energy.

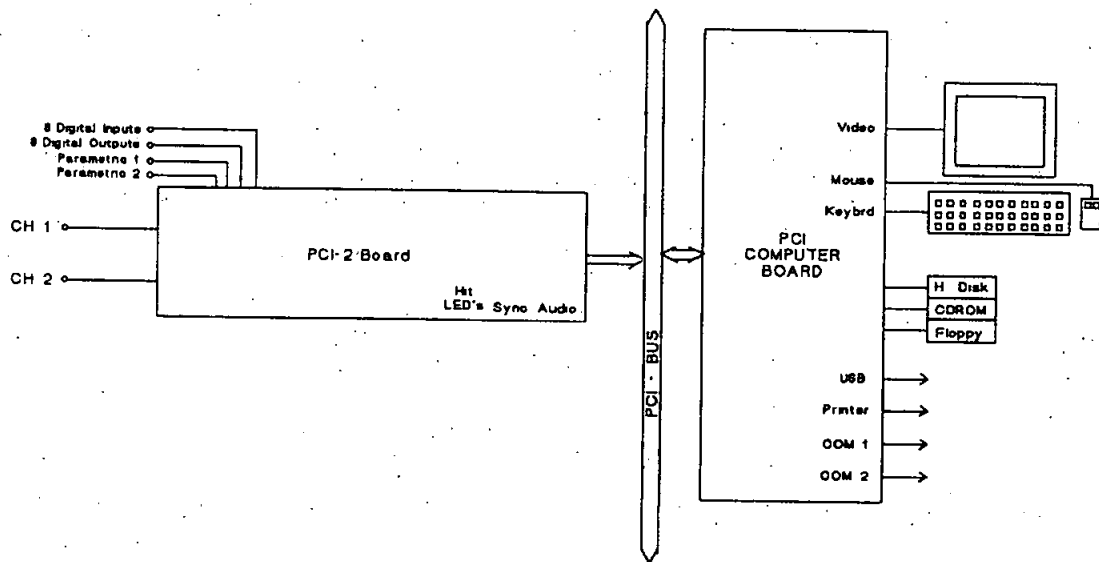


Figure 3.10: PCI-2 system connection block diagram

In addition to two AE channels, this card has a parametric connector (J6) which is located at the right side of the top of the board providing two parametric channels (Figure 3.11). The first of the two parametric inputs is a full instrumentation conditioning channel with gain control (x1, x10, x100, x1000), and filtering for transducers such as strain gauge and load cell at selectable input ranges of $\pm 10V$,

$\pm 1V$, $\pm 0.1V$ and $\pm 0.01V$. The second parametric channel is a standard single ended $\pm 10V$ Input for pre-conditioned parametric inputs.

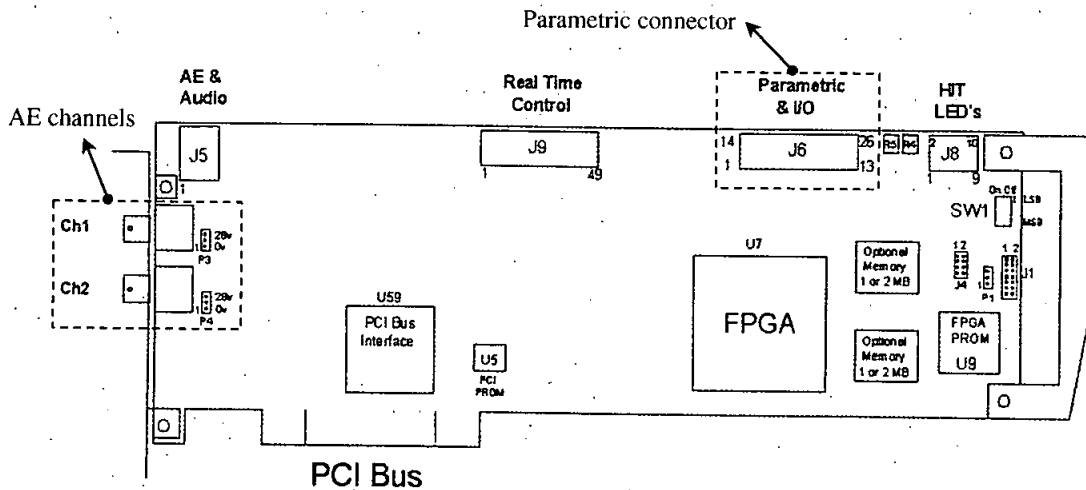


Figure 3.11: PCI-2 board layout showing key AE channels and parametric connectors (PCI-2 based AE system user's manual)

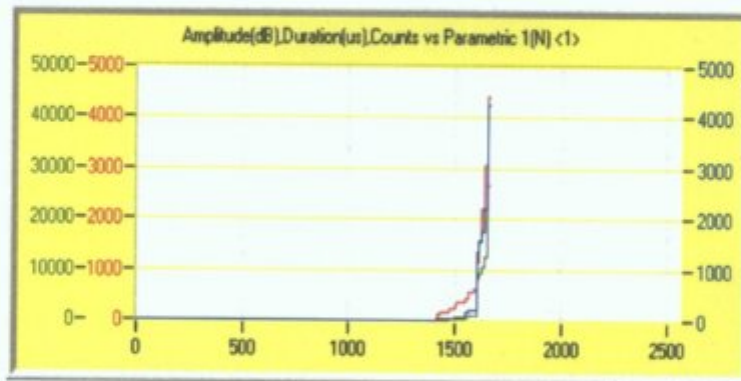
Filtering defines the frequency range for AE signals recorded in a specific AE test and usually a wideband range is set by the operator to ensure capture of all signals during testing. The frequency filtering is provided both in the preamplifier and on the PCI-2 board. In a typical AE test, frequency ranges usually do not exceed 10kHz for lower and 1mHz for upper frequency ranges. The lower frequency is limited to background noise and the upper frequency limit is governed by wave attenuation.

A wide range of frequency filtering can be set within PCI-2 including 4 high pass (3, 20, 100 and 200kHz) and 6 low pass filters (100, 200, 400, 1000, 2000 and 3000kHz).

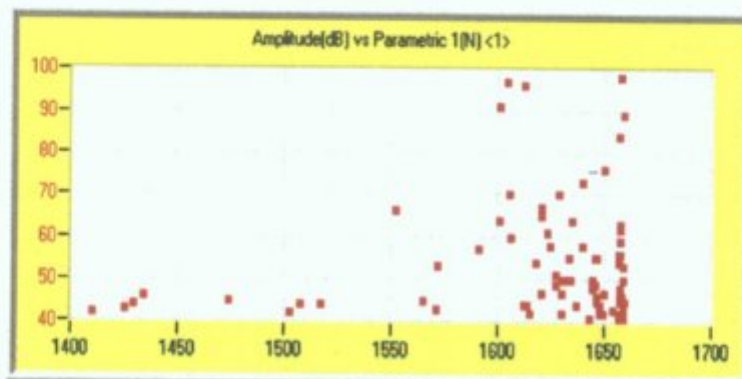
High pass filter means that AE signals pass the frequencies above the stated cut-off frequency and low pass means signals pass the frequencies below the stated cut-off frequency.

3.4.5 AEwin analysis software

AEwin 1.62 software (PAC) is a hit based feature AE data acquisition program which has acquisition and graphing utilities. Two file types are associated with AEwin: 1) Layout files which store the hardware acquisition and graph setup, and 2) Data files which contain recorded data during tests. AEwin has the post-test filtering capability to remove the unwanted AE signals below the threshold value. After testing, data files can be displayed in replay mode to analyse the recorded AE features in conjunction with load data transferred from Kistler dynamometer. Various types of graph such as 2D line and point plots (Figure 3.12a & b) were used to display the data in AEwin. The ASCII format of the data allows the user to export the data to Excel.



(a)



(b)

Figure 3.12: 2D line (a) and point (b) plots in AEwin

3.4.6 Dynamometer

Figure 3.13 shows a Kistler dynamometer (Type 9257BA) which measures the active cutting force regardless of its application point. The dynamometer has 3-component force sensors (shear-sensitive quartz plates for F_x and F_y and pressure-sensitive quartz for F_z) to measure dynamically 3 orthogonal components of force acting on the top plate. Each sensor has three pairs of quartz plates which deform under loading and measures the force or pressure, which is converted into signal output.



Figure 3.13: A Kistler dynamometer (Type 9257BA)

The integrated cable of the dynamometer is connected to the control unit (Type 5233A1) via a 19 pole MIL connector. The control unit can select the 4 measuring ranges in two groups for shear (F_x and F_y) and vertical pressure (F_z) forces. The cutting force measuring system is shown in Figure 3.14. The measured force will be converted into the voltage and displayed in the analysis software in the PC.

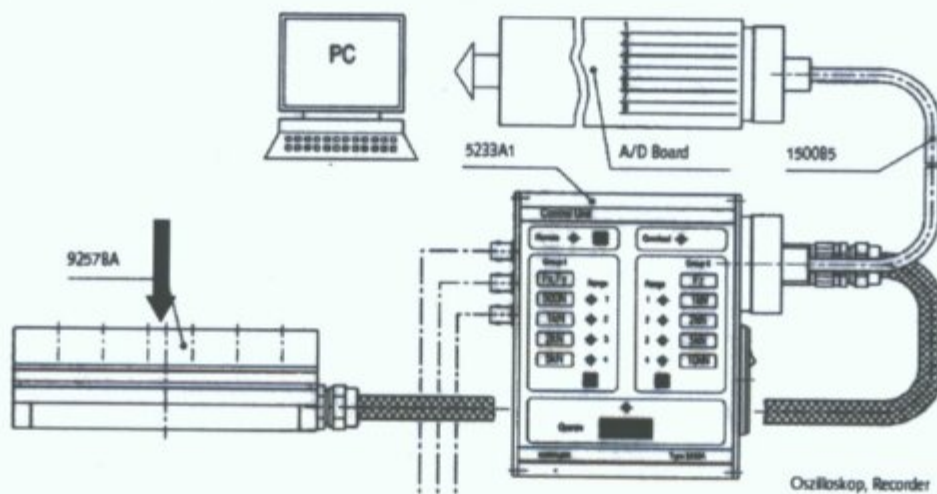


Figure 3.14: Dynamometer cutting force measuring system

3.5 Experiment model

The overview of the progression of experimental analysis for two series of experiments is shown in Figure 3.15. In experiment 1; AE signals and cutting load were monitored during loading up to final fracture, and in experiment 2, AE signals were registered at load intervals prior to complete fracture.

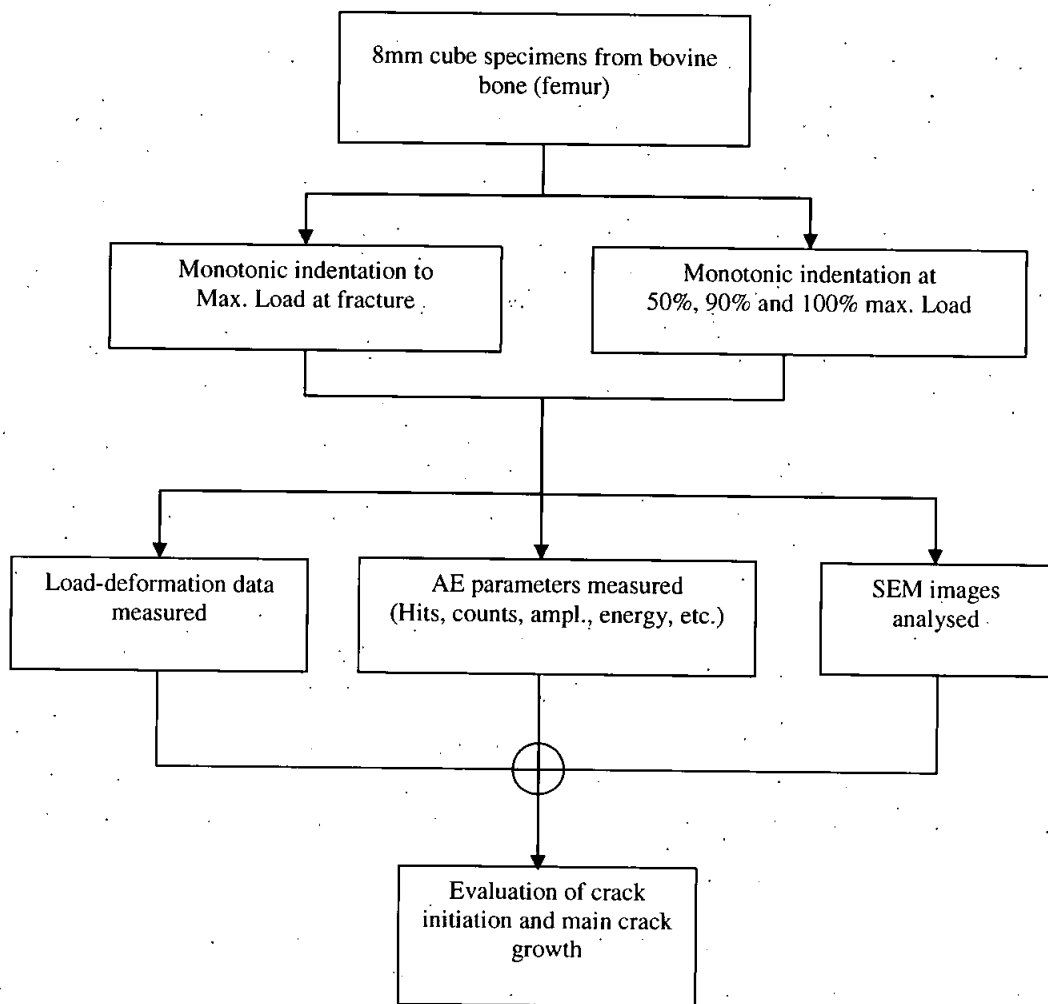


Figure 3.15: Experiment progression for experiments 1 & 2

3.5.1 Experiment 1 set up

As shown in Figure 3.16, indentation cutting load was conducted on 8mm cubic cortical bone specimens by a 2D wedge blade (60°) using Hounsfield mechanical testing machine (100 HK S-series). To perform the cutting load, a custom test routine in compression mode was set as user input options in the test generator module in the Qmat software. Prior to testing, this test routine was loaded in the test zone module and the following input values were entered by operator for the experiment:

- Crosshead speed: 2mm/min
- Preload: 200N
- Maximum load: 2000N

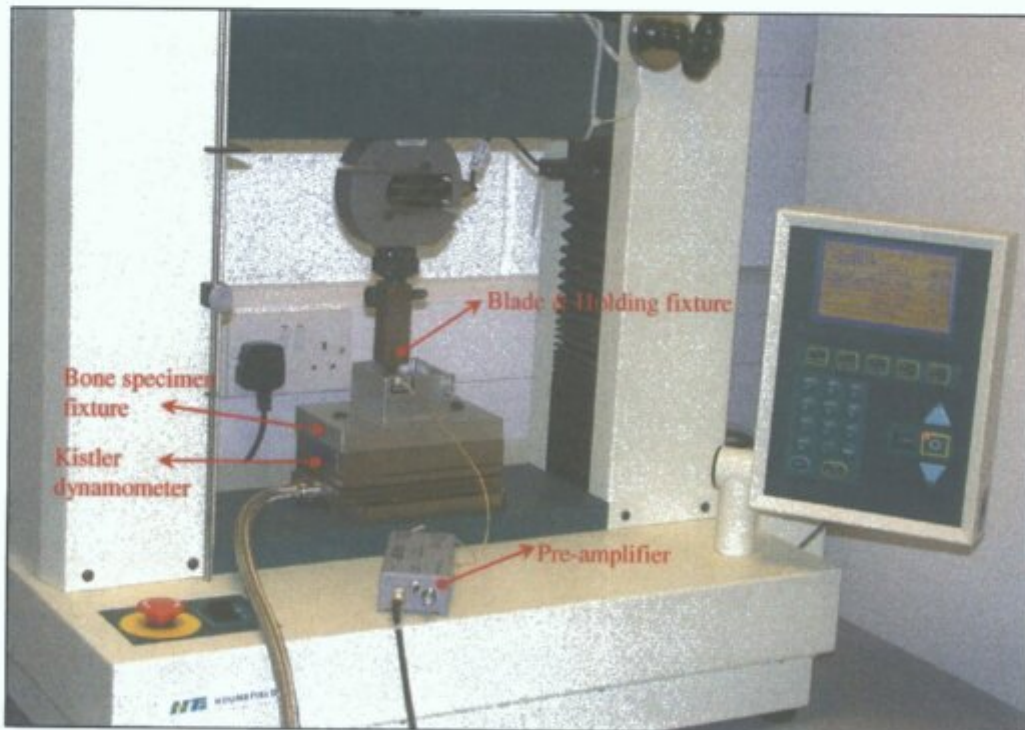


Figure 3.16: Experimental setup for monotonic indentation cutting load

Bone specimen was placed in the designed holding fixture (see Figure 3.6) and fixture was mounted on the Kistler dynamometer during indentation loading (Figure 3.17).

Mounting bone holding fixture on the dynamometer allowed direct measurement of the force in the vertical direction (F_z). Different measuring ranges depending on the expected load may be chosen in control unit for vertical force (F_z). The measuring range was set at 10KN for $\pm 5V$ scale, which means 1N equates 0.5mV.

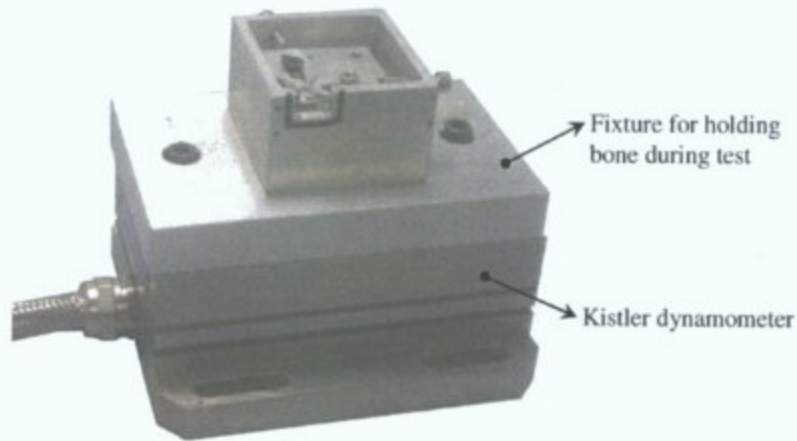


Figure 3.17: Bone-holding fixture mounted on Kistler dynamometer

AE sensor was attached at the side of the specimen (Figure 3.18) using Super Glue or cyanoacrylate adhesive (Loctite 454 Gel) and Silicone compound was used as acoustic couplant to fill interface between the bone specimen surface and the sensor for a good transmission of acoustic signals.

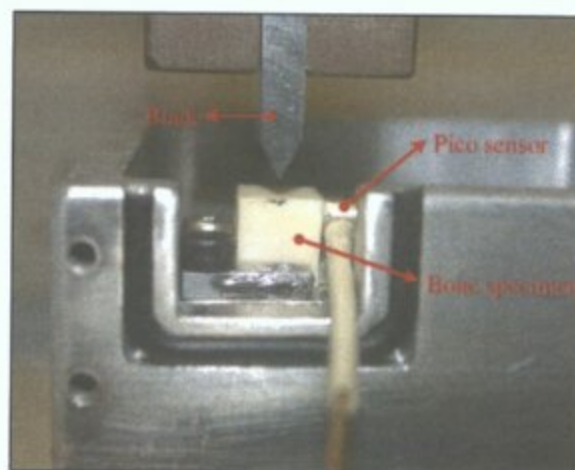


Figure 3.18: Close-up of the sensor attachment to the bone specimen

Figure 3.19 shows the position of the blade aligned to the vertical mid plane of the blade coinciding with the vertical mid plane of the cubic bone specimen.

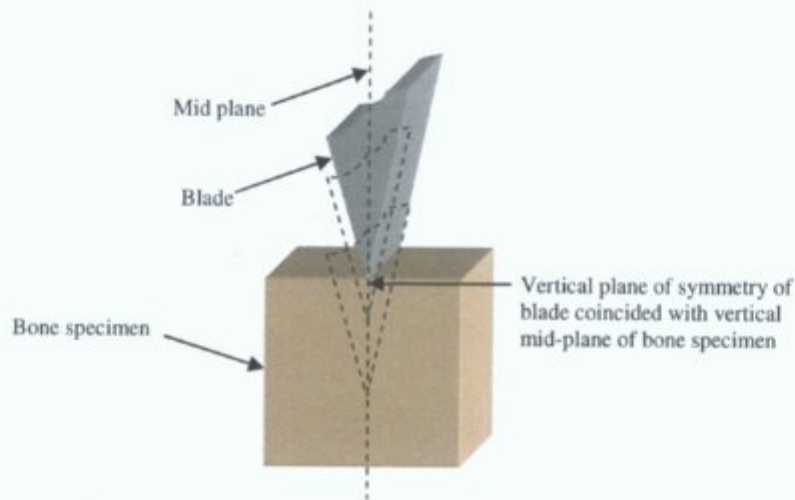


Figure 3.19: Alignment of the blade to bone specimen

During recording AE signals, cutting force was simultaneously measured and displayed (in voltage) in the AEwin analysis software. To accomplish this, the output of the measured cutting force in vertical direction (F_z) was fed into the first parametric input on the PCI-2 card as illustrated in Figure 3.20. The parametric connector on the AE card is a 26 pin IDC (Insulation Displacement Connector) connected via a ribbon cable to the rear panel of the PCI-2 based system through a DB-25 pin connector.

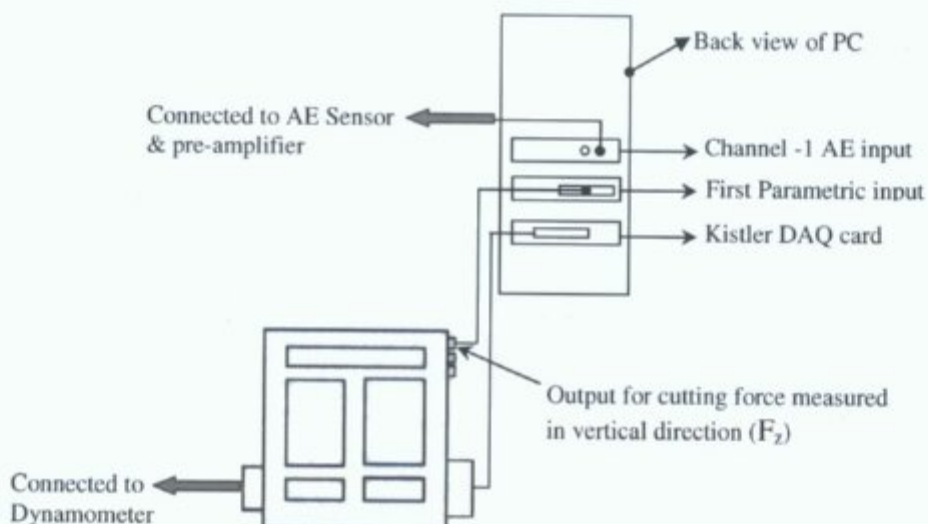


Figure 3.20: Kistler dynamometer connection to PCI-2 card

The following data sets were displayed in the AEwin and Qmat during tests:

- AE data in AEwin;
- Load/deformation data measured by Hounsfield machine in Qmat;
- Load data measured by Kistler dynamometer in AEwin.

In total, 15 specimens were cut up to final fracture in one session to avoid environment effects such as room temperature on the tests. 3 of 15 specimen tests failed during testing due to the movement of the specimens and 12 specimens were successfully tested. Bone specimens from different animals were categorised into 4 separated groups (Table 3.2).

Groups	Failed spec	Number of spec	Specimens codes
G1	-	4	G1-1/ G1-2/ G1-3/ G1-4
G2	1	3	G2-1/ G2-2/ G2-3
G3	-	3	G3-1/ G3-2/ G3-3
G4	2	2	G4-1/ G4-2

Table 3.2: Specimen groups in experiment 1

3.5.2 Experiment 2 set up

In the second series of experiments, the experimental setup was similar to the first experiment and bone specimens were tested at chosen cutting steps prior to complete fracture. For this experiment, a cross head speed of 1mm/min and load intervals of 50%, 90% of maximum load was set for each series of test. Specimens tested from the same sampling source (from one beam of bone) were categorised in one group (Table 3.3). To obtain the maximum fracture load for specimens in each group, some specimens were cut up to complete fracture. It was found difficult to cut the specimens up to 90% of maximum fracture load due to the variation in maximum

fracture load and possibility of earlier sudden fracture. In experiment 2, 15 out of 18 specimens were successfully tested.

Groups	Failed spec	50%	90%	100%	Specimens codes
G1	-	2	2	2	G1-50-1/ G1-50-2/ G1-90-1/ G1-90-2/ G1-100-1/ G1-100-2
G2	2	1	1	1	G2-50-1/ G2-90-1/ G2-100-1
G3	1	2	2	2	G3-50-1/ G3-50-2/ G3-90-1/ G3-90-2/ G3-100-1/ G3-100-2

Table 3.3: Specimen groups in experiment 2

3.5.3 AE acquisition set up

In AE testing during experiments 1 & 2, a threshold value of 40dB was set to remove mechanical and fixture noises (this will be discussed in Section 4.1) and the preamplifier was fixed at 40dB gain which provides a wide band pass filter of 10kHz-2mHz. The typical gain value of 40dB has been previously used in AE studies on cortical bone (Akkus et al., 2000) and bone cement (Jeffers et al., 2005). Therefore, AE hits with amplitude values in the range of 41-100dB were registered during cutting process. A band pass frequency filtering in the range of 100kHz-1mHz was set within the PCI-2 card under AEwin software control, however, the lower frequency range for AE signals was limited to 200kHz as the Pico sensor used in this experiment has a bandwidth of 200-750kHz.

When a gain is applied to an AE signal, the original signal is multiplied by a ratio of $V2/V1$ (using the formula of $20 \log V2/V1$). $V1$ is referenced to 1mV and $V2$ is output. The maximum output of the preamplifier is $\pm 10V$, and so the amplified signal in preamplifier can not exceed this value. This means when a 40dB gain is applied, the original signal is multiplied by 100, and the maximum signal entering the

preamplifier is restricted to $10V/100 = 0.1V = 100mV$ that equates 100dB (see Table 3.4 for amplitude range and related voltage values for a 40dB gain).

Amplitude (dB)	Signals voltage at preamp input (μV)	Signals voltage at preamp output (μV)
0	1	100
20	10	1000 (1mV)
40	100	10000
60	1000 (1mV)	100000
80	10000	1000000 (1V)
100	100000	10000000 (10V)

Table 3.4: The range of AE signal voltage amplitudes for a 40dB gain

3.6 SEM imaging

Post testing, surface damage of bone specimens was examined using Scanning Electron Microscopy (SEM). The scanning electron microscope generates a beam of electrons in a vacuum. The beam is focused by electromagnetic lenses and scanned across the surface of the sample by electromagnetic deflection coils. Interaction of primary electron beam with the material of the sample in SEM causes excitation of secondary electrons that produce flashes of light from the electrons. The light flashes are then detected and amplified by a photomultiplier tube.

Prior to SEM imaging, bone specimens were polished by hand using Buehler carbimet paper strips of various grits and then finish polished using a Buehler Motopol 2000 grinder/polisher using fine polishing cloths spread with diamond compound. Specimens then coated in gold for two minutes using EMScope (SC 500) spotter coater fitted with a gold polodium target. The bone specimen was placed into the fixture as shown in Figure 3.21 for imaging process using I-Scan image capture system (ISS group).

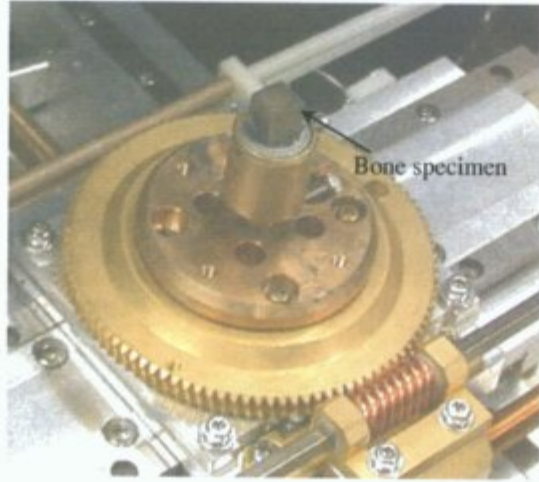


Figure 3.21: Gold coated bone specimen placed in the fixture for SEM imaging

Chapter 4: Results

4.1 Threshold set up for AE testing

Initial exploratory experiments have shown that the optimum approach to ensure maximum detection of AE signals is to set a low threshold value and apply additional post-test thresholding or windowing to remove unwanted signals.

Prior to testing, the AE sensor was attached to the bone specimen fixed in the holding rig to measure any noise generated by the fixture. AE signals were detected in the range of 35-38dB associated with the fixture noise. There was also another possible noise source which may be associated with friction between blade and the surface of the bone specimen. During testing, as soon as the blade contacts the specimen surface during the initial stage of indentation cutting, a large number of low amplitude AE hits were recorded up to 40dB. These signals which had very similar AE features (i.e. duration) were assumed to be related to friction, not caused by a single AE event from a crack. Therefore, it was concluded that AE signals above the threshold value of 40dB were generated by actual damage-related events during indentation cutting of cortical bone specimens. The threshold value of 40dB was used in previous studies of the cracking process in cortical bone (Akkus et al., 2000) and bone cement (Jeffers et al., 2005).

4.2 Results of experiment 1

In the first experiment, 12 specimens were cut up to the final fracture at a constant cross head speed rate of 2mm/min in the longitudinal plane only. Specimens from different sources (4 animals) were categorised into 4 groups (Table 3.2).

The cumulative number of AE hits and key AE signal features including amplitude, duration and absolute energy (abs-energy) were recorded during cutting process and data sets were analysed in 4 ways:

1. Cumulative number of AE hits as a function of load intervals;
2. Cluster analysis of the AE hit amplitudes to categorise AE hits into low and high amplitude signals;
3. Analysis of AE hit durations during test;
4. Analysis of the change in AE hit abs-energy as a function of load intervals.

4.2.1 Indentation fracture load

A typical graph of load versus time during the indentation cutting of bone specimens may be divided into 2 phases as shown in Figure 4.1. As can be seen in this graph, the linear region (phase I) is deviated from the non-linear region (phase II) at the yield point (marked A).

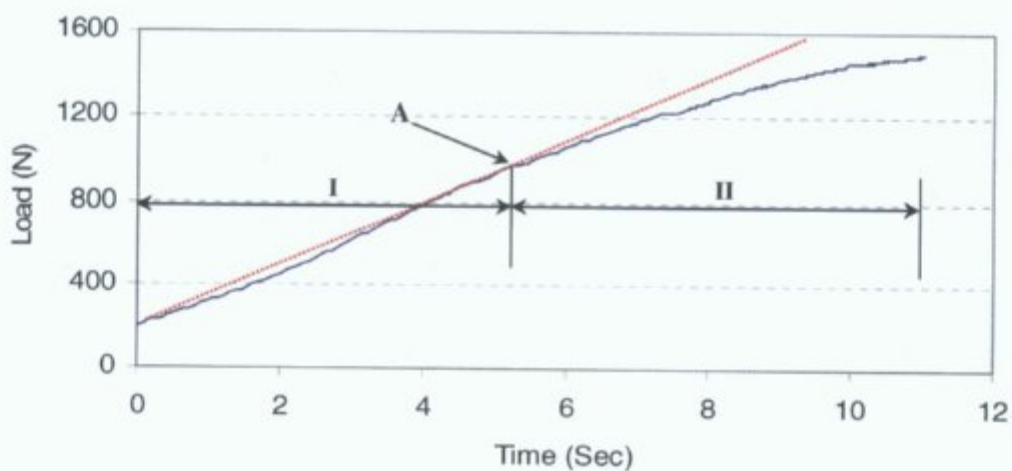


Figure 4.1: A typical graph of load versus time during longitudinal indentation cutting process

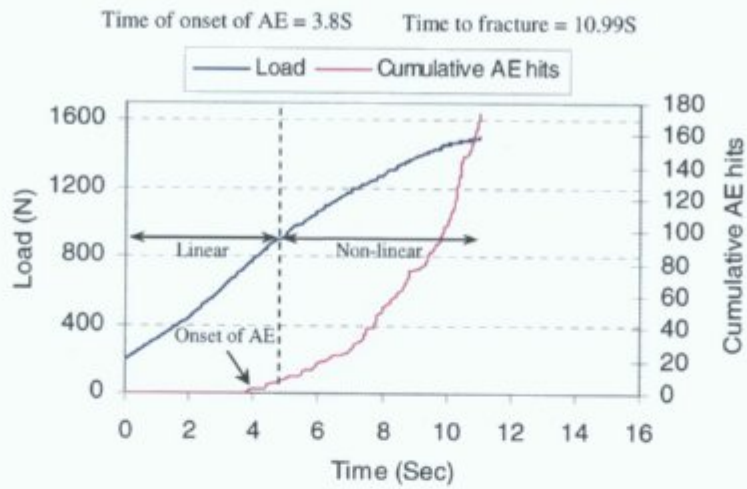
From the results, it was found that specimens fractured at a mean load value of 1633.2 ± 256.3 N which was consistent with the results of other researchers within the group (Reilly-unpublished data). The time to fracture was found to vary in the range

of 10.2-17.2S with the mean value of $13.85 \pm 2.42S$. The variation in time to fracture which was previously reported for cortical bone specimens during monotonic tensile loading (Zioupos et al., 1994) may stem from the inhomogeneous structure of bone and variation in mechanical properties.

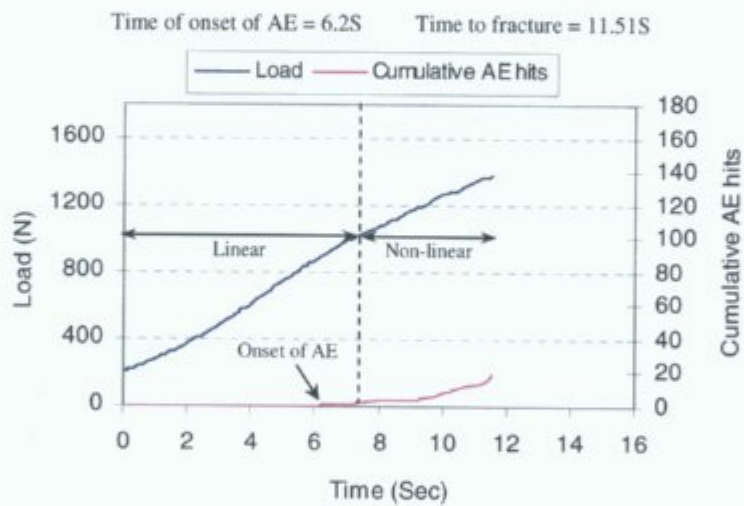
4.2.2 AE hit accumulation during the fracture process

Figures 4.2a, b, c & d show typical graphs of indentation cutting loads and cumulative AE hits against time for 4 bone specimens chosen from 4 different groups. As can be seen in these figures, the number of AE hits increased rapidly just prior to the final fracture point (see the results in Appendix A1 for all specimens). This may indicate a short pre-failure region just prior to complete fracture event which was previously reported by other researchers during fracture process in cortical bone (Currey and Brear, 1992).

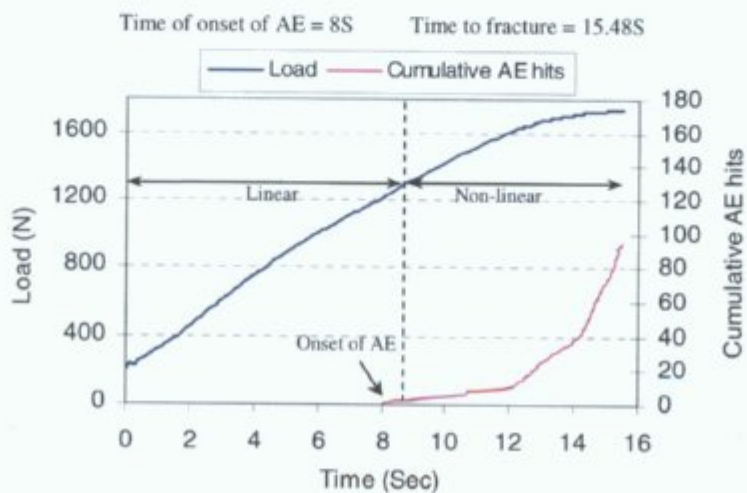
In these experiments, the variation in the recorded number of AE hits in specimens from different sources may be associated with plasticity and brittleness behaviour of the specimens during the fracture process. For example, in the specimen shown in Figure 4.2a in which a large number of AE hits was recorded during test, the load-time curve has a longer non-linear region compared to specimen shown in Figure 4.2b. The non-linear region in the load-time graph is known to be associated with a microcracking and microdamage. In specimen shown in Figure 4.2b, the brittle fracture behavior of this specimen up to the fracture point produces a lesser number of AE hits. Specimens illustrated in Figures 4.2c & d, show greater numbers of AE hits compared to the specimen shown in Figure 4.2b and this is most likely due to a longer region associated with "plastic" deformation.



(a)



(b)



(c)

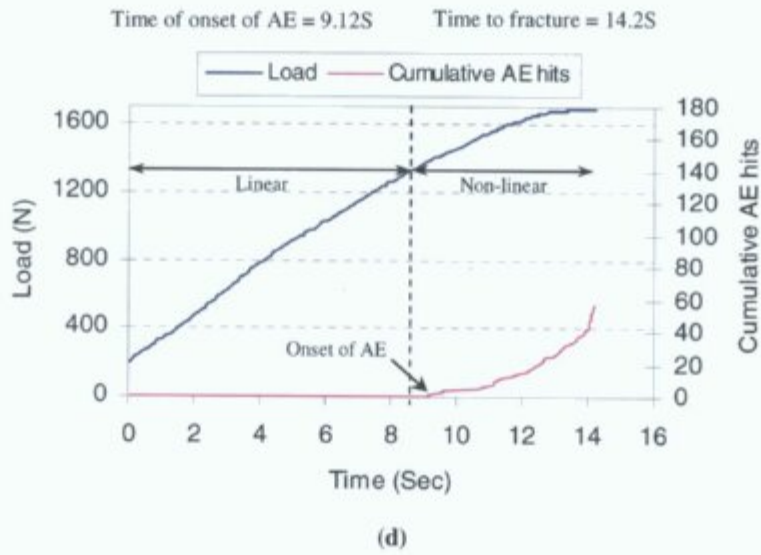


Figure 4.2: Typical plots of load & cumulative number of AE hits versus time for specimens taken from different sources

Due to the fact that the time of onset of AE activity was found to vary for specimens tested, it may be concluded that AE activity might be better analysed in a load-dependant rather than a time-dependant manner. Therefore, cumulative number of AE hits was plotted as a function of indentation cutting load to present the data for all specimens. To normalise the data, load data on the X axis is presented as a percentage of the total fracture load for each specimen (Figure 4.3).

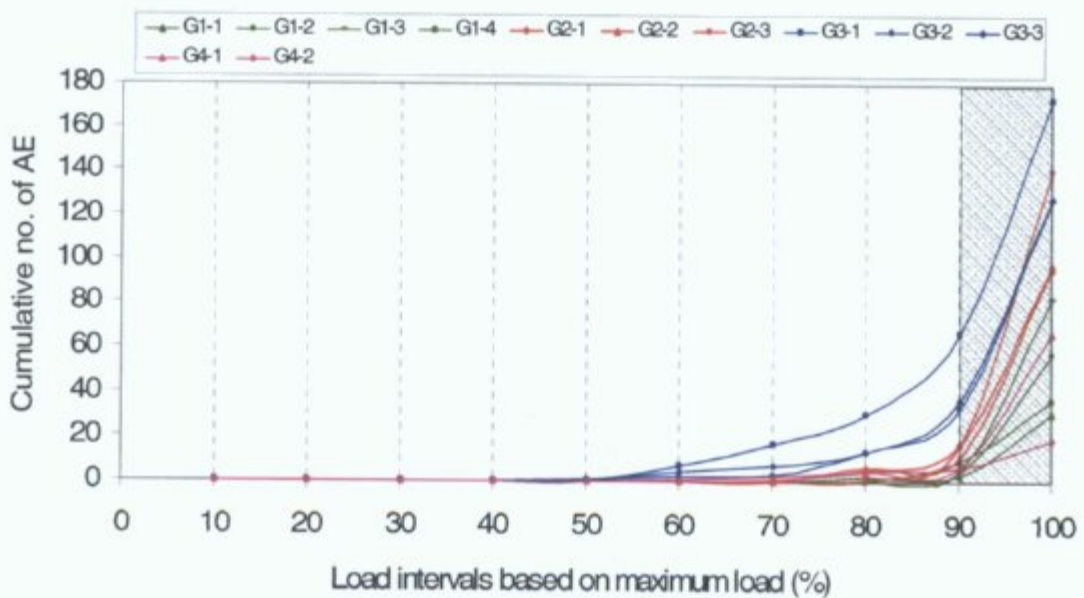


Figure 4.3: Plot of cumulative number of AE hits versus load intervals based on maximum fracture load

From this graph, it may be observed that the number of AE hits increased in a nonlinear fashion as a function of load. This graph also showed a trend for rapid increase in the cumulative number of AE hits occurring just prior to fracture during the load interval of 90% to 100% (shaded region in Figure 4.3). In a typical graph of cumulative number of AE hits as function of load, it may be possible to define three regions based on change in AE hit accumulation (Figure 4.4). As can be seen in this graph, these regions are: 1) a region up to 1383N (80% of maximum fracture load) in which no AE hits are recorded against load (I), 2) a region 1383N and 1654N (between 82% and 97% of maximum fracture load) where there is an increase in the number of hits (II), and 3) a narrow region extending from 1685N to fracture where there is a rapid increase in the number of AE hits for a relatively small increase in the load (III).

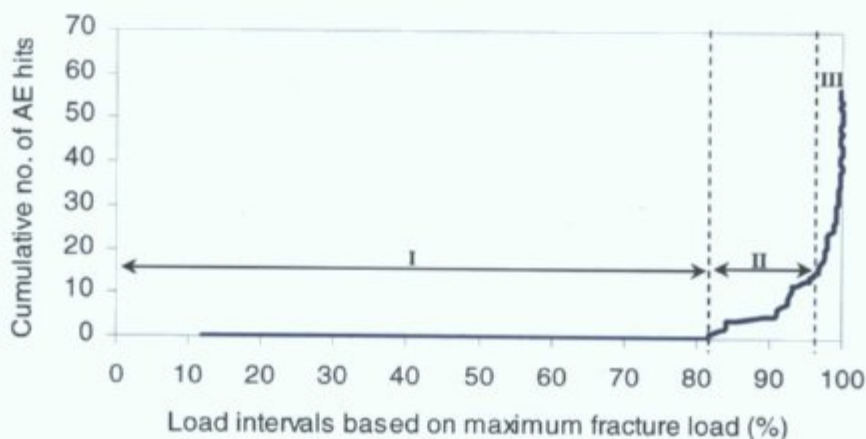


Figure 4.4: Stages of change in AE hit accumulation during the indentation cutting load

Therefore, from this type of graph, it is possible to distinguish between different phases of damage accumulation and crack growth during fracture processes. As seen in Table 4.1, the load, at which the first AE hit recorded, was found to be in the range of 46.5-84.9% of maximum load. It was also found that the significant and rapid increase in AE hit accumulation occurred just prior to fracture at the mean load value of 96.5% of maximum fracture load.

Spec	% of max. load at which 1 st AE hit observed	% of max. load at which significant change in rate of AE hits observed
G1-1	84.3	97
G1-2	81.6	97
G1-3	84.9	97
G1-4	81.7	97
G2-1	65.1	97
G2-2	70.8	98
G2-3	71.9	94
G3-1	50.4	95
G3-2	46.5	93
G3-3	58.6	96
G4-1	59.6	98
G4-2	65	99
Mean	68.3	96.5

Table 4.1: Load levels at onset of AE activity & significant change in AE hit rate during indentation cutting loading

4.2.3 Analysis of AE hit amplitudes

In order to investigate the numbers of AE hits associated with low and high amplitude signals during the indentation cutting process, AE hits within the amplitude range of 40-100dB were classified based on 10dB intervals and the numbers of AE hits in each interval were calculated as the percentage of total AE hits for each specimen tested and the data set was pooled and presented in a distribution graph (Figure 4.5).

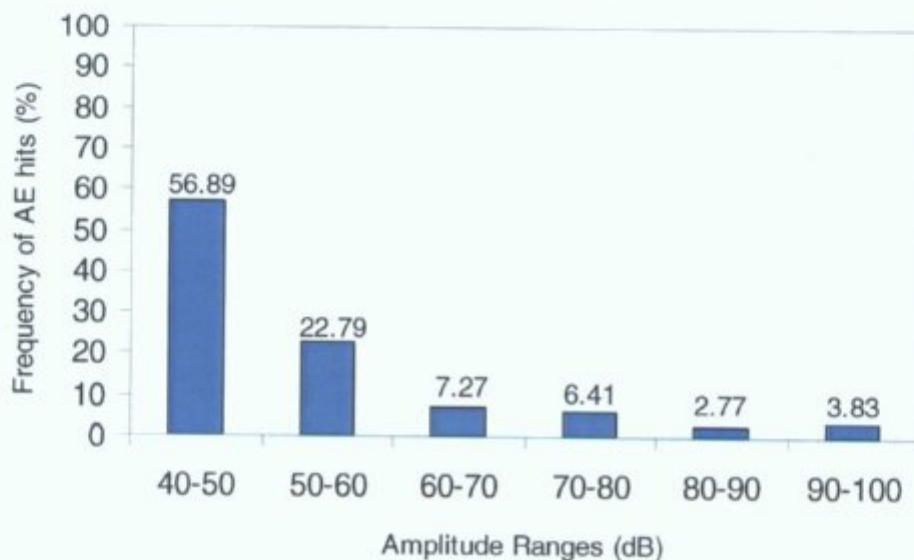


Figure 4.5: Amplitude distribution graph of AE hits recorded in all experiments

From this graph, it was found that 80% of the AE hits are in lower amplitude range of 40-60dB, while 20% of the AE hits had amplitude values higher than 60dB. It is also possible to discriminate further between the low amplitude signals as a greater number of AE hits was found in the range of 40-50dB.

In Figure 4.5, the amplitudes of AE hits were classified in 6 specified groups within the amplitude range of 40-100dB with 10dB intervals. In order to categorise AE hits into 2 groups of low and high amplitude signals, it was necessary to use a statistical clustering method which is a more primitive analysis technique and no assumptions are made concerning the number of groups or the group structure. Thus, K-mean clustering analysis was carried out using SPSS software (version 13.0) on AE hits recorded for all specimens tested and grouping was done according to similarities or distances (dissimilarities) of AE hit amplitudes based on a correlation coefficient factor (Johnson et al., 1988). AE hits were clustered into 2 groups of lower and higher amplitude signals (Table 4.2). As seen in this table, signals in group A are clustered about a mean value of 48dB in the range 41-64dB. Signals in group B are higher amplitude signals and are clustered about a mean value of 79dB in the range of 65-98dB.

Clusters	Cluster 1- Group A	Cluster 2- Group B
Number of AE hits	859	171
Amplitude range (dB)	41-64	65-98
Mean value of AE hit amplitudes (dB)	48.47	79.67
Distance of lowest amplitude to mean (dB)	7.46	15.53
Distance of highest amplitude to mean (dB)	14.67	18.32

Table 4.2: AE hits clustered into two groups based on amplitude values using K-mean clustering method

As shown in Figure 4.6, from the AE data in all experiments, a 2-parameter exponential distribution ($f(x) = \lambda e^{-\lambda(x-\theta)}$) was estimated for the number of AE hits (frequency) versus amplitude values using Maximum Likelihood (ML) statistical method (Bury, 1999).

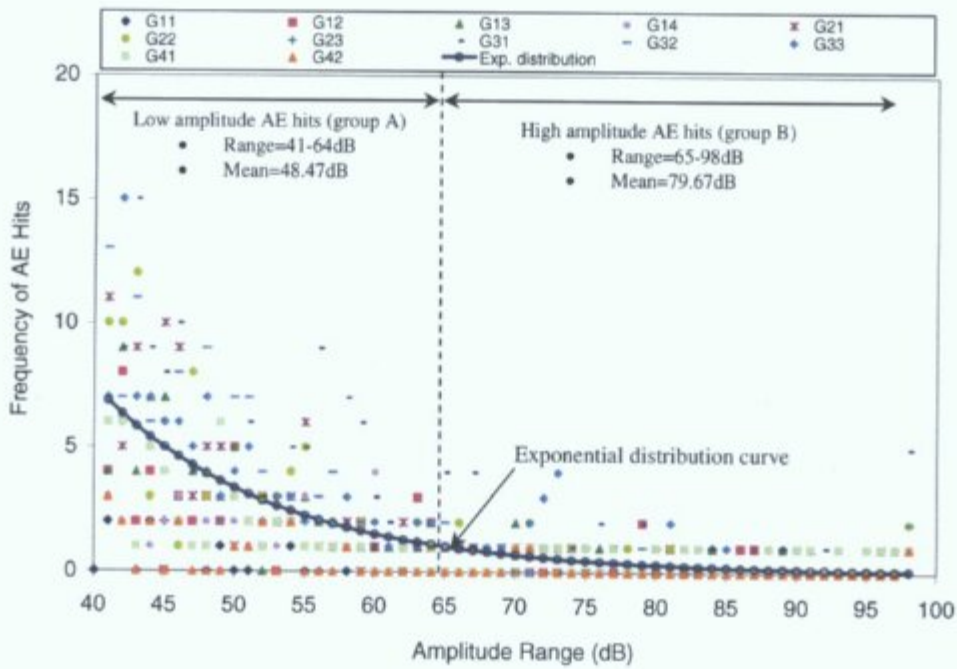


Figure 4.6: Plot of AE hit frequencies as a function of amplitude range in all experiments

4.2.4 Analysis of AE hit durations

Duration is an important AE parameter showing the length of an AE event. Figure 4.7 shows the correlation graph of amplitude and duration which plotted for a typical specimen tested. In this graph the Y axis shows duration (in μs) and the X axis presents amplitude (in dB). The graph shows that duration and amplitude values are correlated in an exponential fashion. It was found that there is only one AE hit of the highest amplitude value which is not fitted in the exponential curve due to the significant increase in duration. This AE hit had amplitude value of 98dB (marked A in Figure 4.7) and high duration value of 23676 μs compared to a similar 96dB AE hit

(marked B in Figure 4.7) which had a much lower duration of 2604 μ s. The same correlation trend was found between duration and amplitude values for the AE results of all experiments (Figure 4.8).

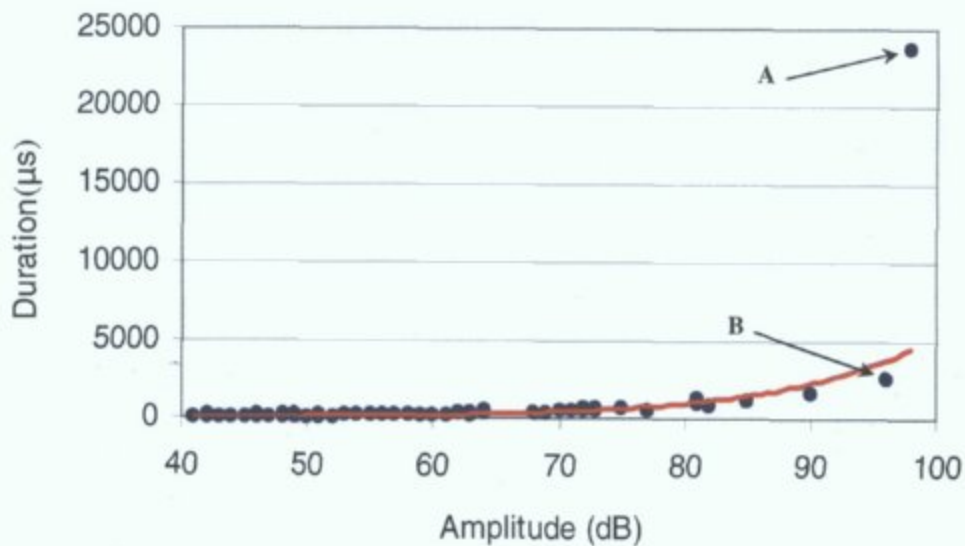


Figure 4.7: Correlation plot of amplitude versus duration for a typical specimen

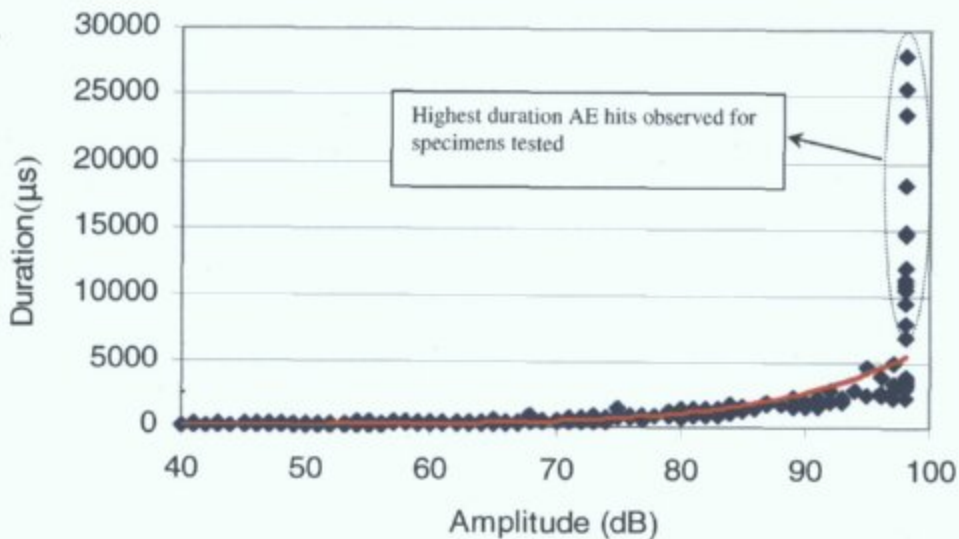


Figure 4.8: Correlation plot of amplitude versus duration for all specimens

Therefore, it was possible to distinguish one very high amplitude hit (98dB) with the highest duration value from other AE hits during the indentation cutting process in each experiment.

As shown in a typical graph of load versus duration (Figure 4.9), the AE hit which was of the highest duration (14747 μ s) occurred at maximum fracture load and it was easily identifiable on the graph from the other AE hits during fracture processes. As shown in Table 4.3, the same trend of recording the highest duration signal at maximum fracture load was observed for all specimens tested. As can be seen in this table, duration of the final fracture related signal is significantly greater than those with the second highest duration occurred during loading in each experiment.

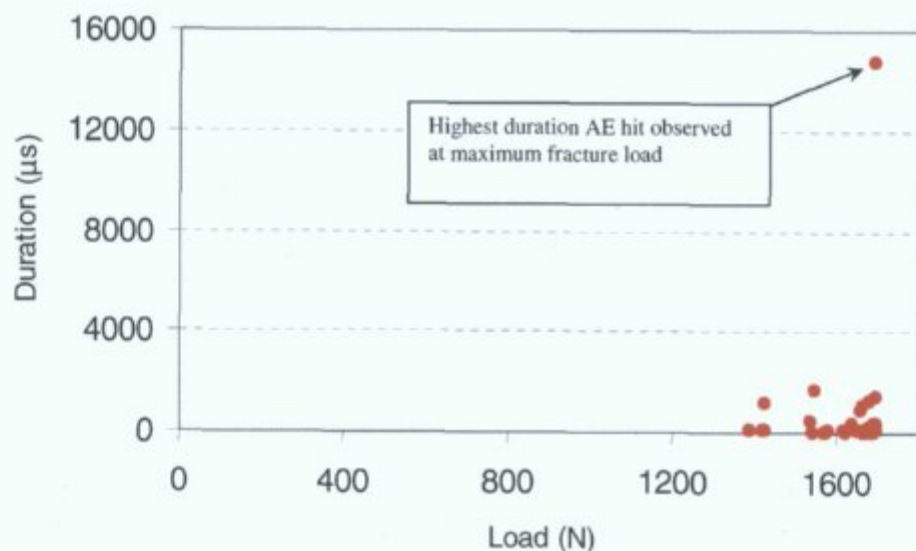


Figure 4.9: A typical graph of load & duration versus time

From the result discussed in this section, high amplitude signals which were categorised in group B (Section 4.2.3) can be further subcategorised into 2 groups based on duration values prior to and at maximum fracture load. Prior to maximum fracture load, AE signals had an amplitude range of 65-98dB and durations in the range of 175-6815 μ s (group B1) and at maximum fracture load the highest amplitude signals of 98dB with durations in the range of 7948-28059 μ s were recorded (group B2) (see Table 4.4).

Spec	Range of durations for high amplitude signals (group B) before max. load (μ s)		Duration of the signal at max. load (μ s)
	Min	Max	
G1-1	346	2742	11267
G1-2	284	1469	14767
G1-3	175	2532	9548
G1-4	321	1372	12133
G2-1	205	2474	28059
G2-2	248	3223	10626
G2-3	206	3606	25514
G3-1	207	6815	10895
G3-2	263	2261	14617
G3-3	328	2604	23676
G4-1	338	5013	18418
G4-2	548	589	7948
Mean			15625.3

Table 4.3: Durations of high amplitude AE hits prior to and at maximum fracture load

AE Features		Group B1	Group B2
Amplitude (dB)	Min	64	-
	Max	98	98
	Mean	77.37	-
Duration (μ s)	Min	175	7984
	Max	6815	28059
	Mean	1119.6	15625.3

Table 4.4: High amplitude AE hits classified into two groups based on duration values

4.2.5 Abs-energy as measure of fracture characterisation

In the subsequent AE analysis approach used in this study, absolute energy (abs-energy) was found as a good AE parameter to characterise the fracture process as it showed a good correlation with both amplitude and duration. Figure 4.10 shows

correlation graph of abs-energy and amplitude. In this graph the Y axis shows abs-energy values in logarithmic scale (in aJ) and the X axis shows amplitude values.

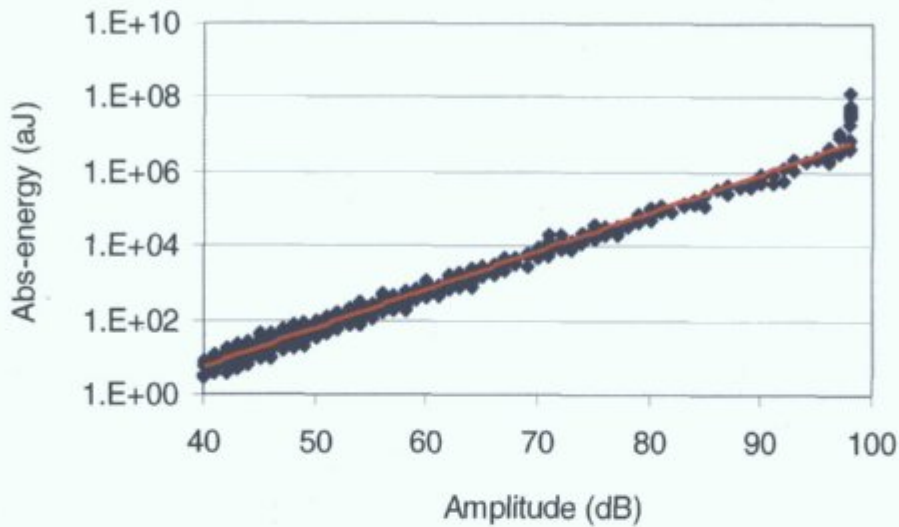


Figure 4.10: Correlation plot of abs-energy versus duration for AE hits in all experiments

From the AE results for in all experiments, it was found that abs-energy increased as a result of rise in amplitude in an exponential fashion, however, the very high energy AE hit at maximum load was not well fitted to the curve (similar to the duration & amplitude correlation graph in Figure 4.8).Figure 4.11 shows a correlation graph of abs-energy and duration. In this graph, the Y axis shows abs-energy values in logarithmic scale (in aJ) and the X axis is duration (in μs).

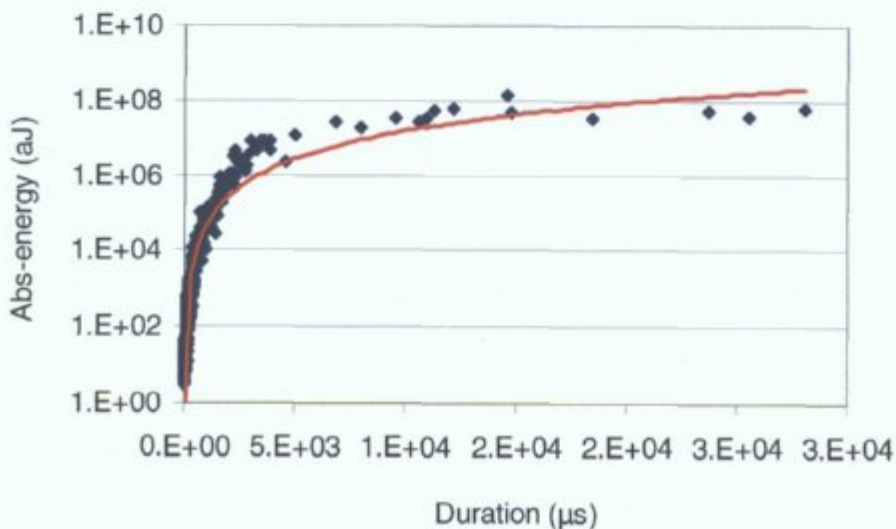


Figure 4.11: Correlation plot of abs-energy versus duration for AE hits in all experiments

4.2.6 Abs-energy from low and high amplitude hits

The sum of abs-energy values associated with the low amplitude signals (group A) and high amplitude signals (group B) was calculated for each test and presented as a percentage of total abs-energy content during the entire indentation cutting process (Table 4.5). As can be seen in the table below, although the majority of the AE events during the cutting process were of lower amplitude (see Table 4.2), these signals produced only about 0.01% (mean value) of the total abs-energy required for the fracture processes.

Spec	Sum of abs-energy (aJ) produced by lower amplitude hits (group A)	% of total abs-energy (group A)	Sum of abs-energy (aJ) produced by higher amplitude hits (group B)	% of total abs-energy (group B)
G1-1	1988.207	0.0035	56796793	99.9965
G1-2	8440.31	0.0182	46242920	99.9818
G1-3	6400.621	0.0165	38646444	99.9835
G1-4	5055.995	0.0085	58832826	99.9915
G2-1	9289.607	0.0135	68544468	99.9865
G2-2	8464.693	0.0257	32876069	99.9743
G2-3	17147.33	0.0196	87344626	99.9804
G3-1	18876.37	0.0021	89614916	99.9979
G3-2	8388.953	0.0058	142805940	99.9942
G3-3	11657.56	0.0215	54046750	99.9785
G4-1	3777.327	0.0066	56872523	99.9934
G4-2	794.281	0.0043	18434924	99.9957
Mean	6941.021	0.0122	62579910	99.9878

Table 4.5: Abs-energy produced by low and high amplitude AE hits

4.2.7 Analysis of abs-energy during the fracture process

Figure 4.12 shows plot of the mean values of abs-energy as a function of load intervals up to final fracture for all specimens. As can be seen in this graph, AE hit abs-energy did not increase in a similar fashion. In most specimens the mean value of abs-energy was found to be lower at load intervals prior to the final fracture phase between 90% and 100% of maximum fracture load. The significant increase in abs-energy content during this critical phase (shaded region in Figure 4.12) is associated with the recording of higher energy signals (AE signals which are categorised in group B with amplitude value greater than 64dB).

In some specimens (G4-1 & G4-2), a sudden rise in abs-energy was found at earlier phase of loading (80% of maximum load) followed by a decrease (up to 90%) prior to the critical fracture phase. In some other specimens (G2-3 & G3-1), a significant amount of abs-energy was produced up to 90% of maximum load which may be associated with earlier major fracture events.

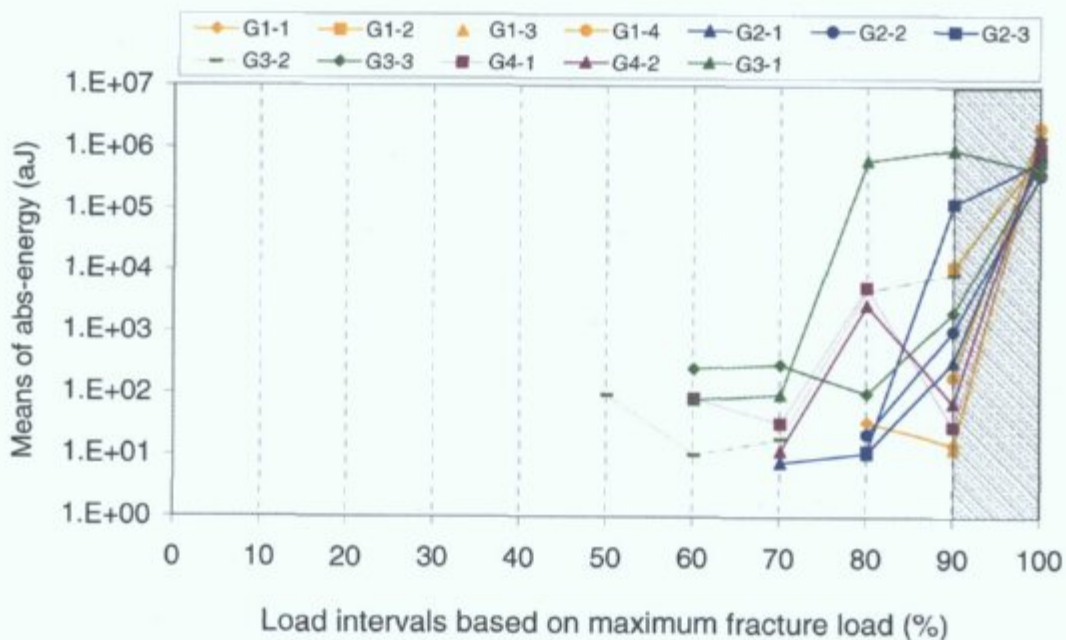


Figure 4.12: Plot of mean values of abs-energy as a function of load intervals based on maximum fracture load

As shown in a typical test in Figure 4.13, the significant increase in abs-energy during final fracture phase between 90% and 100% is mainly caused by a very high energy AE hit at maximum fracture load.

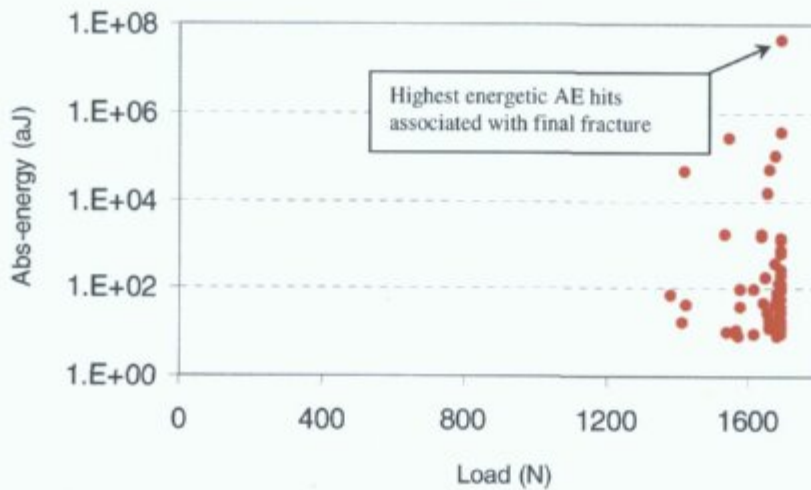


Figure 4.13: A typical graph of load & abs-energy versus time

The same trend was observed for all specimens tested (Figure 4.14). As seen in Figure 4.14, the amount of abs-energy associated with final AE hit was found to vary from specimen to specimen that may stem from the complex structure of bovine bone.

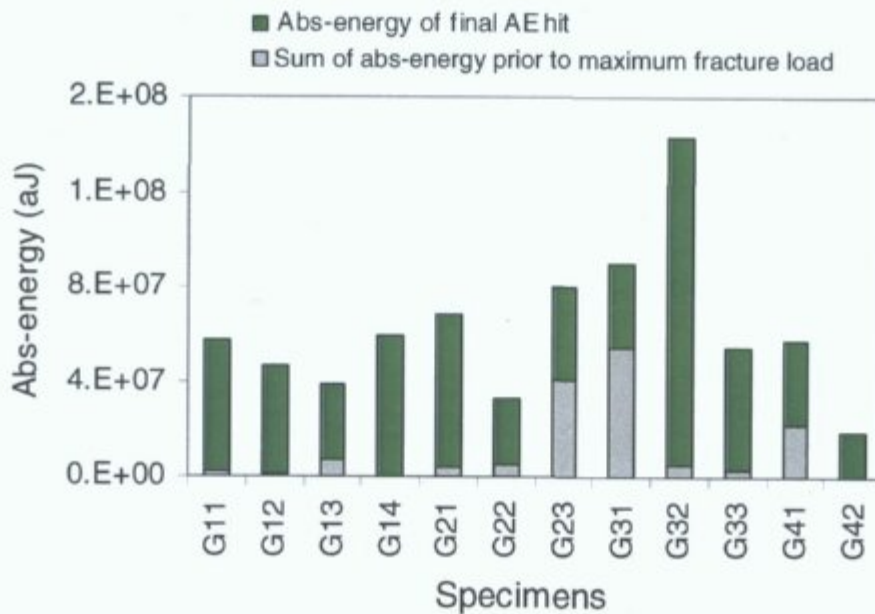
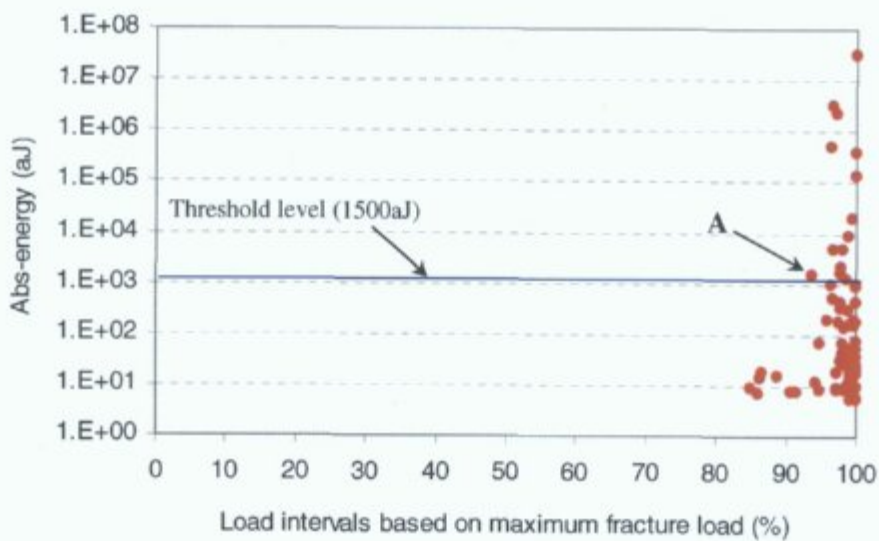
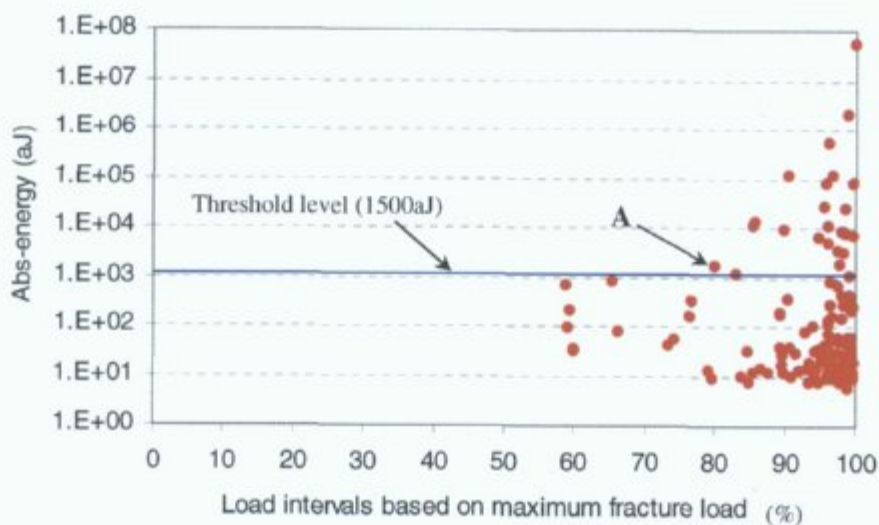


Figure 4.14: Abs-energy produced by AE hits prior to and at final maximum load

As previously discussed in Section 4.2.3, the 64dB amplitude value was calculated statistically to distinguish between low and high amplitude signals. The mean value of abs-energy for the signals which had the amplitude value of 64dB (approx. 1500aJ) was used as a threshold value to capture the first high energy signal. Figure 4.15 shows plots of AE hits abs-energies versus load intervals based on maximum fracture load (%) for two typical tests and the first high energy hit is also marked in A.



(a)



(b)

Figure 4.15: Typical graphs of abs-energy versus load intervals showing the first high amplitude AE hit: (a) First high energy signal recorded at 93% max. load and (b) First high energy signals recorded at 80% of max. load

As can be seen in Figures 4.15a & b, the first high energy signal was observed at different load levels. This analysis approach for all tests shows that the first high amplitude signal was registered at a very high mean load value of 86.9% of maximum fracture load as seen in Table 4.6, (see the typical graphs in Appendix A2).

Spec	% of max. load at which 1 st high energy AE hit observed
G1-1	96.6
G1-2	83.8
G1-3	93.5
G1-4	96.8
G2-1	90.1
G2-2	85.4
G2-3	85.7
G3-1	79.1
G3-2	77.5
G3-3	85.4
G4-1	76.7
G4-2	92.5
Mean	86.9

Table 4.6: Load levels associated with the first high energy signal

4.3 Results of experiment 2

In experiment 2, it was decided to cut the bone specimens from one animal prior to complete fracture in attempt to resolve variability observed in AE response from different animal bones observed in experiment 1. 15 bone specimens were cut at chosen load intervals of 50%, 90% and 100% of the maximum fracture load in order to investigate damage prior to complete fracture. It was also decided to reduce the cross head speed rate to 1mm/min in order to investigate the possibility of earlier AE detection that could be rate dependant.

4.3.1 Indentation fracture load

In experiment 2, the mean fracture load was 1634.73N consistent with experiment 1 results (1633.21N). The characteristics of the cutting load and AE hit response were similar to those described previously in Sections 4.2.1 & 4.2.2 (see Appendix B1 for results).

4.3.2 Number of AE hits at 50/90/100 % of fracture load

Figure 4.16 shows the recorded number of AE hits for chosen load intervals at 50/90/100% of the maximum fracture load for specimens from 3 groups (3 different bone pieces). It was found that the increase in number of AE hits follows an exponential relationship.

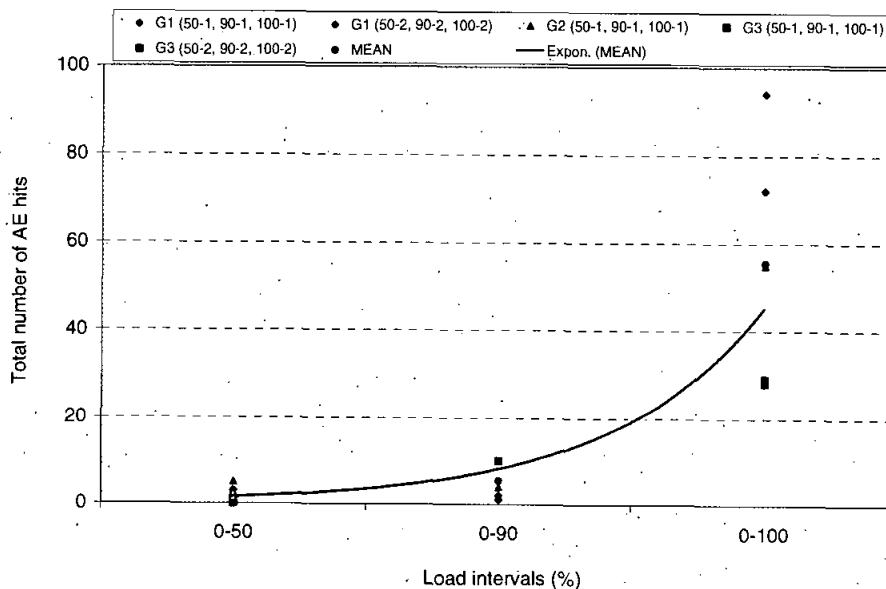


Figure 4.16: Exponential increase in the number of AE hits at chosen load intervals prior to and at final maximum load

As shown in Table 4.7, during loading up to 50% of fracture load, only 3 out of 5 specimens showed evidence of AE signals, however, during the second loading phase up to 90% of final fracture load all specimens showed AE activity. As seen in this table, there is a significant increase in the number of AE hits during the loading phase

up to 100% of maximum fracture load compared to specimens subjected to loading up to 90%.

Load intervals	Spec	Total number of AE hits
50%	G1-50-1	0
	G1-50-2	3
	G2-50-1	5
	G3-50-1	1
	G3-50-2	0
90%	G1-90-1	1
	G1-90-2	2
	G2-90-1	4
	G3-90-1	10
	G3-90-2	10
100%	G1-100-1	94
	G1-100-2	72
	G2-100-1	55
	G3-100-1	29
	G3-100-2	28

Table 4.7: Number of AE hits at 3 load intervals of 50%, 90% & 100% of maximum load

4.3.3 Quality of AE hits at 50/90/100 % of fracture load

As previously discussed in Section 4.2.5, abs-energy can be used as a method for fracture characterisation as it shows a good correlation with duration and amplitude. Figure 4.17 shows the pooled mean values of abs-energy for specimens tested at 3 chosen load intervals (50/90/100%). For the specimens cut up to the complete fracture (100%), the pooled mean abs-energy value of 652852.4aJ was found significantly greater than pooled mean values of abs-energy for specimens subjected to the indentation loading up to 90% (212.8aJ) and 50% (128.6aJ) of maximum fracture load.

As can be seen in Table 4.8, in comparison to the mean values of AE hit absolute energies, amplitudes and durations in specimens subjected to loading phases up to 90% and 100% of the maximum load, it was found that high energy AE signals (with approximate abs-energy value of over 1500aJ) were produced at the load levels

greater than 90% of maximum load (in the load range between 90% and 100% of the maximum load). This is better observed for abs-energy and duration values and may not be clearly observed for amplitude parameter as significant low amplitude signals within this critical phase reduced the mean value. During loading phases up to 50% and 90% of maximum load, no significant change was found for these values.

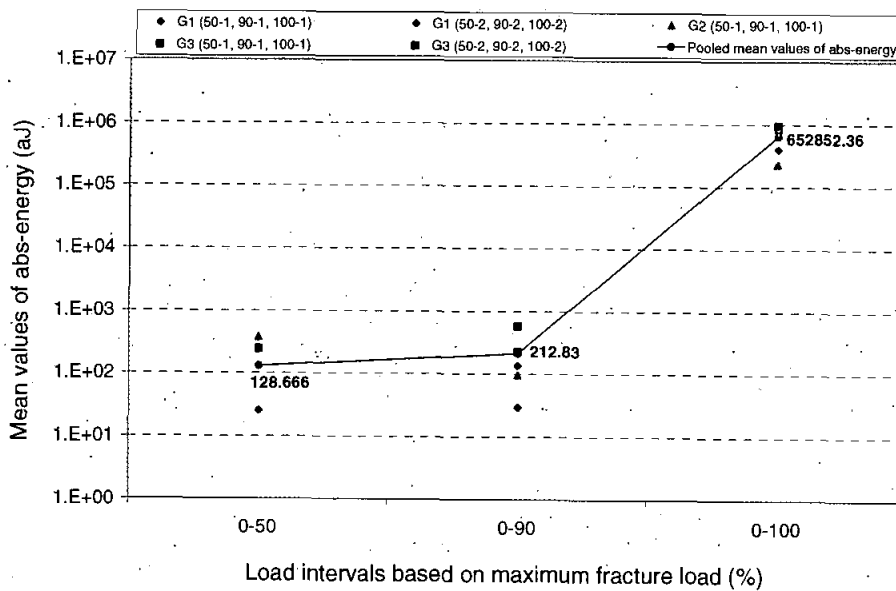


Figure 4.17: Abs-energy produced at 3 chosen load intervals prior to and at final maximum load

Load intervals	Spec	Total no. of AE hits	Amplitude (dB) (mean value)	Duration (μ s) (mean value)	Abs-energy (aJ) (mean value)
50%	G1-50-1	0	-	-	-
	G1-50-2	3	43.6	121.0	25.0
	G2-50-1	5	50.4	83.2	375.6
	G3-50-1	1	51.0	147.0	242.6
	G3-50-2	0	-	-	-
90%	G1-90-1	1	52.0	165.0	135.6
	G1-90-2	2	46.5	34.5	28.7
	G2-90-1	4	50.5	133.5	96.1
	G3-90-1	10	44.6	117.2	224.7
	G3-90-2	10	49.8	149.7	578.9
100%	G1-100-1	94	52.1	290.3	781208.7
	G1-100-2	72	53.6	200.9	400829.0
	G2-100-1	55	54.7	274.9	232207.7
	G3-100-1	29	54.8	483.3	888488.2
	G3-100-2	28	52.7	469.4	961528.2

Table 4.8: Mean values of AE hit features at 3 load intervals of 50%, 90% & 100% of maximum load

The significant increase in abs-energy for specimens subjected to loading up to 100% of maximum cutting load is mainly caused by the highest energy signal occurring at the peak load (see the results in Appendix B2). As can be seen in Table 4.9, these signals had a mean amplitude value of 98dB, mean duration value of 4583.4 μ s, and mean abs-energy value of 23569200aJ.

Spec	Amplitude (dB)	Abs-energy (aJ)	Duration (μ s)
G1-100-1	98	29589000	6420
G1-100-2	98	28060000	5858
G2-100-1	98	12389000	1245
G3-100-1	98	23251000	2300
G3-100-2	98	24557000	7094
Mean	98	23569200	4583.4

Table 4.9: AE hit features at maximum fracture load

4.3.4 SEM images analysis

SEM images were captured in order to assist in analysis of the AE results at 3 chosen load intervals of 50%/90%/100%. SEM images of three specimens from the same piece of bone were captured as it was expected that these bone specimens would behave in similar manner under indentation loading.

Figure 4.18 shows a typical SEM image of the specimen cut up to 50% of maximum load. As can be seen in this figure, there is some evidence of initial damage at the cutting zone underneath the blade tip which is attributed to a small surface crack and associated with uncracked ligament bridging (terracing effects) as recently reported as a major damage mechanism in bone (Nalla et al., 2004; 2005; Hazenberg et al., 2006).

As shown in Figure 4.19, very few AE hits were recorded in this specimen.

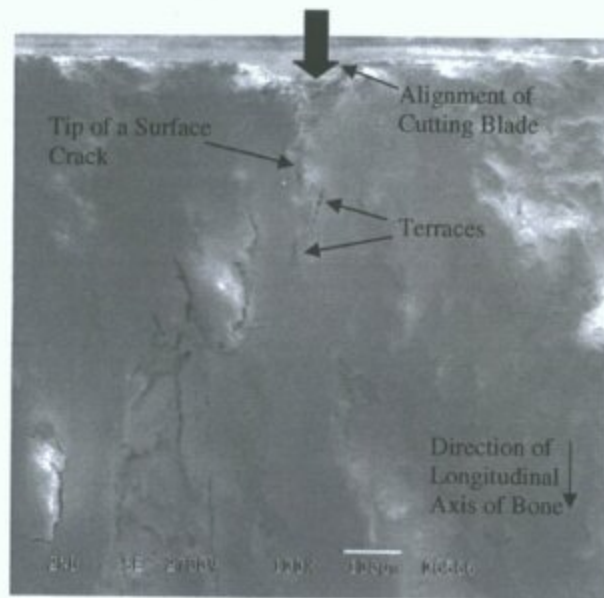


Figure 4.18: SEM image of bone specimen cut up to 50% of maximum load

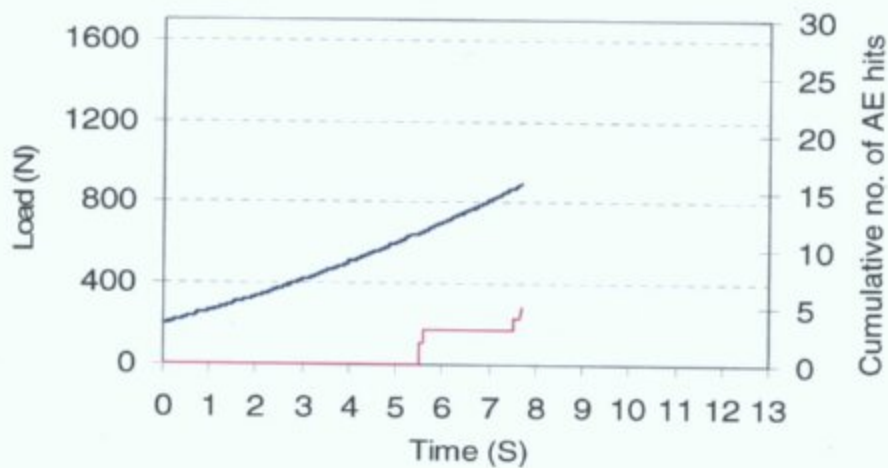


Figure 4.19: Cumulative number of AE hits of bone specimen cut up to 50% of maximum load

Figure 4.20 shows an SEM image of the specimen cut up to 90% of maximum load before final complete fracture. This figure shows early stage of a fracture crack formation as a result of increase in indentation load. This specimen may show some evidence of fibre bridging as a toughening mechanism in cortical bone. As illustrated in Figure 4.20, this specimen showed more AE activity during second phase of cutting (Figure 4.21) compared to the specimen cut up to 50%.

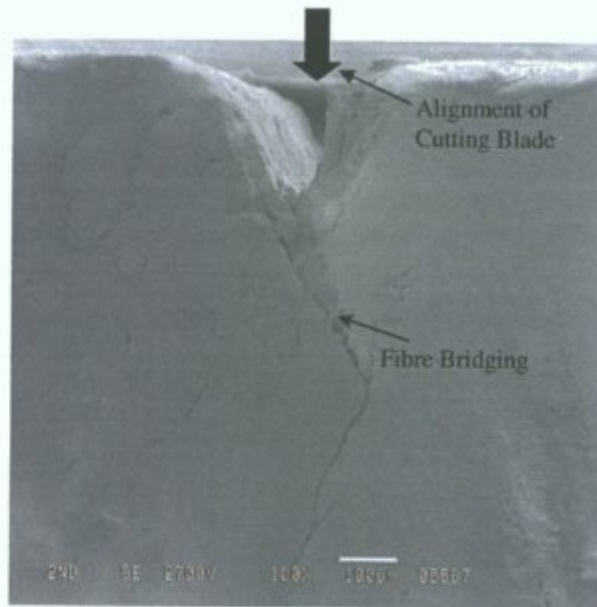


Figure 4.20: SEM image of bone specimen cut up to 90% of maximum load

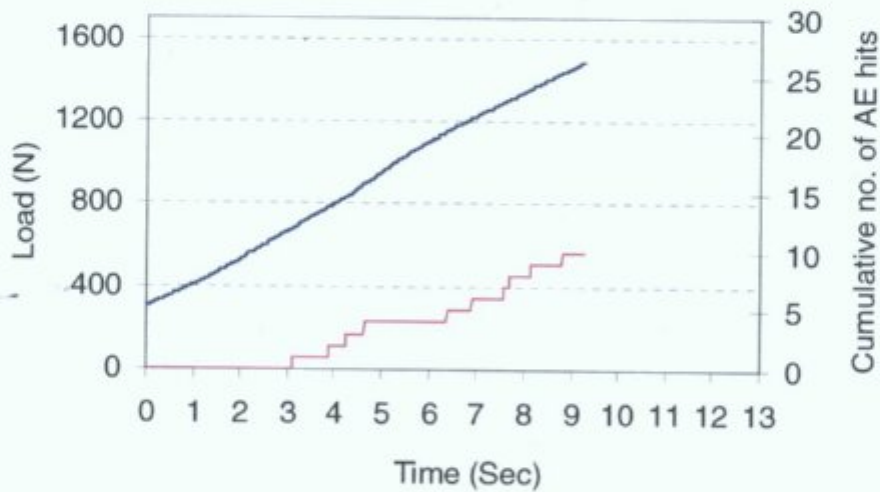


Figure 4.21: Cumulative number of AE hits for bone specimen cut up to 90% of maximum load

Figure 4.22 shows a specimen which fractured completely (separation) as the blade was further penetrated into the bone leading to a rapid increase in the number of AE hits (Figure 4.23).

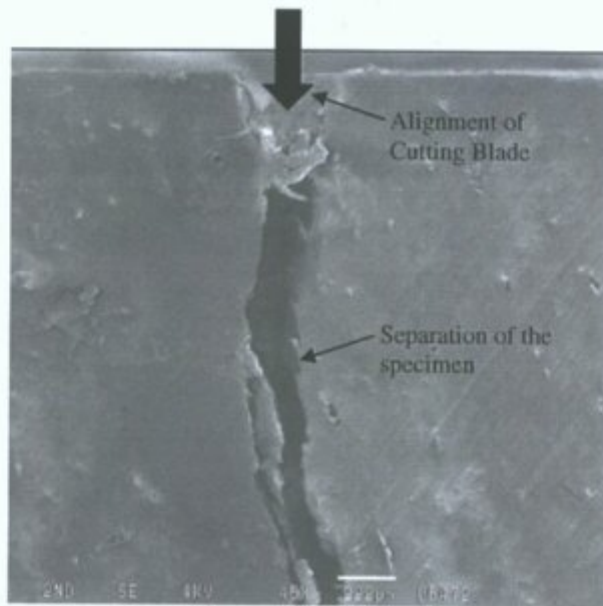


Figure 4.22: SEM image of bone specimen cut up to maximum fracture load

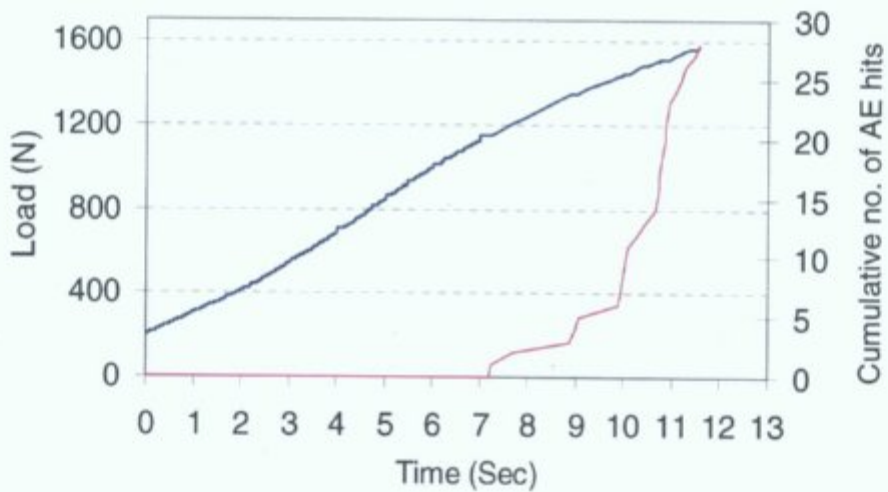


Figure 4.23: Cumulative number of AE hits for bone specimen cut up to maximum fracture load

In summary, analysis of SEM images in conjunction with AE results showed that the number of AE signals increased as a result of advance of the main fracture crack up to separation of the specimen.

Chapter 5: Discussion

5.1 Overview

The application of the acoustic emission technique to monitor crack growth during monotonic indentation cutting on cortical bone specimens is a new area of research. In this study attempts were made to analyse different parameters of AE signals based on techniques used by others. As found in the AE studies on bone and other materials, AE testing was typically carried out on the notched specimens subjected to fatigue loading as it was easier to detect crack initiation and monitor propagation phases. Few attempts were made to apply the AE technique to specimens under monotonic loading.

In this study, the AE analysis approach was carried out as follows:

- To introduce absolute energy as a good parameter to quantify an AE signal characteristics as it was strongly correlated with both amplitude and duration;
- To separate the signals into low and high amplitude signals;
- To record the first high energy signal as an indication of main crack initiation;
- To identify a significant change in AE hit accumulation after recording the first high energy signal to identify unsteady crack propagation phase;
- To register the highest energy signal indicating the final fracture event.

Prior to discussion of the results, it should be noted that the variation in AE results to identify crack initiation and propagation may stem from the complex nature of bovine and further study is required to determine the microstructure at the surface of bone to characterise the crack initiation as well as understanding the effects of inner sites microstructure on main crack propagation process.

5.2 Discussion of results in experiment 1

5.2.1 Fracture process monitoring based on AE hit accumulation

In AE studies, a plot of AE hits versus loading time or load (History plot) is the most commonly used method to show a trend of AE activity. From the results, a nonlinear increase may be found in AE hit accumulation during cutting process up to final fracture which was consistent with previous studies on bone and associated with damage accumulation in the form of microcracking and crack growth (Netz et al., 1980; Wright et al., 1981; Jonsson et al., 1984; Fischer et al., 1986; Zioupos et al., 1994). The results showed that there is a rapid increase in the cumulative number of AE hits occurring just prior to fracture during the load intervals of 90% to 100% (Figure 4.3) which indicates an increase in the number of fracture events occurring during final crack propagation phase (Akkus et al., 2000). It is assumed that the increase in number of AE hits at this critical stage is related to an increase in, and a mixture of microcrack and crack growth events as previously proposed Vashishth et al. (1997; 2000).

It was observed that the recorded number of AE signals was found to vary in specimens tested (see Figure 4.2) and this may stem from a number of factors such as variation in density (Hanagud and Clinton, 1975), variation in brittleness and plasticity in different parts of bone (Hanagud et al., 1977), and pre-existing defects (Thomas et al., 1977). It is important to note that the bovine bone specimens used in these experiments have a mixture of highly mineralised (woven) and less mineralised lamellar bone (Figure 2.8), and due to the fact that specimens were taken from a number of sources (different animals), it was expected that there would be variation in the AE response for specimens tested.

An AE model of crack propagation phases has previously been described by Kohn et al. (1992a; 1992b) based on change in the amount and rate of AE hit accumulation for titanium alloy material (Ti-6Al-4V) during fatigue tensile tests (Figure 5.1) as follows: (a) early AE, indicative of fatigue damage initiation (I), (b) lower AE rate, indicative of steady crack propagation phase (II), and (c) an increase in the amount and rate of AE, indicative of unsteady crack propagation and final fracture (III). As illustrated in Figure 5.2, during the indentation cutting process on bone specimens in this research, the change in cumulative AE hits indicates a similar trend to Kohn's model for a typical specimen.

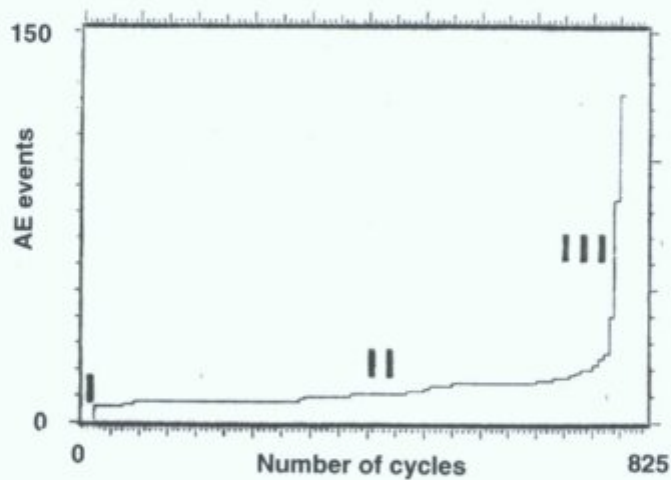


Figure 5.1: Stages of crack growth up to final fracture during fatigue tensile loading of titanium alloy proposed by Kohn et al., (1992)

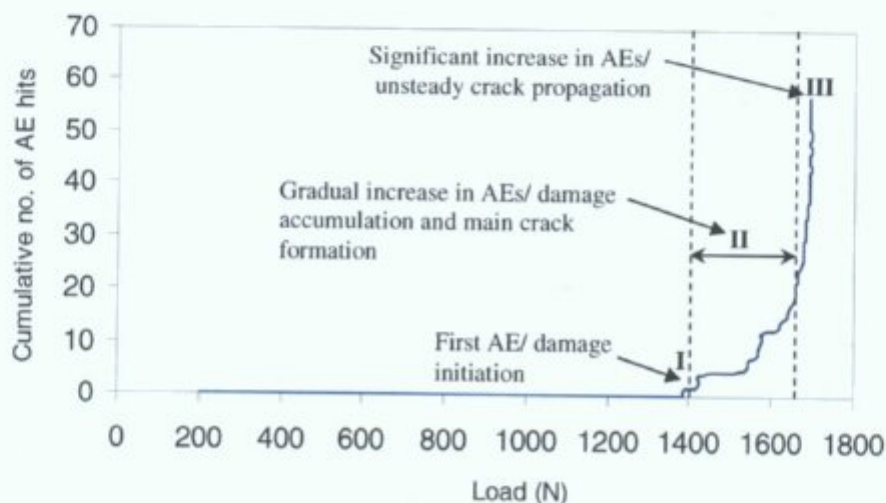


Figure 5.2: Stages of crack growth based on change in AE hit accumulation during indentation loading

It should be noted that in the crack growth process described by Kohn et al. (1992a; 1992b), the crack was initiated from a notch in titanium alloy (a ductile material) subjected to fatigue loading, and so a main crack would propagate more slowly in a step by step manner up to fracture and the associated damage accumulation phases could differ from bone damage process (a semi brittle material) subjected to a monotonic indentation load that could result in a faster crack initiation and propagation. Therefore, it was necessary to investigate the intensity of the signals in order to describe the onset of damage and main crack initiation in regions I & II for bone. It is assumed that the significant change in AE hit rate just prior to fracture point for specimens about a mean value of 96.5% of maximum fracture load (see Table 4.1) may indicate a critical phase of unsteady crack propagation.

5.2.2 Failure modes detection based on amplitude and duration

In order to identify high energy signals related to cracks (initiation or propagation) during loading and to separate them from weaker AE hits associated with microcracking, a statistical clustering method was carried out on AE hit amplitudes. By using the K-mean clustering method, a threshold value of 64dB was calculated to separate the signals into the low and high amplitude signals (see Table 4.2). It was assumed that a greater number of low amplitude signals in the range 41-64dB (group A) may be associated with microcracking, whereas, a lower number of high amplitude signals in the range of 65-98dB (group B) may correspond to main crack initiation and propagation events similar to previous AE studies on bone which showed crack growth-related signals produce AE signals with amplitude values above the 65dB (Yoon et al., 1980) or 70dB (Akkus et al., 2000). It was also reported that fracture related signals in composite and titanium alloy materials generate the amplitude value above the 70dB (Bakusken and Awerbuch, 1987; Kohn 1992a; 1992b).

During the fracture processes, greater numbers of microcrack related signals than those related to crack growth events were previously observed by Akkus et al. (2000). SEM studies of surface crack growth (Vashishth et al., 1997) and histological observations of damage process at inner sites (O'Brien et al., 2005) in bovine bone confirmed that microcracks were dominant damage type during crack growth processes.

It may be also possible to discriminate further between these low amplitude signals. It was reported by researchers that more AE hits in the lower amplitude range were associated with diffuse damage (Akkus et al., 2000). Therefore, it was hypothesised that the greater number of AE hits observed in the range of 40-50dB may be associated with diffuse damage. This was agreed by other researchers within this group for a similar experimental setup that diffuse damage is the dominant damage type using histological methods (Reilly et al., 2005a; 2005b).

The limitation of the use of amplitude parameter to identify crack growth phases is that the final complete fracture event showed amplitude value of 98dB similar to some signals associated with crack propagation events prior to final fracture in the range of 65-98dB. Therefore, one can not only rely on amplitude values and it is necessary to analyse durations of these high amplitude signals. Analysis of the durations showed that the highest duration signals at maximum load with a mean value of 15625.3 μ s in the range of 7984-28059 μ s are related to the final fracture events (group B2), however, other crack propagation signals had lesser durations in the range of 175-6815 μ s (group B1) (see Table 4.3). Observation of the highest duration signal at maximum failure load was previously confirmed by Jeffers et al. (2005) in bone cement subjected to fatigue loading (approx. 4000 μ s duration value for signal at maximum failure load) (Figure 5.3). Therefore, by analysing the duration

values, final fracture related AE hits were separated out from other crack growth and/or simultaneous crack propagations at multiple, unknown sites which could not lead to the complete fracture events.

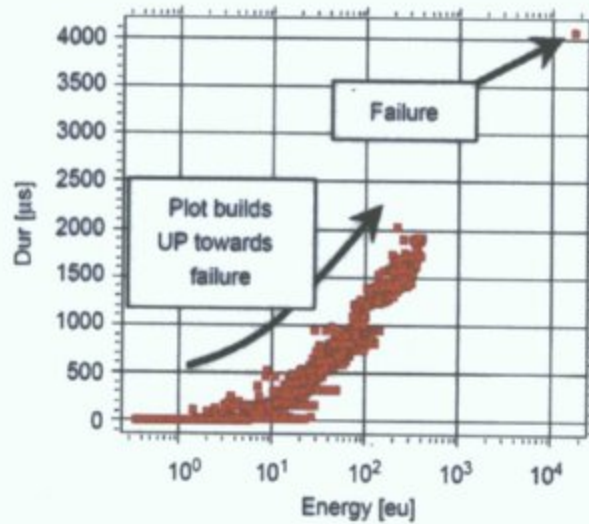


Figure 5.3: Observation of the signal with the highest duration value at final failure for bone cement specimen under fatigue loading (Jeffers et al., 2005)

5.2.3 Monitoring of fracture process based on abs-energy

Abs-energy was found to be a good parameter for fracture characterisation (discussed in Section 4.2.5). It has been widely accepted that total energy required during the fracture process is the sum of energy generated by microcracking and main crack growth events. In this study, it was shown that abs-energy produced by a large number of low amplitude signals associated with microcracking is negligible compared to abs-energy produced by crack propagation events during fracture (Table 4.5). Lower mean values of abs-energy were usually observed at initial load intervals in most specimens which are associated with weaker AE events and may be generated by initial microcracking at an early stage of the indentation cutting process. This is followed by a significant increase in abs-energy up to the final fracture point during 90-100% of maximum load (see Figure 4.12), however, this graph would not be very

useful to further investigate in the details of crack growth processes. Therefore, the change in AE abs-energy during the indentation loading up to final fracture was analysed for each specimen (see Figure 4.15 for a typical specimen) to identify the first high energy hit with abs-energy value over of 1500aJ. This abs-energy value is the mean value for abs-energy of the AE hits which had the amplitude value of 64dB and assumed to correspond to a main crack initiation occurring at a mean load level about 87% of maximum load (see Table 4.6).

By using this approach, it may be possible to suggest a trend for indentation crack growth processes based on change in AE hit abs-energy (Figure 5.4) which is similar to the fatigue crack growth model proposed by Vashishth et al. (1997; 2003) (Figure 5.5). As can be seen in Figure 5.4, the initial low energy AE hits (marked A) may be associated with initial microcracking (phase I in Figure 5.5), followed by a rapid rise in abs-energy from a higher energy AE hit (marked B) possibly associated with a main crack formation (phase II in Figure 5.5). This cycle was observed as the second phase of lower energy signals were generated (marked C) followed by a higher energy signal (marked in D) to derive the main crack (phase III in Figure 5.5) up to the highest energy AE hit (marked E) which is associated with complete fracture event. Association of the highest energy signal with final fracture events was previously demonstrated by other researchers during AE testing on concrete (Landis and Ballion, 2002) and bone cement materials (Jeffers et al., 2005). It should be noted that all high energy AE hits might not be related to one main crack growth only as multiple major cracks may form suddenly during test.

This analysis approach for all specimens showed that, although there is potentially a similar crack growth model as shown above, some minor differences were observed from specimen to specimen which are due to the complex osteonal structure of bone

as recently described by other researchers (Akkus et al., 2001, O'Brien et al., 2003; 2005).

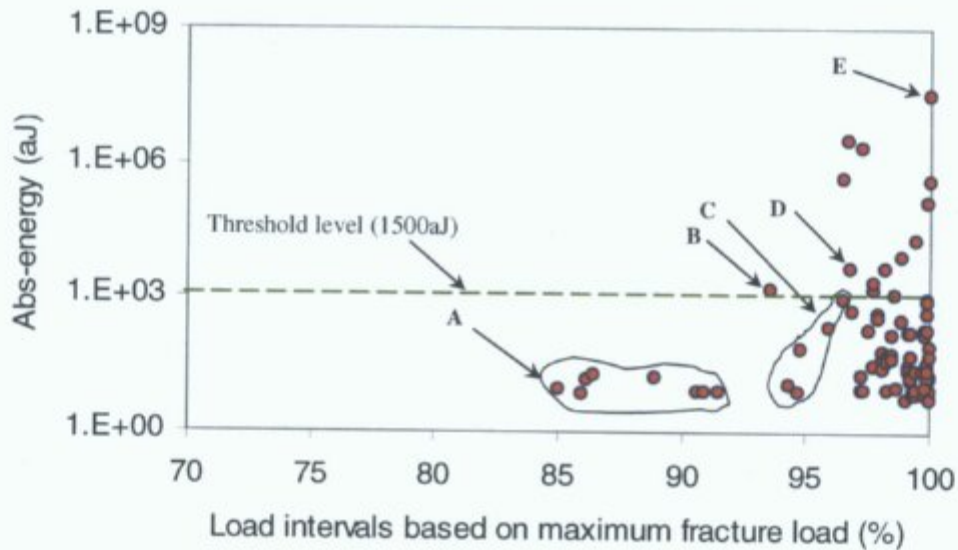


Figure 5.4: Crack growth process based on change in AE hit abs-energy during indentation cutting

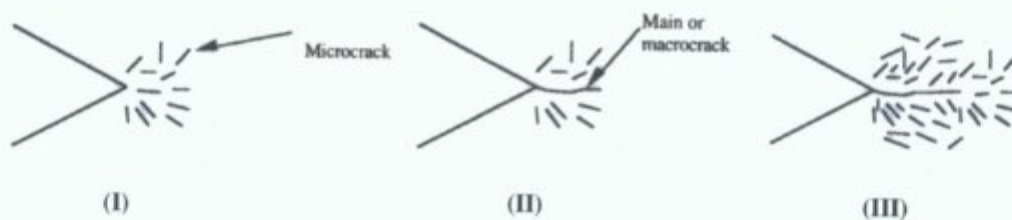


Figure 5.5: Fatigue crack growth processes (Vashishth et al., 1997)

From the analysis of abs-energy during loading, it is assumed that there are some possibilities during crack growth processes as follows:

1. The final AE hit energy associated with the final fracture event was found to vary from specimen to specimen (Figure 4.14). The greater abs-energy (duration dependant) may be generated by a slower final fracture event to overcome the barrier effects and find an easier crack growth path. It has been shown that in cortical bone, cracks deviate and travel around lamellae in an attempt to find the path of least resistance (O'Brien et al., 2003; 2005);

2. As previously observed in Figure 4.14, the considerable amount of abs-energy produced before the final fracture related signal in some specimens (G2-3 & G3-1) could correspond to earlier major fracture events prior to final separation of the specimen;
3. The alternating nature of abs-energy produced in some specimens (Figure 5.6) may stem from some kind of resistance against advance of the crack. Increase in energy of the signal to overcome the barriers during crack propagation as previously reported by From et al. (1995) during an indentation cracking process in ceramic composite materials. In the case of bone, this is likely to be associated with stop/start crack growth (as shown in the figure below in which; Phase A: the crack starts, Phase B: the crack stops, Phase C: the crack starts again up to final fracture). This may stem from the structural crack arresting mechanisms in bone (O'Brien et al., 2003; 2005) or microcracking toughening effect (Vashishth 97; 2003).

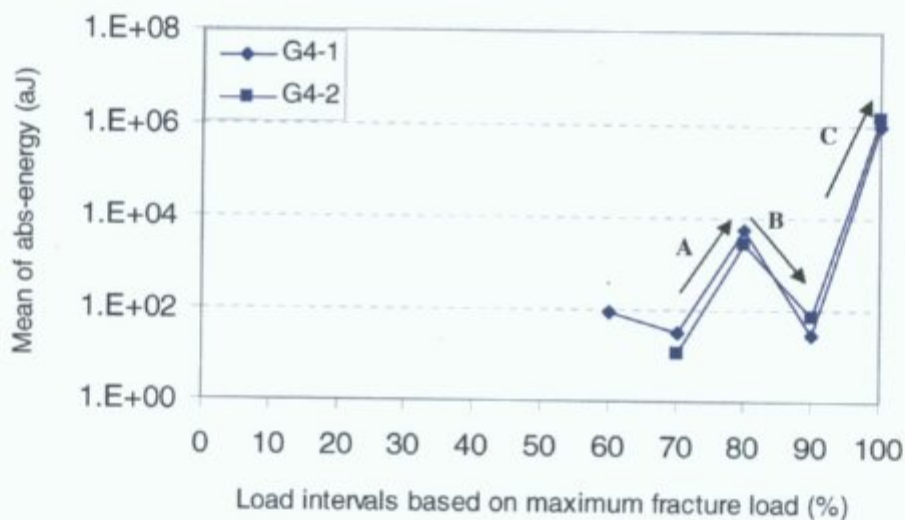


Figure 5.6: Stop/start crack growth process occurring in some specimens

5.2.4 Crack initiation and propagation during indentation process

As discussed in previous sections, it was concluded that crack initiation, propagation and final fracture can be describe based on change in AE hit rate and abs-energy. The crack growth model based on a combined AE and load analysis proposed in this study is shown in Figure 5.7 for a typical specimen tested.

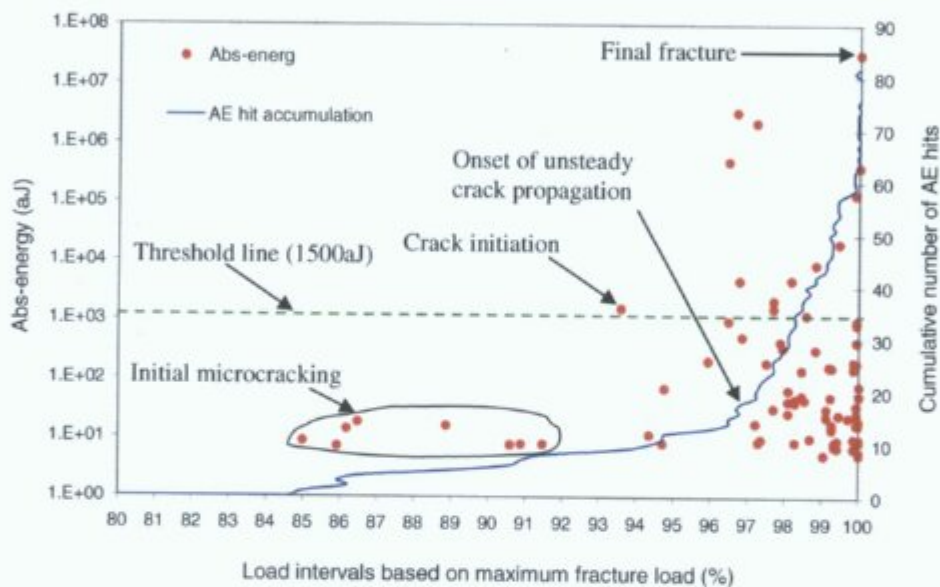


Figure 5.7: Crack initiation and propagation phases during indentation cutting based on the change in AE hit accumulation and abs-energy content

The crack growth phases for specimens tested are described as follows:

- 1) The first detected AE hit (41dB) may be indicative of an initial microcrack related event which occurred within the load range of 47-85% of maximum load (see Table 4.1);
- 2) The first high amplitude AE hit with amplitude value of over 64dB (with an approximate mean value of abs-energy of 1500aJ) may be associated with main crack initiation which occurred within the load range of 77-97% of maximum load (see Table 4.6);

- 3) The rapid increase in AE hit accumulation after registering the first high amplitude signal may indicate a transition phase between steady and unsteady crack propagation which occurred in the load range of 93-99% of maximum load (see Table 4.1). Due to the fact that the rapid rise in AE hit accumulation occurred just after observation of the first high energy signal in some specimens, it was difficult to define clearly between the transition phase from steady to unsteady crack propagation and it is proposed that the main crack propagates in an unsteady manner during indentation cutting as soon as it initiates;
- 4) The significant rise in abs-energy at 100% of peak load is indicative of the complete fracture event.

5.3 Discussion of results in experiment 2

In experiment 2, an exponential increase in the number of AE hits in specimens tested at 3 cutting steps of 50/90/100% of maximum fracture load was in accordance with other previous AE studies on bone that demonstrated damage-related AE activity follows a power law relationship (Netz et al., 1980; Wright et al., 1981; Jonsson et al., 1984; Fischer et al., 1986; Zioupos et al., 1994).

Observation of AE signals in all specimens subjected to indentation cutting up to 90% of maximum load may indicate that the initial damage occurred at primary load levels during this second loading stage. Due to the fact that no AE activity was observed in some specimen subjected to cutting load up to 50% of maximum load, it may be concluded that the onset of damage is mostly identified between 50 and 90% of maximum fracture load. The significant increase in the number of AE hits for specimens cut up to final fracture (at 100% maximum load) compared to specimens

cut up to 90%, may show an increase in the number of fracture events as a result of microcracking, main crack initiation and propagation.

The significant increase in abs-energy between 90% and 100% of maximum load may indicate that the main crack initiation and propagation, which were assumed to be caused by high energy signals, occurred within this load range. It should be noted that the majority of the signals were low amplitude (energy) associated with microcracking process. The results from experiment 2 also showed that the final signal at maximum fracture load had the mean duration value of 4583 μ s which is similar to that previously recorded during bone cement cracking process (approx. 4000 μ s) (Jeffers et al., 2005).

In summary, the indentation fracture was found to be similar to compressive fracture described by George and Vashishth (2005) which shows a 2 stage cracking process with crack initiation occurring at a high load (relative to fracture load), followed by a very fast crack propagation up to the final complete fracture event.

Chapter 6: Conclusions and Future Work

6.1 Conclusions

The data from this experimental work showed that the acoustic emission technique is a useful method for monitoring crack initiation and propagation during the indentation cutting processes. The experimental research completed and the results generated and recorded are in agreement with previous literature. A number of conclusions may be made from the results and analysis of the data in this research. Specific outcomes of this series of experiments are:

1. Onset of AE activity which is likely to be associated with initial damage is detected within the load range of 47-85% of maximum fracture load. This AE activity continues to accumulate in a nonlinear manner up to the fracture point between 90-100% of maximum fracture load;
2. An amplitude threshold value of 64dB (approx.1500aJ abs-energy content) may be used to separate AE signals associated with microcracking from crack growth related signals;
3. There is evidence that many of the AE signals generated are likely to be associated with damage such as microcracking; 80% of the total AE signals during indentation cutting have an amplitude below 64dB which has been shown by this research to correspond to the amplitude range for signals generated by microcracking, whereas the remaining 20% have higher amplitude and may be separated into a category associated with main crack growth;

4. Absolute energy (abs-energy) of the signal is an useful AE parameter to distinguish between microcrack and main crack events as well as identifying crack initiation, propagation and final complete fracture event;
5. A high energy signal which generally occurred during testing in the load range of 77-97% of maximum fracture load may indicate the main crack initiation;
6. The main crack may propagate in an unsteady manner just prior to maximum fracture load at load in the range of 93-99% of maximum fracture load;
7. The final fracture event at maximum load produced the highest energy signal during the indentation cutting process;
8. It is possible to separate out the complete fracture event at maximum load from other multiple cracks which did not grow up to the complete fracture based on abs-energy (or duration).

6.2 Recommendations for future work

The following recommendations have been put forward to support future research in this field:

1. A further study is recommended to identify friction related events from actual damage related signals by investigating the Kaiser effect in bone specimens subjected to cyclic indentation loading;
2. In this study, AE signals are clustered on the basis of amplitude, however, a further multiple clustering method is strongly recommended based on all AE parameters including amplitude, duration, rise time and number of counts;
3. This study is based on the hypothesis that “a high amplitude (energy) signal is an indication of main crack initiation” and relied on a statistically calculated

amplitude value of 64dB to detect main crack initiation, however, it is necessary to apply cyclic indentation cutting load on bone and carry out microscopy studies (which it is being carried out by other researchers within this group) to verify the amplitude value for crack initiation signals;

4. In order to further investigate multiple fracture events at different locations in the specimen, further AE testing would be required in conjunction with histological observation and use of multiple sensors for improved location of source of AE signals;
5. The effect of bone structure on speed of acoustic signals and AE signal attenuation needs to be investigated by use of 2 sensors in a standard method using signal generators and AE monitoring.

References

- Akkus, O., Jepsen, K. J., & Rimnac, C. M. 2000, Microstructural aspects of the fracture process in human cortical bone, *Journal of Materials Science*, vol. 35, pp. 6065-6074.
- Akkus, O. & Rimnac, C. M. 2001, Cortical bone tissue resists fatigue fracture by deceleration and arrest of microcrack growth, *Journal of Biomechanics*, vol. 34, pp. 757-764.
- Bakuckas, J. G., & Awerbuch, J. 1987, Crack-tip damage progression and acoustic emission in unidirectional silicon-carbide/titanium 6Al-4V composite, in *Advance Material Symposium*, Tokyo, Japan, pp. 33-42.
- Berkovits, A., & Fang, D. 1995, Study of fatigue crack characteristics by acoustic emission, *Engineering Fracture Mechanics*, vol. 51, pp. 401-416.
- Bianchett, R., Hamstad, M. A., & Mukherjee, A. K. 1976, Origin of burst-type acoustic emission in unflawed 7075-T6 Aluminum, *Journal of Testing and Evaluation*, vol. 4, pp. 313-318.
- Burr, D. B., & Stafford, T. 1990, Validity of the bulk-staining technique to separate artifactual from *in vivo* bone microdamage, *Clinical Orthopaedics and Related Research*, vol. 260, pp. 305-308.
- Burr, D. B., Martin, R. B., Schaffler, M. B., & Radin, E. L. 1985, Bone remodeling in response to *in vivo* fatigue microdamage, *Journal of Biomechanics*, vol. 18, pp. 189-200.
- Burr, D. B., Turner, C. H., Naick, P., Forwood, M. R., Ambrosius, W., Sayeed Hasan, M., & Pidaparti, R. 1998, Does microdamage accumulation affect the mechanical properties of bone?, *Journal of Biomechanics*, vol. 31, pp. 337-345.
- Bury, K., 1999, *Statistical Distribution in Engineering*, Cambridge University Press, United Kingdom.
- Carter, D. R., & Hayes, W. C. 1977, Compact bone fatigue damage: a microscopic examination, *Clinical Orthopaedics and Related Research*, vol. 127, pp. 265-274.
- Currey, J. D. 2002, *Bones: Structure and Mechanics*, Princeton University Press, Princeton, New Jersey.
- Currey, J. D., & Brear, K. 1992, Fractal analysis of compact bone and antler fracture surfaces', *Biomimetics*, vol. 1, pp. 103.
- Fang Q., Sidky, P. S., & Hocking, G. M. 2000, Cracking behaviours and stresses release in titanium matrix composites, *Materials Science and Engineering A*, vol. 288, pp. 142-147.

Fischer, R. A., Arms, S. W., Pope, M. H., & Sèligson, D. 1986, Analysis of the effect of using two different strain rates on the acoustic emission in bone, *Journal of Biomechanics*, vol. 19, pp. 119-121.

Fitz-Randolph, J., Phillips, D. C., & Beaumont, P. W. R. 1972, The fracture energy and acoustic emission of a born-epoxy composite, *Journal of Materials Science*, vol. 7, pp. 289-294.

From, P. S., Pyrz, R., Clausen, B., & Nielsen, E. O. 1995, Indentation and acoustic emission in filtration processed platelet reinforced ceramics, *Materials Science and Engineering A*, vol. 197, pp. 231-236.

Frost, H. M. 1960, Presence of microscopic cracks in vivo in bone, *Henry Ford Hospital Bulletin*, no.8, pp. 27-35.

George, W. T., & Vashishth, D. 2005, Damage mechanisms and failure modes of cortical bone under components of physiological loading, *Journal of Orthopaedic Research*, vol. 23, pp. 1047-1053.

Giraud, J.Y., Villemin, S., Darmana, R., Cahuzac, J. P., Autefage, A., & Morucci, J. P. 1991, Bone cutting, *Clinical Physics and Physiological Measurement: An Official Journal of The Hospital Physics Association*, vol. 12, pp. 1-19.

Hanagud, S., & Clinton, R. G. 1975, Acoustic Emission Techniques in the Development of a Diagnostic Tool for Osteoporosis, in *IEEE Ultrasonics Symposium*, pp. 41-45.

Hanagud, S., Clinton, R. G., & Lopez, J. P. 1973, Acoustic Emission in Bone Substance, in *ASME Winter Annual Meeting, Bio Mechanics Symposium*.

Hanagud, S., & Clinton, R. G. 1977, Soft Tissues and Acoustic Emission Based Diagnostic Tools, in *IEEE Ultrasonics Symposium*, pp. 242-245.

Hasegawa, K., Takahashi, H. E., Koga, Y., Kawashima, T., Hara, T., Tanabe, Y., & Tanaka, S. 1993, Mechanical properties of osteopenic vertebral bodies monitored by acoustic emission, *Bone*, vol. 14, pp. 737-743.

Hazenbergh, J. G., Taylor, D., & Lee, T. C. 2006, Mechanisms of short crack growth at constant stress in bone, *Biomaterials*, vol. 27, pp. 2114-2122.

Hill, R. 1953, On the mechanics of cutting metal strips with knife-edged tools, *Journal of The Mechanics and Physics of Solids*, vol. 1, pp. 265-270.

Jeffers, J. R. T., Browne, M., & Taylor, M. 2005, Damage accumulation, fatigue and creep behaviour of vacuum mixed bone cement, *Biomaterials*, vol. 26, pp. 5532-5541.

Jepsen, K. J., Davy, D. T., & Krzyppow, D. J. 1999, The role of the lamellar interface during torsional yielding of human cortical bone, *Journal of Biomechanics*, vol. 32, pp. 303-310.

Johnson, R. A., & Wichern, D. W. 1988, *Applied multivariate statistical analysis*, Prentice Hall, New Jersey.

Jonsson, U., & Eriksson, K. 1984, Microcracking in dog bone under load. A biomechanical study of bone visco-elasticity, *Acta Orthopaedica Scandinavica*, vol. 55, pp. 441-445.

Kadar, C., Chmelik, F., Rajkóvits, Z., & Lendvai, J. 2004, Acoustic emission measurements on metal foams, *Journal of Alloys and Compounds*, vol. 378, pp. 145-150.

Knet-s, I. V., Krauya, U. E., & Vilks, Yu. K. 1975, Acoustic emission in human bone tissue subjected to longitudinal extension, *Mekhanika Polimerov*, vol. 4, pp. 685-690.

Kohn, D. H., Ducheyne, P., & Awerbuch, J. 1992a, Acoustic Emission During Fatigue of Porous Coated Ti-6Al-4V Implant Alloy, *Journal of Biomedical Materials Research*, vol. 26, pp. 19-38.

Kohn, D. H., Ducheyne, P., & Awerbuch, J. 1992b, Acoustic emission during fatigue of Ti-6Al-4V - incipient fatigue crack detection limits and generalized data -analysis methodology, *Journal of Materials Science*, vol. 27, pp. 3133-3142.

Landis, E. N., & Ballion, I. 2002, Experiments to relate acoustic emission energy to fracture energy of concrete, *Journal of Engineering Mechanics*, vol. 128, pp. 698-702.

Lawn, B. W. R. 1975, Indentation fracture: principles and applications, *Journal of Materials Science*, vol. 10, pp. 1049-1081.

Lee, T. C., O'Brien, F. J., & Taylor, D. 2000, The nature of fatigue damage in bone, *International Journal of Fatigue*, vol. 22, pp. 847-853.

Martin, R. B., Burr, D. B., & Sharkey, N. A. 1999, *Skeletal tissue mechanics*, Springer-Verlag, New York.

Mashino, S., Mashimo, Y., Horiya, T., Shiwa, M., & Kishi, T. 1996, Analysis of microfracture mechanism of titanium alloy by acoustic emission technique, *Materials Science and Engineering A*, vol. 213, pp. 66-70.

Merchant, M. E. 1944, Basic mechanics of the metal-cutting process, *Journal of Applied Mechanics*, vol. 11, pp. 168-175.

Miller, R. K. & Hill, E. K. 2005, *Nondestructive testing handbook: Acoustic emission testing (vol. 6)*, 3 edn, American society for nondestructive testing (ASNT).

Nalla, R. K., Kruzic, J. J., & Ritchie, R. O. 2004, On the origin of the toughness of mineralized tissue: microcracking or crack bridging?, *Bone*, vol. 34, pp. 790-798.

Nalla, R. K., Stolken, J. S., Kinney, J. H., & Ritchie, R. O. 2005, Fracture in human cortical bone: local fracture criteria and toughening mechanisms, *Journal of Biomechanics*, vol. 38, pp. 1517-1525.

Netz, P., Eriksson, K., & Stromberg, L. 1980, Material reaction of diaphyseal bone under torsion. An experimental study on dogs, *Acta Orthopaedica Scandinavica*, vol. 51, pp. 223-229.

- Nicholls, P. J., & Berg, E. 1981, Acoustic emission properties of callus, *Medical and Biological Engineering and Computing*, vol. 19, pp. 416-418.
- Norman, T. L., & Wang, Z. 1997, Microdamage of human cortical bone: Incidence and morphology in long bones, *Bone*, vol. 20, pp. 375-379.
- O'Brien, F. J., Hardiman, D. A., Hazenberg, J., Mercy, M. V., Mohsin, S., Taylor, D., & Lee, T. C. 2005, The behaviour of microcracks in compact bone, *European Journal of Morphology*, vol. 42, pp. 71-79.
- O'Brien, F. J., Taylor, D., Dickson, G. R., & Lee, T. C. 2000, Visualisation of three dimensional microcracks in compact bone, *Journal of Anatomy*, vol. 197, pp. 413-420.
- O'Brien, F. J., Taylor, D., & Lee, T. C. 2002, An improved labelling technique for monitoring microcrack growth in compact bone, *Journal of Biomechanics*, vol. 35, pp. 523-526.
- O'Brien, F. J., Taylor, D., & Lee, T. C. 2003, Microcrack accumulation at different intervals during fatigue testing of compact bone, *Journal of Biomechanics*, vol. 36, pp. 973-980.
- Pook, L. P. 2000, *linear elastic fracture mechanics for engineers: Theory and application*, University College London, United Kingdom.
- Rajachar, M. R., Christopher, E. C., Weissman, N. A., & Kohn, D. H. 1999, Use of acoustic emission to characterize focal and diffuse microdamage in bone, in *Acoustic emission: Standard and technology update*, ASTM STP 1353..
- Ray, A. K., Bhattacharya, D. k., & Das, G. 1996, Acoustic emission studies during indentation on ceramic and ceramic composite, in *14th world conference on Non destructive testing*, New Dehli, India, pp. 2455-2458.
- Reilly, C. G., & Currey, J. D. 1999, The development of microcracking and failure in bone depends on the loading mode to which it is adapted, *Journal of Experimental Biology*, vol. 202, 543-552.
- Reilly, D. T., & Burstein, A. H. 1975, The elastic and ultimate properties of compact bone tissue, *Journal of Biomechanics*, vol. 8, pp. 393-396.
- Reilly, D. T., Burstein, A. H., & Ohio, C. 1974, Review article. The mechanical properties of cortical bone, *Journal of Bone and Joint Surgery*, vol. 56, pp. 1001-1022.
- Reilly, G. A., & Taylor, D. 2005a, Cutting bone: fluorescent labelling of the damage zone in bovine cortical bone, in *the 11th annual conference of the bioengineering of the Royal Academy of Medicine*, Ireland.
- Reilly G. A., & Taylor D. 2005b, An analysis of the fracture process and microdamage occurring during cutting of cortical bone, in *the 1st International Conference on Mechanics of Biomaterials & Tissues*, Wikoloa, Hawaii, USA.

Reilly, G. A. McCormack. B. A. O., & Taylor. D. 2004, Cutting sharpness measurement: a critical review, *Journal of Materials Processing Technology*, vol. 153-154, pp. 261-267.

Reilly, G. C., 2000, Observations of microdamage around osteocyte lacunae in bone, *Journal of Biomechanics*, vol. 33, pp. 1131-1134.

Rho, J. Y., Kuhn-Spearing, L., & Zioupos, P. 1998, Mechanical properties and the hierarchical structure of bone, *Medical Engineering & Physics*, vol. 20, pp. 92-102.

Ritchie, R. O. Kinney. J. H. Kruzic. J. J., & Nalla. R. K. 2005, A fracture mechanics and mechanistic approach to the failure of cortical bone, *Fatigue Fracture Engineering Materials Structure*, vol. 28, pp. 345-371.

Roberts, T. M., & Talebzadeh, M. 2003, Acoustic emission monitoring of fatigue crack propagation, *Journal of Constructional Steel Research*, vol. 59, pp. 695-712.

Roques, A., Browne, M., Thompson, J., Rowland, C., & Taylor, A. 2004, Investigation of fatigue crack growth in acrylic bone cement using the acoustic emission technique, *Biomaterials*, vol. 25, pp. 769-778.

Schaffler, M. B., Choi, K., & Milgrom, C. 1995, Aging and matrix microdamage accumulation in human compact bone, *Bone*, vol. 17, pp. 521-525.

Schaffler, M. B., Pitchford, W. C., Choi, K., & Riddle, J. M. 1994, Examination of compact bone microdamage using back-scattered electron microscopy, *Bone*, vol. 15, pp. 483-488.

Schaffler, M. B., Radin, E. L., & Burr, D. B. 1990, Long-term fatigue behaviour of compact bone at low strain magnitude and rate, *Bone*, vol. 11, pp. 321-326.

Schaffler, M. B., Radin, E. L., & Burr, D. B. 1989, Mechanical and morphological effects of strain rate on fatigue of compact bone, *Bone*, vol. 10, pp. 207-214.

Thomas, R., Yoon. H. S., & Katz J. L. 1977, Acoustic Emission from Fresh Bovine Femora, in IEEE Ultrasonics Symposium, New York, pp.237-241.

Tortora, G. J., & Derrickson, B. H. 2005, *Principles of Anatomy and Physiology*, John Weilly & Sons Inc., New Jersey.

Vashishth, D., Behiri, J. C., & Bonfield, W. 1997, Crack growth resistance in cortical bone: Concept of microcrack toughening, *Journal of Biomechanics*, vol. 30, pp. 763-769.

Vashishth, D., Tanner, K. E., & Bonfield, W. 2003, Experimental validation of a microcracking-based toughening mechanism for cortical bone, *Journal of Biomechanics*, vol. 36, pp. 121-124.

Vashishth, D., Tanner, K. E., & Bonfield, W. 2000, Contribution, development and morphology of microcracking in cortical bone during crack propagation, *Journal of Biomechanics*, vol. 33, pp. 1169-1174.

Wright, T. M., Vosburgh, F., & Burstein, A. H. 1981, Permanent deformation of compact bone monitored by acoustic emission, *Journal of Biomechanics*, vol. 14, pp. 405-409.

Xiaodu W. & Agrawal, C. M. 1996, Fracture toughness of bone using a compact sandwich specimen: Effects of sampling sites and crack orientations, *Journal of Biomedical Materials Research Part B: Applied Biomaterials*, vol. 33, pp. 13-21.

Yoon, H. S., Caraco, B., Kaur, R., & Katz, J. L. 1980, Clinical application of acoustic emission techniques to bone abnormalities, in *IEEE Ultrasonics Symposium*, New York, pp. 1067-1072.

Zioupos, P. 2001, Accumulation of in-vivo fatigue microdamage and its relation to biomechanical properties in ageing human cortical bone, *Journal of Microscopy*, vol. 201, pp. 270-278.

Zioupos, P., Currey, J. D., & Sedman, A. J. 1994, An examination of the micromechanics of failure of bone and antler by acoustic emission tests and Laser Scanning Confocal Microscopy, *Medical Engineering and Physics*, vol. 16, pp. 203-212.

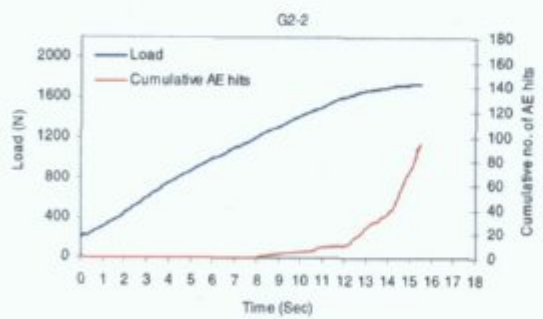
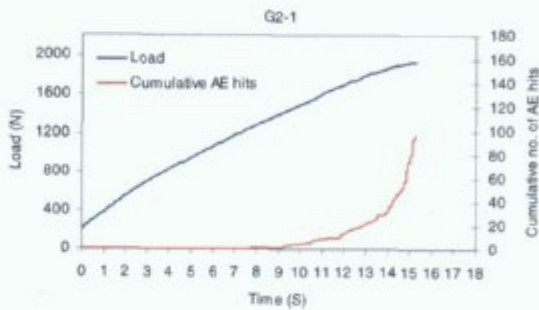
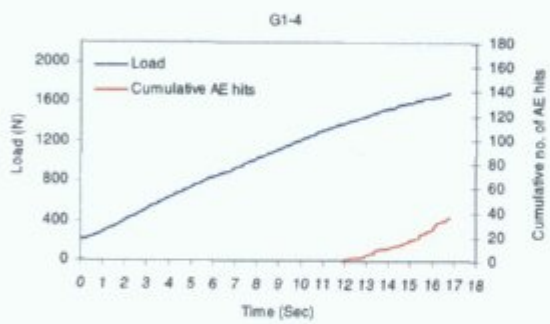
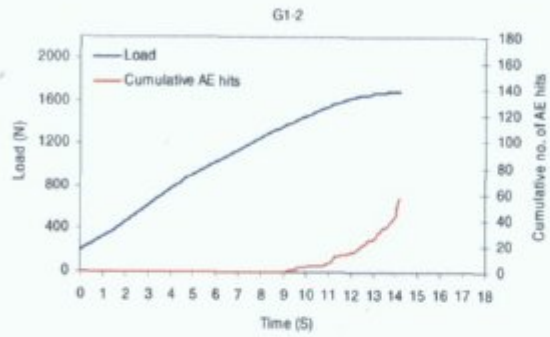
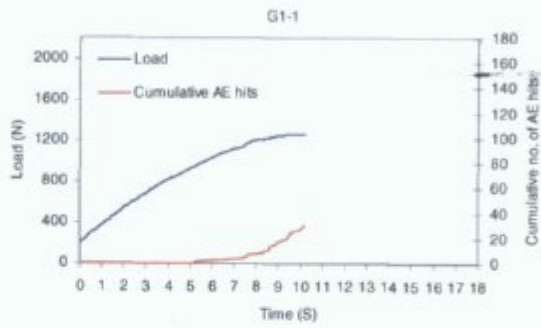
Zioupos, P., & Currey, J. D. 1994, The extent of microcracking and the morphology of microcracks in damaged bone, *Journal of Materials Science*, vol. 29, pp. 978-986.

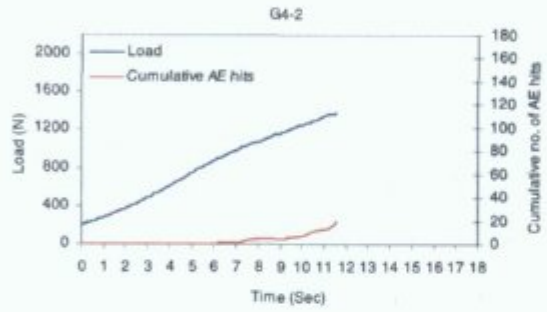
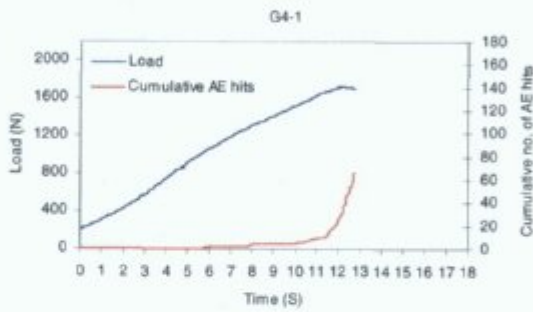
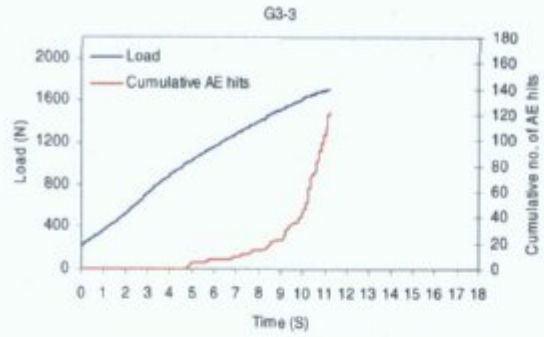
Appendix A

Results of experiment 1

Appendix A1

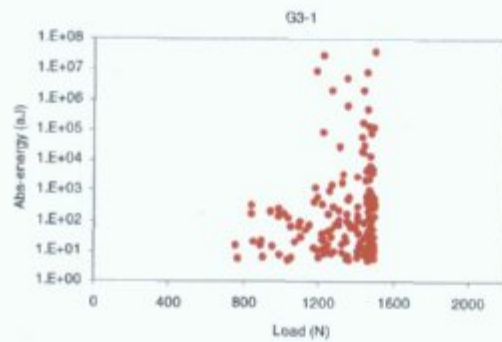
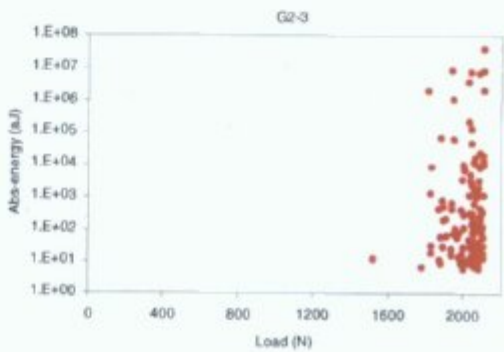
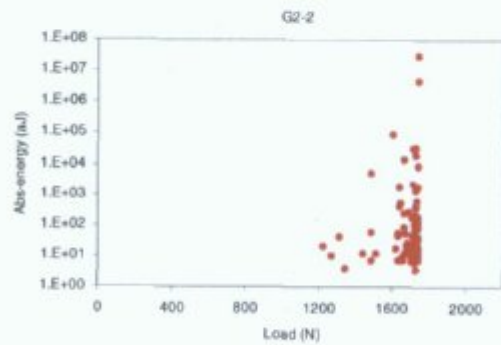
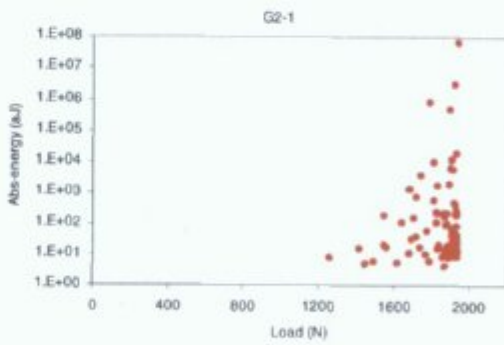
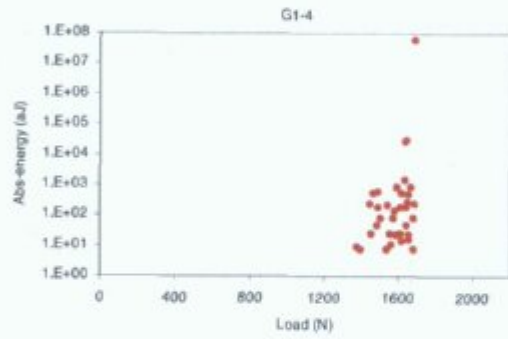
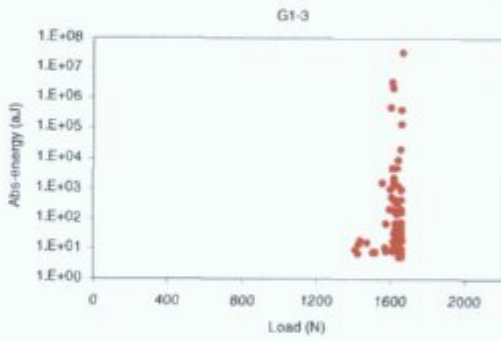
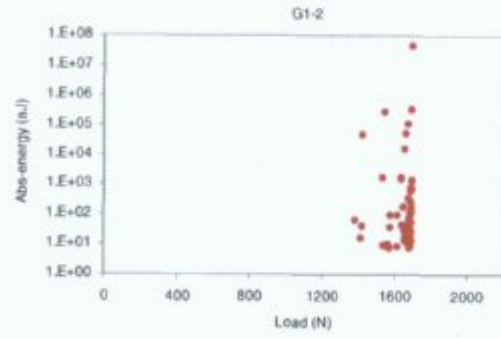
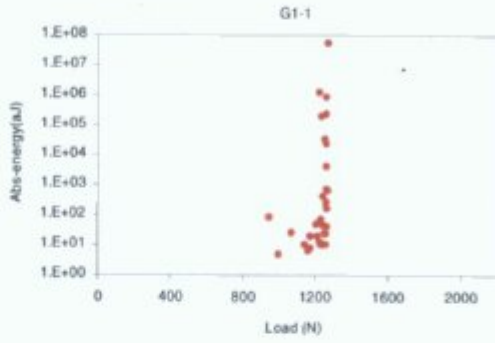
Experiment 1 - Graphs of load & cumulative number of AE hits versus time

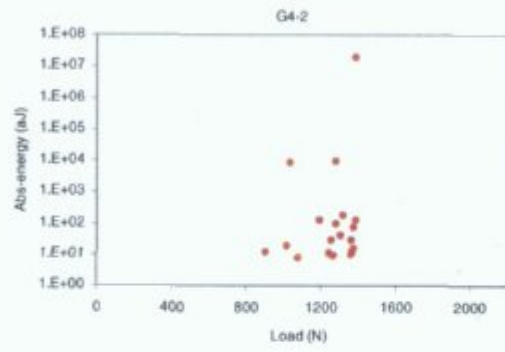
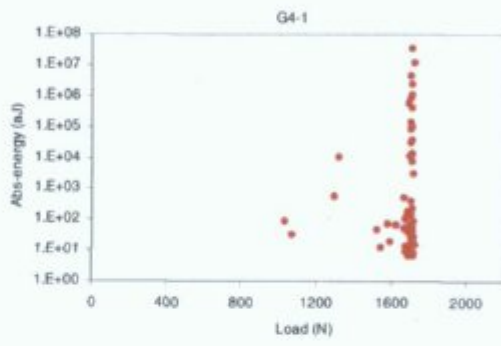
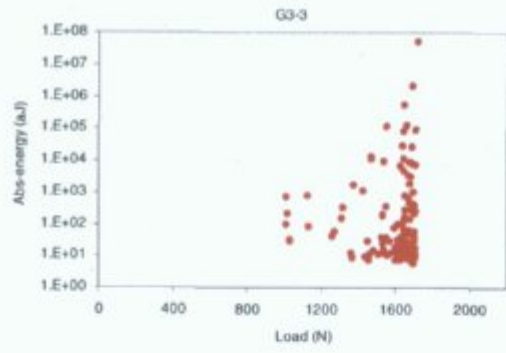
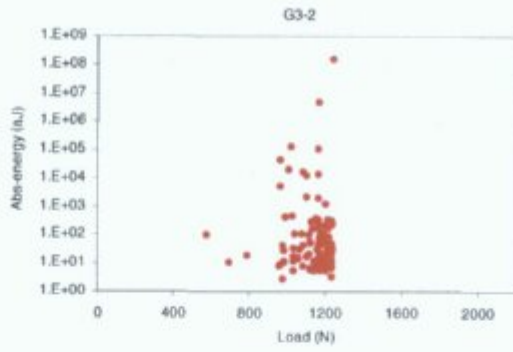




Appendix A2

Experiment 1 - Graphs of abs-energy versus load





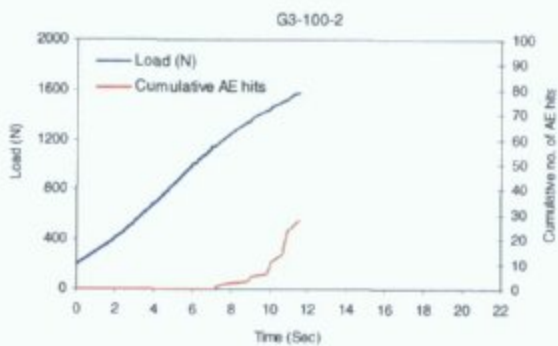
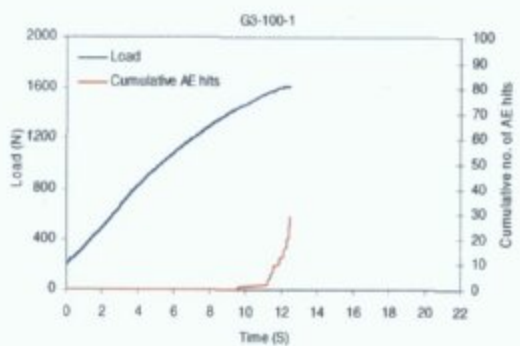
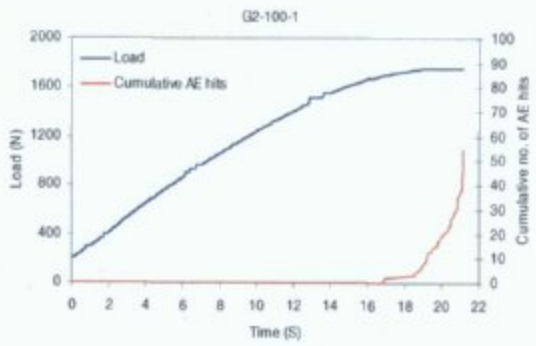
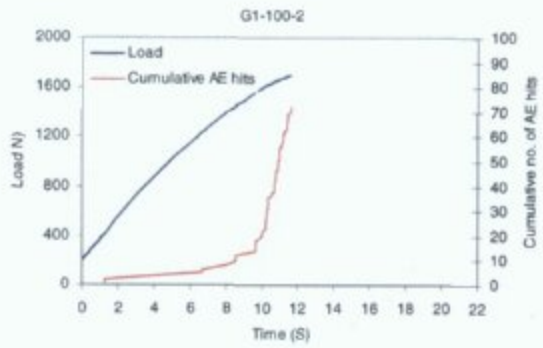
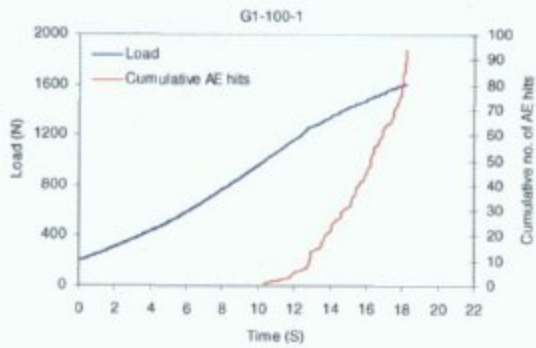
Appendix B

Results of experiment 2

Appendix B1

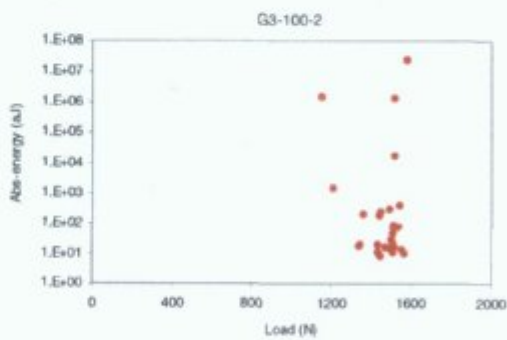
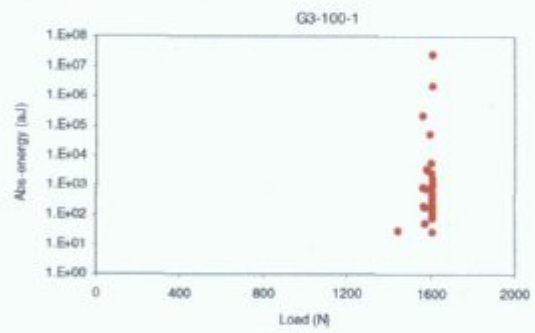
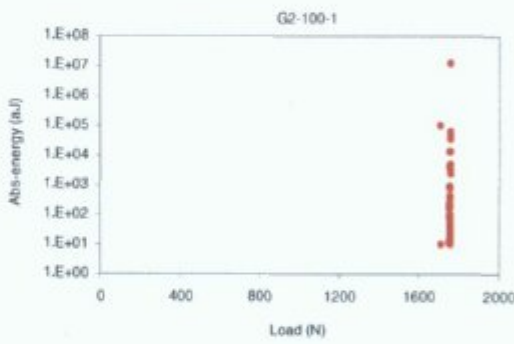
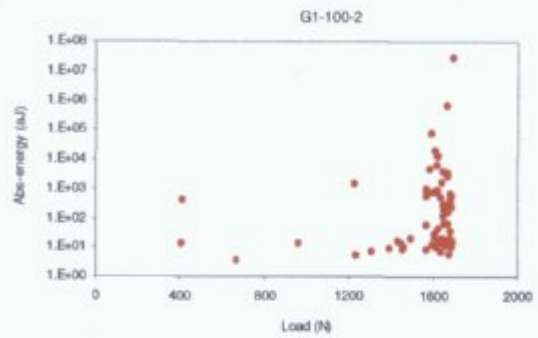
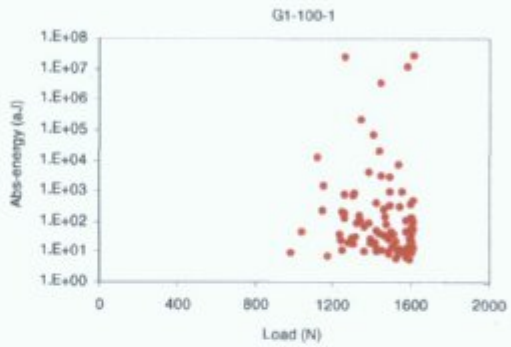
Experiment 2 - Graphs of load & cumulative number of AE hits versus time

(5 fractured specimens)



Appendix B2

Experiment 2 - Graphs of abs-energy versus load (5 fractured specimens)



Appendix C

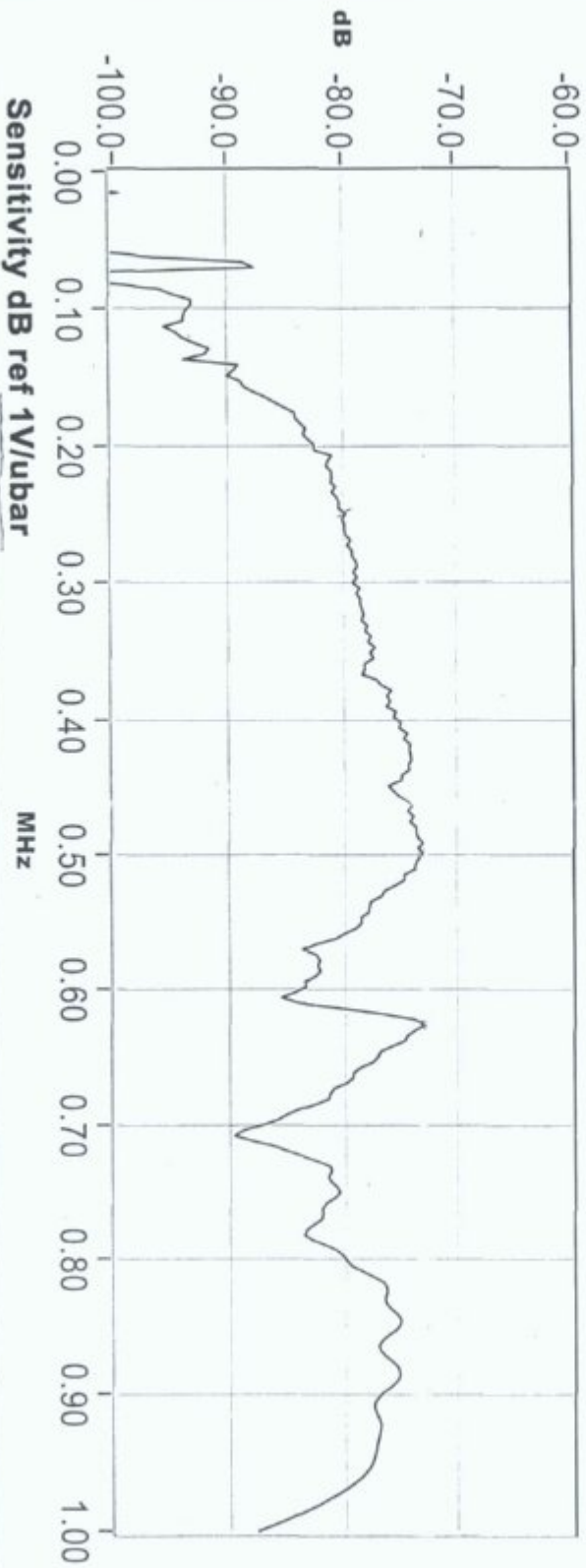
Technical sheet



A MISTRAS Holdings Company

AE SENSOR CALIBRATION CERTIFICATE

Sensor Name: PICO Test Date: 5/28/04 Max. Value (dB): -72.96
Sensor S/N: 4081 Tested By: B.W. Peak Freq.(kHz): 625.00
Comment:



PAC Certifies that this sensor meets all performance, environmental and physical standards established in applicable PAC specifications. Calibration methodology based on ASTM standard E976- "Guide for Determining the Reproducibility of Acoustic Emission Sensor Response."



AE Sensor Calibration Project